FINAL REPORT FOR ALPHA FOUNDATION TARGETED RESEARCH GRANTS (AFCTG22r2-159)

Title: *Assessment of Pillar Stability in Underground Room & Pillar Mines from Autonomous Robotic Inspections*

Grant Number: AFCTG22r2-159

Submitting Organization:
West Virginia University
Research Corporation
886 Chestnut Ridge Road, PO Box 6845
Morgantown, WV 26506-6845
DUNS #: 191510239 EIN#: 550665758

Participating Organization:
Virginia Tech
300 Turner Street NW - Suite 4200
Blacksburg, VA 24061
DUNS #: 003137015 EIN#: 546001805

Principal Investigator: Deniz Tuncay, Ph.D., Assistant Professor
Department of Mining Engineering,
West Virginia University
Phone: 304-413-6465,
Email: deniz.tuncay@mail.wvu.edu

Co-Principal Investigators: Jason N. Gross, Ph.D.
Email: jason.Gross@mail.wvu.edu

Yu Gu, Ph.D.
Email: Yu.Gu@mail.wvu.edu

Guilherme A. S. Pereira, Ph.D.
Email: guilherme.pereira@mail.wvu.edu

Richard E. Bishop, Ph.D.
Email: ribishop@vt.edu

Period of Performance: 12/01/2022 to 11/30/2024

Disclaimer: This study was sponsored by the Alpha Foundation for the Improvement of Mine Safety and Health, Inc. (ALPHA FOUNDATION). The views, opinions and recommendations expressed herein are solely those of the authors and do not imply any endorsement by the ALPHA FOUNDATION, its Directors, and staff.

Table of Contents

1. Executive Summary:

In 2019 more than 2,000 miners worked in underground stone mining (NIOSH, 2021), and since 2006, approximately 40% of fatalities in this mining sector have been linked to falls of ground from roofs and pillars (MSHA, 2025). The modern pillar and roof span design guidelines developed by National Institute for Occupational Safety and Health (NIOSH) were published in 2011 and have improved the design of stable layouts for modern limestone mines. However, since then, five massive pillar collapses have occurred in older workings of active limestone mines, and four out of five occurred after 2020. On January 7, 2022, a massive roof fall claimed the life of a dozer operator in an underground mine operating in the Loyalhanna formation, and reports of extensive regionalized roof falls in other mines demonstrated the potentially severe risk to the safety of miners in underground stone mines.

Mine Safety and Health Administration (MSHA) has indicated that there is not any design method available to predict when, or even whether, a particular pillar or group of pillars would collapse, but it is possible to recognize hazards that might increase the likelihood of these massive collapses (MSHA, 2021). MSHA listed the following hazards that might cause pillar collapses: (i) irregular undersized pillars due to surveying or blasting errors, and (ii) ignoring or not realizing geological features (joints, weak bedding planes etc.) on the pillars that might reduce pillar stability or induce rib falls (MSHA, 2021). Unmanned Aerial Vehicles (UAV) and Unmanned Ground Vehicles (UGV) can be used to autonomously and safely scan old workings and capture high-resolution 3D maps for assessing pillar and roof damage and stability.

In 2019, the Alpha Foundation funded a project with West Virginia University (WVU) entitled "Autonomous Robotic Early Warning System for Underground Stone Mining Safety". In this project, WVU team developed a proof-of-concept of an autonomous robotics system for stone mine pillar inspection using LIDAR-based time-lapse 3D imaging from a UAV and a UGV system. Virginia Tech (VT) team also developed and applied drone technology for mapping underground mines and has demonstrated the capability of drones to reconstruct digital 3D models of mine pillars that can be used for geotechnical assessment and hazard identification. This collaborative project aimed to collect the necessary data from active stone mines by means of the existing autonomous UAV/UGV technologies and the expertise of VT and WVU teams, while evaluating and improving the field performance of the WVU autonomous systems and integrating the WVU autonomous flight control software and operational sensory subsystems to commercial drones currently used by VT. The ultimate goal of this project was to develop guidelines for stone mine operators to evaluate pillar stability of old workings and roof fall hazards from a UAV and/or UGV captured high-resolution 3D point clouds and geomechanical data. The research conducted in this project included: (i) Develop a database of mine layout, rock mass characteristics, and high-resolution 3D maps of stone mine pillars and roofs in old workings while evaluating and improving the application of conventional UAVs of VT and autonomous systems of WVU. (ii) Develop guidelines for recognizing hazards that might increase the possibility of massive pillar and roof collapses through the analysis of the database.

Accomplishments:

This project successfully demonstrated the use of autonomous robotic platforms for collecting high-resolution spatial data in underground stone mines and evaluating pillar

stability using advanced geomechanical analysis. Field deployments enabled the acquisition of detailed three-dimensional maps of underground workings, including pillars, entries, and roof conditions, which were subsequently processed to extract geometric and structural parameters relevant to stability assessment. The project also integrated robotic mapping technologies with geomechanical analysis techniques to evaluate pillar dimensions, loading conditions, and potential indicators of instability. These efforts produced a dataset and analytical workflow capable of supporting more objective and repeatable pillar stability evaluations compared to traditional visual inspections.

In addition, the research team identified the capabilities and current limitations of autonomous inspection technologies in underground mining environments. Improvements to mapping workflows, data processing methods, and geotechnical interpretation procedures were developed during the project. The collaboration between engineering, robotics, and mining researchers also resulted in a framework for future integration of autonomous data collection with mine design and ground control practices. The project generated valuable case studies and practical insights that can guide further development of robotic inspection tools for underground mine safety applications.

The project also contributed to workforce development in mining engineering and robotics. Students participated in field data collection, robotic system operation, and data analysis. Through this work, students gained hands-on experience in underground mine environments, geomechanical assessment, and advanced sensing technologies. Findings from this project have also been disseminated through conference presentations and journal manuscripts which help ensure that the developed methodologies reach both academic researchers and industry practitioners.

Expected impact on mining health and safety:

The outcomes of this research have the potential to significantly improve health and safety practices in underground stone mines by enabling more comprehensive, frequent, and safer assessments of pillar stability and ground conditions, especially in inactive areas. Autonomous robotic inspection systems can access areas that may be difficult or hazardous for personnel to enter, allowing for safer data collection in active or abandoned sections of mines. The high-resolution spatial data generated by these systems can help identify changes in pillar geometry, roof conditions, and other structural features that may indicate increasing ground control risk.

By providing quantitative and repeatable measurements of underground conditions, the methodologies developed in this project can support better informed ground control decisions and earlier detection of potentially unstable areas. This capability may ultimately reduce the risk and severity of pillar failures, roof falls, and other ground control hazards that threaten miner safety. Additionally, the integration of robotic mapping with geomechanical analysis creates opportunities for developing field informed numerical models that could further enhance proactive safety management in underground coal mines.

2. Problem Statement and Objective:

2.1 The Problem Statement and Focus Area

In stone mines, older mined sections stay open for the life of the mine, which may be many years and subject the pillars to time-dependent degradation. Since 2015, five massive pillar collapses have occurred in older workings of active limestone mines, and four out of five occurred after 2020. As stated by MSHA (MSHA, 2021), it might not be possible to predict a single or massive pillar collapse, but it is possible to recognize hazards that might increase the possibility of these events. In addition, hazards causing fall of ground accidents generally develop with time and it is possible to respond to detected potentially elevating hazardous conditions and prevent accidents. Therefore, proper inspection to identify hazards and deteriorating ground conditions, and rapid response to these hazardous conditions would protect miners from possible fall of ground accidents. This project aimed to develop guidelines for stone mine operators to evaluate pillar stability of old workings and roof fall hazards from robotic UAV and/or UGV captured high-resolution 3D point clouds and geomechanical data. While the problem of pillar and roof stability is associated with all underground operations, this project focuses on the underground stone mining industry and addresses the topical area "*Health and Safety Interventions"* with a specific emphasis on *"prevention of unstable ground conditions that result in collapses and roof/rib falls"*. Alpha Foundation Priority Areas 1) Ground Control - Prevention of unstable ground conditions that result in collapses; roof and rib falls; and injuries due to insufficient support coverage, and 2) Monitoring Systems and Integrated Control Technologies - Recognition of and intervention to prevent the escalation of conditions that lead to health and safety risks before they reach hazardous levels.

2.2 Background

The US Mine Safety and Health Administration (MSHA) classifies metal and nonmetal (M/NM) mining into four broad categories: metal, nonmetal, stone, and sand-and-gravel (MSHA, 2022a). MSHA Handbook Number PH20 V 2, Roof Control Plan and Ground Support Review Procedures, states that inspection personnel may use the guidelines and procedures in the PH20 V 2 handbook to evaluate the suitability of ground support materials and rock burst control plan, but unless a mine is burst-prone, there are no federal regulations stating that M/NM mines have to submit a ground support plan (MSHA, 2020). Pillar and roof span dimensions in the M/NM mines are largely based on experience, developed through trial and error, and there are no generally applicable guidelines for designing pillar layouts in M/NM mines apart from the underground stone mining industry.

The current state of pillar design in the US stone mines

In the US, the S-Pillar program was developed to assist in the design of stable pillars for room-and-pillar workings in underground stone mines (Esterhuizen et al, 2011). Esterhuizen et al. collected operational and pillar performance information from 34 different stone mines in the Eastern and Midwestern US. Then, they classified a total of 18 cases of individual pillars as failed, assessed each of the failed pillars visually, and categorized the failure mode of hard rock pillars as crushing or structure-controlled failures. Later, by completing a comprehensive numerical analysis to understand pillar behavior within the consideration of brittle rock spalling, large and angular

discontinuities, weak bedding bands, floor benching, and length of pillar, they established the empirical pillar strength equation governing stone mines in the US and the Spillar program.

Since the development of S-Pillar, there have been three major research projects to improve the safety of underground stone mining operations. NIOSH intramural research project concentrated on building a framework for expanding pillar design criteria used in S-Pillar software to multiple-seam, deep, and dipping mining environments (NIOSH, 2022). In this project, the NIOSH team used light detection and ranging (LIDAR) and photogrammetry methods to map case study mines and geological structures, characterize the rock mass, monitor rock mass deformation, and develop numerical models that simulate pillar responses and failure mechanisms. Virginia Polytechnic Institute and State University (VT) research, funded by NIOSH, focused on the application of LIDAR and photogrammetry for mapping discontinuities in case study mines and generating discrete fracture networks for stochastic discrete element simulation of stone mine pillars (Bishop, 2022). The major contribution of the VT research has been the demonstration of the successful applications of the UAVs to mapping and inspection of underground workings both with manual piloting and autonomously (Bishop, 2022). West Virginia University (WVU) research, funded by Alpha Foundation, consists of two parts: (i) development of an autonomous robotic system that is comprised of an UAV tethered to an Unmanned Ground Vehicle (UGV) for mapping underground stone mines, and (ii) development of a practical design approach that follows the S-Pillar empirical design method, uses LaModel and Stability Mapping software, and allows stone mine operators to integrate large geological structures, irregular pillar layouts, and variable topography into the global and local pillar stability analysis (Suner, 2021; Suner and Tulu, 2022; Escobar, 2021; Bendezu de la Cruz, 2021).

Escobar (2021) extended the application of the S-Pillar stone pillar strength equation to Boundary Element Method software (BEM), LaModel, by the derivation of a gradient stress equation for stone pillars from the empirical pillar strength equation proposed by Esterhuizen et al. (2011). This gradient stress equation provides the stress distribution within the pillar, and it is used to derive concentric rings of material to simulate a stone mine pillar yielding in the BEM. Figure 1a and Figure 1b show the overburden stress distribution and stress safety factor calculations for the case study mine in Loyalhanna formation using Escobar's stress gradient equations and LaModel software. Different yield zone elements were used to simulate the development and benched pillars in this study. It is observed that the benched pillars and "edge" pillars surrounding the fully benched pillars present a lower Factor of Safety (FOS) than the development pillars (Figure 1b). Moreover, the total vertical stress on the seam is incremented in pillars with higher overburden stress. Therefore, in the deepest areas of the mine, the factor of safety is smaller, and the vertical stress is higher, disregarding if the pillars are fully benched or development.

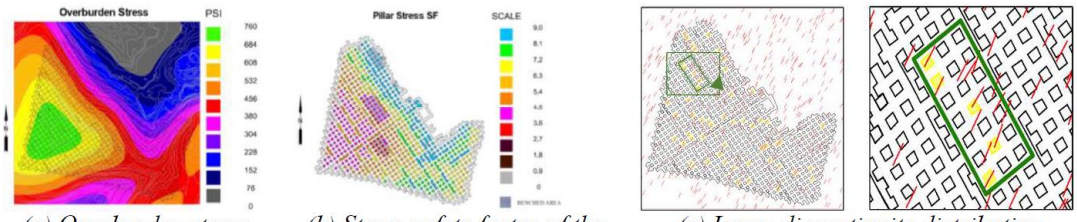

(a) Overburden stress distribution. *(b) Stress safety factor of the stone mine pillars.* *(c) Large discontinuity distribution relative to pillar layout.*

Figure 1 Case study application of WVU design approach (after, Escobar, 2021; Ates, 2022)

Ates (2022) developed a software tool that incorporates the large discontinuity impacts into the method developed by Escobar (2021) using: S-Pillar, Large Discontinuity Factor (LDF), and AutoCAD ObjectARX add-in Integrated Stability Mapping System (ISMS). Figure 1c shows the application of ISMS for finding the intersection of the pillars and large angular discontinuities on the case study mine layout. Red lines in this figure are the representation of the large discontinuity distribution, following the negative exponential distribution. Pillars that are intersected by the large discontinuities are highlighted with yellow. Figure 2a shows the safety factors of the pillars (in the green box shown in Figure 1c) without incorporating the influence of the large discontinuities on pillar strength. Figure 2b shows the safety factor distribution when the influence of large discontinuities is included in the analysis, and the safety factor of pillars that are intersected by large angular discontinuities is reduced by approximately 40% in this case study mine.

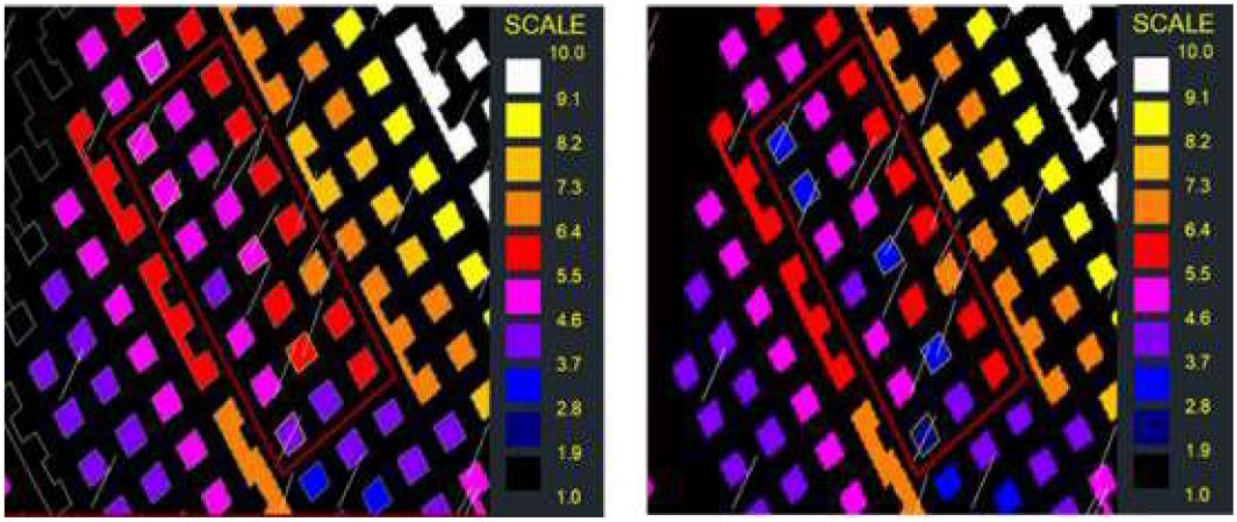

Figure 2 Safety factors of pillars before & after implementing the Large Discontinuity Factor.

The current state of roof span and support design in the US stone mines

Esterhuizen et al. (2011) stated that in underground stone mines, rooms are on average 44-ft wide, and the desired roof span dimensions are generally predetermined by the operational requirements, the size of the mining equipment, etc. The roof design in stone mines is generally focused on optimizing the stability of the roof under the usual rock mass conditions, and an unsupported roof is common in underground stone mines due to the inherently strong rock mass. Operators generally support the roof based on their experience in the mine if they encounter a geological condition or geological structure. Esterhuizen et al. (2011) stated that large roof falls were observed at 19 mine operations visited during the development of the roof span design guidelines. They reported that high horizontal stress contributed to 36%, failure of the weak band / parting plane within the roof beam contributed to 28%, large discontinuities contributed to 21% and failure of weak immediate roof strata contributed to 15% of all roof falls. NIOSH roof span design guidelines recommend stone mine operators should conduct detailed geotechnical characterization of the mine since the discontinuities play a major role in roof stability and should monitor changes in rock mass conditions. Therefore, successful roof support design depends on accurate identification of the geological structures and recognition of the adverse changes in rock mass conditions in the stone mines, and failure to recognize these hazards caused many massive roof fall accidents, the most

recent fatal accident happened on January 2022 in the mine operating in Loyalhanna formation (Figure 3). Adaptation of a sensory subsystem to an UAV that allows mine operators to inspect stone mine roofs through high-resolution pictures or point clouds would help the identification of the roof fall hazards.

Figure 3 Roof fall fatality in PA (MSHA, 2022b)

The current research on drone/robotic applications in mining

UAVs have become an integral part of the surface mining operations, where they allow operators to model the terrain quickly and effortlessly with GPS localization and advanced mission planning software (Bishop, 2022). In a GPS-denied environment, application of the UAV has been more challenging, although significant advancements in drone autonomy in GPS-denied environments has been made in recent years. There are three research projects, before WVU research, funded by Alpha Foundation for developing UAV systems for the US underground mining industry; AFC518-23 for developing permissible Aerial Vehicle. Platform (AVP) for underground coal mine applications, AFC518-67 for developing proof-of-concept and working prototype for UAV-based digital photogrammetry system for geological mapping, and AFC518-48 for autonomous navigation using a ground robot/UAV couple.

VT research, funded by NIOSH, demonstrated new techniques for remote mapping of GPS-denied underground mines using UAVs, including the case of autonomous UAV mapping of abandoned underground workings originating from the surface (Bishop, 2022). Bishop demonstrated the successful application of a photogrammetry survey of a 30 m (>90 ft) high limestone pillar using DJI Mavic 2 Zoom UAV that was modified with a custom-designed high-powered onboard LED

lighting system (on the right side of Figure 4). On the left side of Figure 4, the pillar surveyed in this study is shown and in the middle of Figure 4, the 3D high-resolution model of this pillar is shown. Bishop also demonstrated the horizontal photogrammetry surveying of a limestone pillar using a custom design 960 mm quadcopter with a DSLR camera mounted (Figure 5). Point clouds generated from the photogrammetry surveys were post-processed in Maptek's PointStudio software to extract discontinuities using the plane surface detection algorithm of the program.

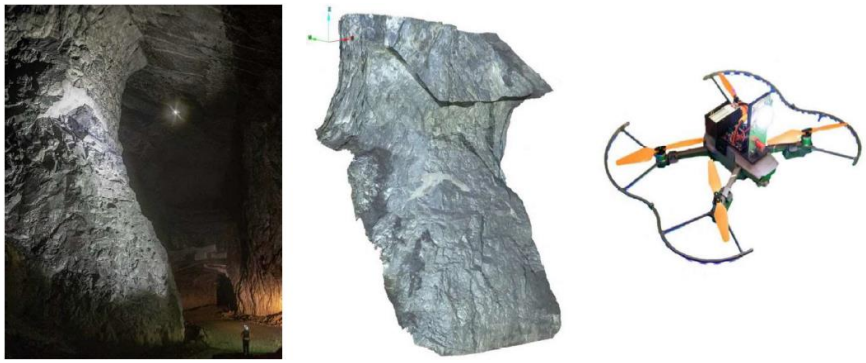

Figure 4 Drone-based pillar survey for photogrammetric modeling (after, Bishop, 2022)

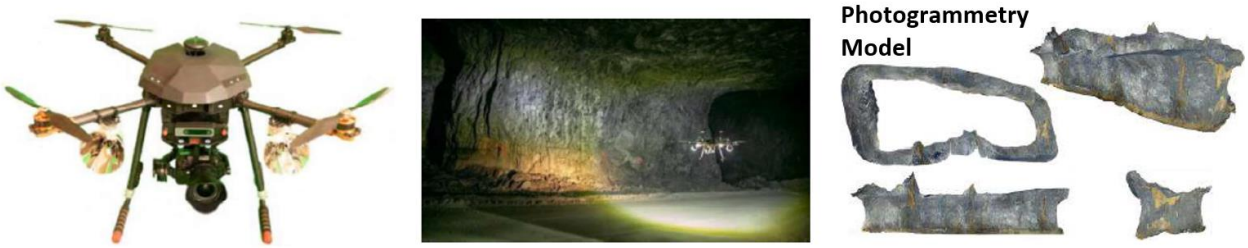

Figure 5 Photogrammetry survey of karst pillar (Bishop, 2022)

Bishop (2022) also demonstrated the autonomous mapping of the inaccessible areas of a limestone mine using the Exyn Technologies autonomous aerial robot. Like the WVU's unmanned ground vehicle (UGV) this autonomous robot can navigate and map underground openings, a great tool for mapping the underground mines. However, as seen in Figure 6, it is hard to identify the geological structure from drone LIDAR data. For this reason, WVU system uses UGV for autonomous navigation and provides additional lighting and power for the UAV, which is equipped with a higher resolution LIDAR camera, and surveys pillar autonomously, similar to the manually piloted photogrammetry survey shown in Figure 5. Details of this system are explained in the next section.

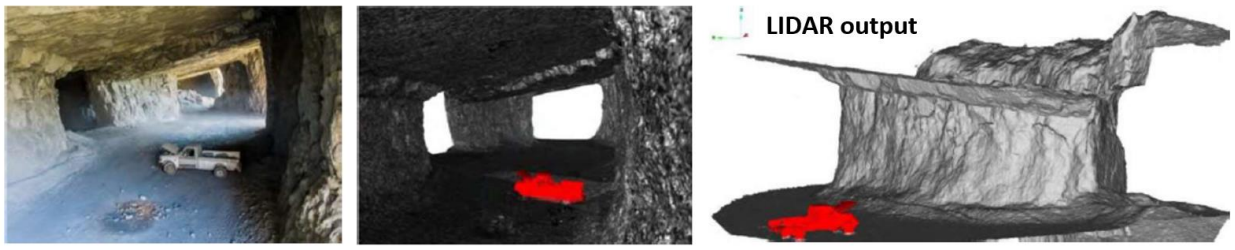

Figure 6 Survey conducted by Exyn Technologies autonomous aerial robot (Bishop, 2022).

WVU robotic system and relevant robotic research of robotic Co-PIs

WVU robotics team has been working on the development of an autonomous robotic system for several applications. In the current project funded by Alpha Foundation, it has been developed an ensemble of a ground robot (UGV) and a drone (UAV) for the inspection of stone mine pillars. The UGV allows fast autonomous mapping of a large-scale underground mine with limited needs for supporting infrastructures. The UAV is powered by a tether connected to the UGV for long-duration powered flights for performing a detailed inspection of the pillars of interest. A picture of the robotic system is shown in Figure 7. During the system operation, the UGV is responsible for autonomously navigating in the stone mine, performing mapping and localization using the onboard 3D LIDAR, stereo vision camera, and inertial sensors, and finding the pillar to be inspected by the UAV. Once the UGV carrying the UAV approaches the pillar to be inspected, it stops and commands the UAV to take off and survey the pillar. Each face of the pillar is then surveyed by the drone using a lawnmower pattern. Research on the design of the inspection pattern to achieve the best mapping was conducted (Samarakoon et al., 2022). After the pillar is inspected, the UAV lands back on the deck carried by the UGV, which then moves to the next pillar. So far, the UGV and the UAV were tested independently. In the middle of Figure 7, we show a test with an early version of the UAV flying autonomously in a stone mine, and on the right-hand side of the same figure, we show the construction of the high-resolution 3D model of the surveyed pillar. WVU expects to carry out a full system experiment by the end of this summer.

Figure 7 Robotic system developed for mining inspection. Left: the UGV with the UAV in the landing platform; Center: UAV autonomous surveying a pillar; Right: 3D photogrammetry model obtained from the survey.

Figure 8 shows a field test of the UGV in the NIOSH experimental mine. Similar to the Exyn autonomous aerial robot, the UGV can navigate and map the underground mine as shown in the bottom image in Figure 8. Autonomous mission times with the UGV (i.e., >4 hours) are significantly higher than any aerial robot, which allows it to operate and map deeper into a mine. Lights installed on the UGV also allow autonomous surveying of the pillars with a photogrammetry method, which produces RGB-colored high-resolution 3D maps.

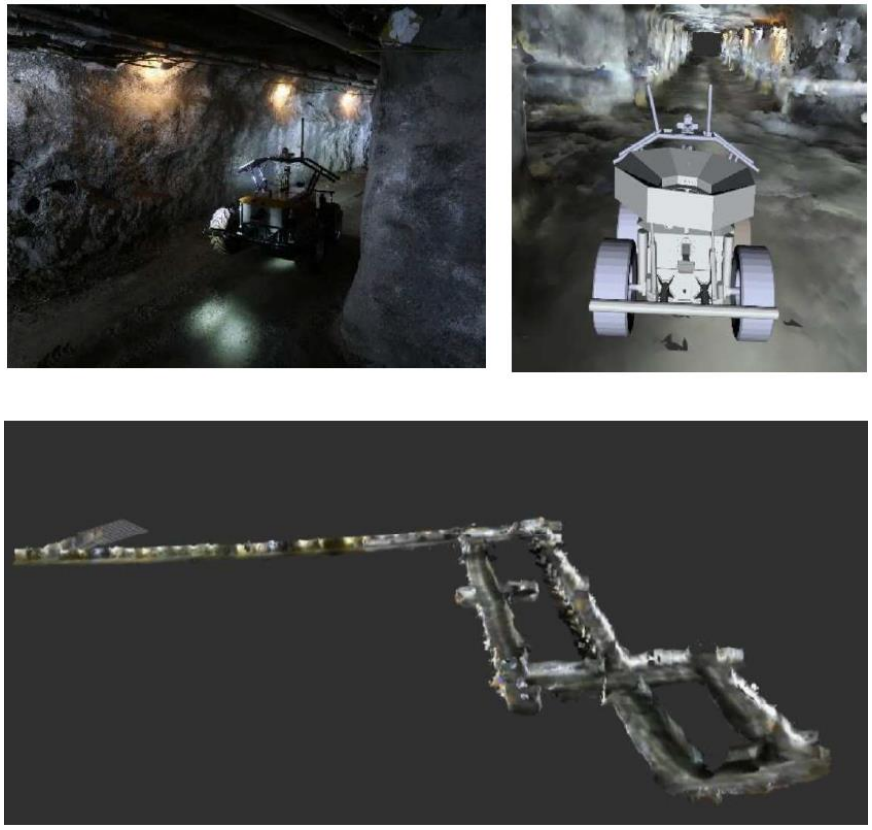

Figure 8. Maps generated by the WVU UGV, named Rhino, during an experiment in the NIOSH experimental mine

The experimental coal mine has significantly narrow room dimensions compared to stone mines. Ground condition in the experimental coal mine, during the test, was also hostile to robotic hardware, i.e., muddy ground and dripping water. The UGV was tested in the mine for hours without any problem, thus demonstrating the reliability of the system. The image on the top right-hand side of Figure 8 shows the data replay of the UGV in the virtual 3D map generated during the field tests. These simulations would also allow mine operators to plan and test autonomous mapping missions inside the virtual mine that is an accurate representation of the actual mine environment. It is important to note that both the Lidar based and Stereo Vision based SLAM software of the UGV can also be integrated to the UAV for single autonomous aerial missions.

2.3 Specific Aims and Research Objectives

The goal of this research was to reduce the occurrence of mine collapse and fall of ground related accidents in the underground stone mine industry through the development of guidelines for stone mine operators to evaluate pillar stability of old workings and roof fall hazards from UAV and/or UGV captured high-resolution 3D point clouds and geomechanical data. The collaborative project aimed to collect the necessary data from active stone mines by means of the existing autonomous UAV/UGV technologies and the expertise of VT and WVU teams while evaluating and improving the field performance of the WVU autonomous systems and integrating the WVU autonomous flight control software and operational sensory subsystems to commercial drones. While the problem is associated with pillar design in the underground stone mine industry, the techniques

and design guidelines developed in this project are adaptable to the underground metal and other nonmetal mining sectors. The following research specific aims were undertaken to achieve the research goal:

(i) Specific Aim 1: Develop a database of mine layout, rock mass characteristics, and high-resolution 3D maps of stone mine pillars and roofs in old workings while evaluating and improving the application of conventional UAVs of VT and autonomous systems of WVU.

(ii) Specific Aim 2: Develop guidelines for recognizing hazards that might increase the possibility of massive pillar and roof collapses through the analysis of the database.

3. Research Approach

The research approach consists of a field operation and data collection phase, a performance evaluation phase, a system enhancement phase, and the post-processing phase. During the field operation and data collection phase: VT and WVU teams visited and mapped different underground mines using VT's UAVs and WVU's autonomous systems. During each visit, the first objective was to gather a 3D map of the pillar layout and high-resolution 3D point clouds maps of the pillars and roofs. 3D point clouds were used in the post-processing phase to identify the geological structures on the rock mass. During the performance evaluation phase: the research team evaluated the operational performances and the successes/failures of the autonomous missions. The performance of each system was evaluated separately for each field operation. Objectives of this phase were: (i) to identify the potential bugs and shortcomings in the simultaneous localization and mapping (SLAM) and other related autonomy software, (ii) to determine the operational limits of each system, (iii) to identify the hardware or software components that limit the longer or more successful autonomous missions, and (iv) to evaluate the quality (i.e., quality of 3D maps for post-processing) of the measurement data. During the system enhancement phase: issues or potential improvements identified in the evaluation phase were addressed or implemented into the solution. The research team improved the WVU and VT autonomous systems in this phase to enhance the performance of each system for successful 3D mapping missions. During the post-processing phase: 3D point cloud data was processed to extract the geological structures on the rock mass, intact rock samples are tested, and rock mass for each case study local formation was characterized. In the final phase of this project, guidelines for recognizing hazards utilizing the analyzed data were developed.

4. Research Findings and Accomplishments:

4.1 Autonomous Mapping Technology

4.1.1 Summary of Previous Autonomous Mapping Technology Development

Unmanned Aerial Vehicles (UAV) and Unmanned Ground Vehicles (UGV) can be used to scan old workings and capture high-resolution 3D maps of these areas that can be used for assessment of pillar and roof damage, and stability. Previous research was aimed to develop an autonomous robotic system that is comprised of an Unmanned Aerial Vehicle (UAV) tethered to an Unmanned Ground Vehicle (UGV) and accompanying integrated hazard mapping approach for the assessment of stone mine pillar stability. This combination of remote vehicles was able to provide high-resolution 3D maps, which are then used as input for the assessment of stability. The main research accomplishments were: (i) the development of a proof of concept of a robotics system specifically for stone mine inspection, (ii) the development of a framework for integrating hazard mapping and boundary element modeling for the assessment of stone mine pillar stability.

An autonomous drone was improved along with this project from a legacy version developed in the previous project. While the focus of the previous project was the development of a tethering system able to power the drone from the ground vehicle, this project focused on the autonomous control and stability of the system components in the underground environment. To facilitate experiments for data collection, the drone was adapted to fly untethered which allowed for mine experiments without the requirement of the ground vehicle, where the drone's batteries are stored during a tethered operation.

4.1.2 Refinement and Enhanced Technology Development

4.1.2.1 Drone mapping improvements

To assess the performance of WVU drone mapping technology, early in the project, the team performed a quantitative evaluation of a SLAM-estimated map was performed using a controlled test object in a motion-capture facility. The test object was a toy climbing set shown in Figure 9, which was completely in a Vicon Motion Capture faculty with fiducials marked as the yellow climbing handles on the object.

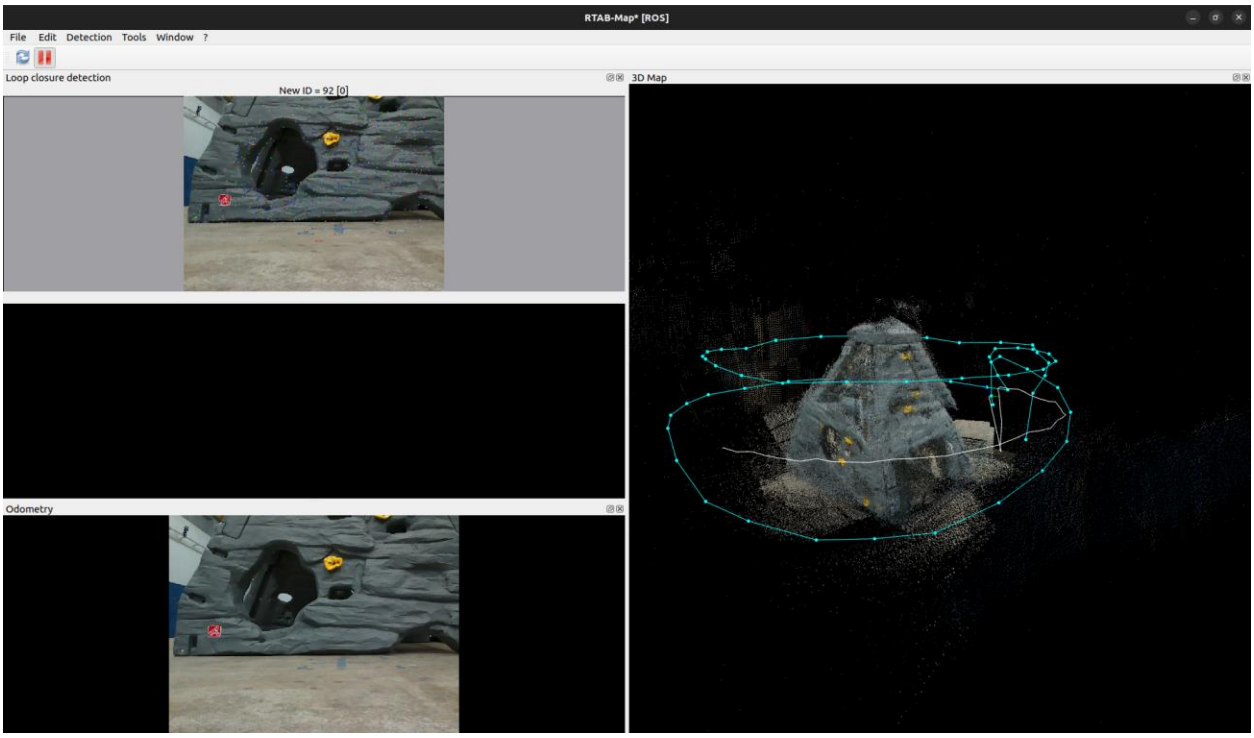

Figure 9 RTABMap generated map of test object in motion capture facility.

Stereo camera and LiDAR depth data were collected by flying a drone in the motion-capture room and processed using the RTAB-Map SLAM package. The drone was equipped with an Intel RealSense T265 stereo camera and an Intel RealSense LiDAR Camera L515. The L515 provided RGB and depth data, while odometry information was obtained from the T265 camera.

Visual inspection of the generated map against the yellow hand-hold features on the test object showed that some portions of the map were skewed and that some structures were duplicated. These inaccuracies were assumed to be largely due to odometry errors. Comparison plots between the T265 odometry and motion-capture ground truth, shown in Figure 10, were produced, and numerical odometry error values were reported. The RMS 3D position error was 0.43946 m, with a maximum error of 1.06759 m.

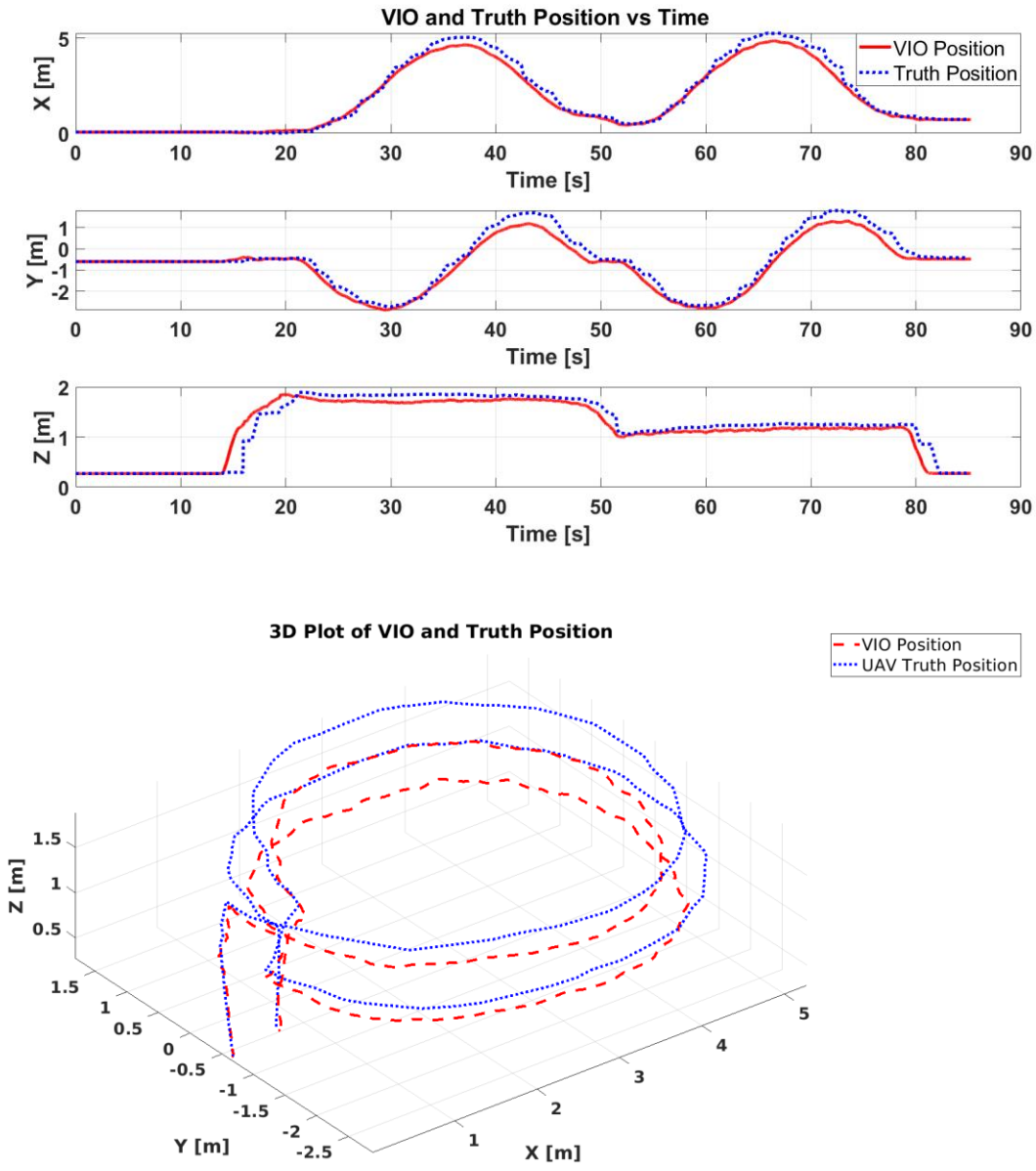

Figure 10 T265 odometry used for SLAM map compared with the ground truth

To evaluate the estimated map, distances between features in the map were compared to the corresponding distances in the ground truth. The selected features were the yellow hand-holds on the test object. Ground-truth feature positions were obtained by tracking reflective VICON markers in the motion-capture system. To detect the same features in the SLAM map, a ROS2 node was created to filter the point cloud by color, and Euclidean clustering was used to compute the centroids of the resulting clusters.

Correspondence between detected map features and ground-truth features was determined using Iterative Closest Point (ICP), followed by Euclidean distance matching, as shown in Figure 11. The model contained nine features of interest, while thirteen features were detected in the estimated map, indicating the presence of duplicate features. Duplicate features were identified as those farthest from their matched ground-truth features. The sum of the squared error of the distances between ground-truth feature pairs and map feature pairs was 0.1903 m.

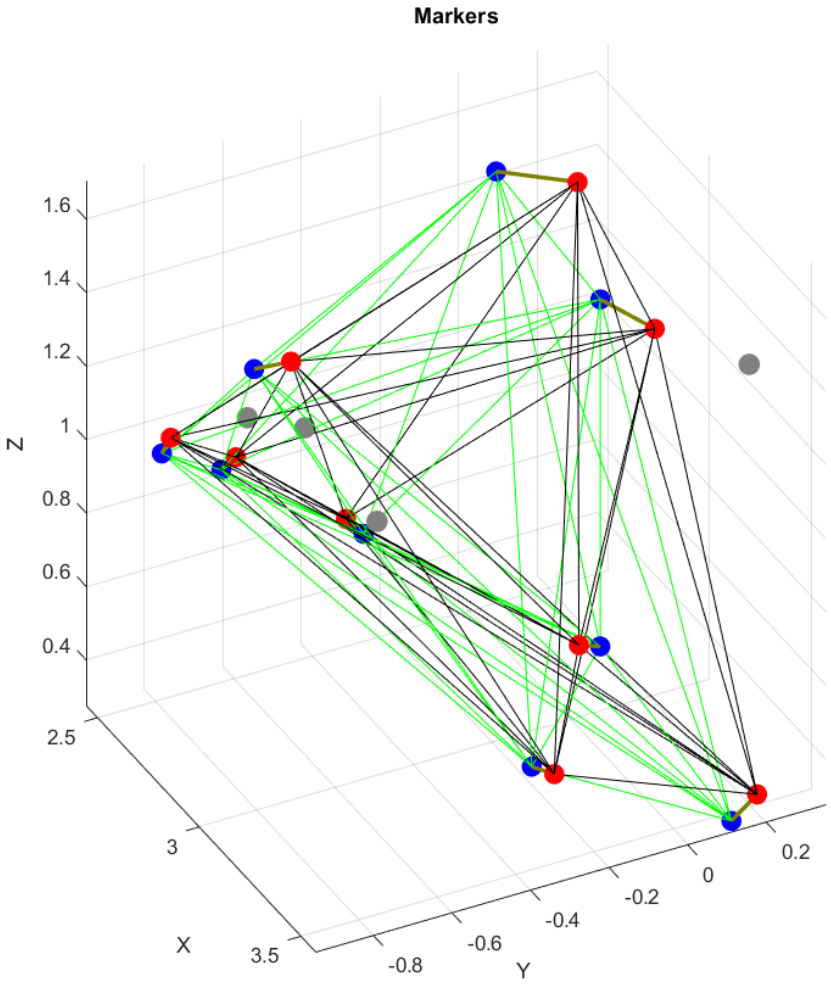

Figure 11 Correspondence between ground truth features (red) and features detected in the map (blue/grey)

4.1.2.2 Autonomous flight control software integration for a commercial drone

The drone developed on the project is based on the Holybro X500 V2 drone, shown in Figure 12a. The frame of this drone is made with full carbon fiber twill, with carbon fiber tube arms supported

by fiber-reinforced nylon connectors. The drone is controlled by the Pixhawk 6C flight controller. To fulfill the basic requirements of the project, the drone was modified to include propeller guards, several sensors (described below), lights, and an Intel i7 Nuc12 computer for autonomous onboard control. To power these accessories, the drone was equipped with DC/DC converters and a series of electronic circuits called "ideal diodes", which are installed in parallel to each other and allow the drone to be connected to several power sources at the same time, including batteries and a tether. In fact, only one of these power sources would power the drone, since the ideal diodes select the source with higher voltage. This configuration proved to be very useful in mine experiments, since it allows the drone to fly with two batteries and also enables the hot swapping of batteries. With hot swapping, a battery change can take a few minutes, since the system does not need to be reinitialized every time the battery needs to be replaced. Based on this standard configuration, three versions of the drone were developed along the duration of the project.

Figure 12 (a) Basic drone platform used in the project; (b) Mine Drone V1, equipped with a T265, L515 and Teratower laser sensor.

The first version of the drone, shown in Figure 12b, was based on the Oxpecker UAV, which is a tethered drone developed in the previous project. It uses a PX4 flight controller, which receives and processes information from multiple inertial measurement units (IMU) and a compass. Additionally, a distance sensor is used to control the height. The pilot controls the illumination using the remote controller, which is necessary for the camera and payload. The flight controller also receives command inputs and odometry information from the onboard computer. The onboard computer is connected to a RealSense T265 camera, a L515 LiDAR and camera, and a Teratower array of distance sensors. It uses the T265 camera to feed Visual Inertial Odometry (VIO) to the flight controller, records data from the L515 LiDAR, and leverages the Teratower array along with the drone state to navigate. A control station running QGroundControl is used by the pilot on an Android tablet. Through this station, the pilot can interact with the flight controller, adjust parameters, and monitor real-time information such as relative position, battery status, and sensor status. The pilot can also start and stop the drone. Finally, a ground computer connects to the onboard computer to launch software packages for VIO, start and stop data recording, and control automated flight sequences.

Figure 13 Mine Drone V2, with an extended frame and oversized propellers, equipped with a full Teratower array and independent front and downward-facing light sources, and carrying a RealSense D455 as payload.

The second version of the drone, shown in Figure 13, was physically modified to support wider propellers, increasing payload capacity and flight time through powerful motors. An optical flow sensor was added to estimate relative velocity and position. Since optical flow requires some light, a downward-pointing LED was installed. Additionally, information from the ceiling-pointing sensor was incorporated. The onboard computer received multiple software updates. The software was polished and improved so that it no longer relies on VIO. Therefore, this version does not require the onboard computer for flight, only to record mapping data. Because no specific camera is needed, we included the option to record with multiple payloads, which include any realsense camera or LiDAR.

The third and final version of the drone, shown in Figure 14, includes a 360° Livox LiDAR capable of operating in the dark, while remaining light enough to be carried by the drone. The onboard computer computes the drone's odometry in real time and feeds it to the flight controller. For automated sequences, only three point distance sensors plus the ceiling sensor were retained. This version is capable of flying without the onboard computer, since all other sensors are still active, but the computer, necessary to process LiDAR data, is recommended in very low light environments. Without the LiDAR the drone becomes unstable in dusty, low light conditions.

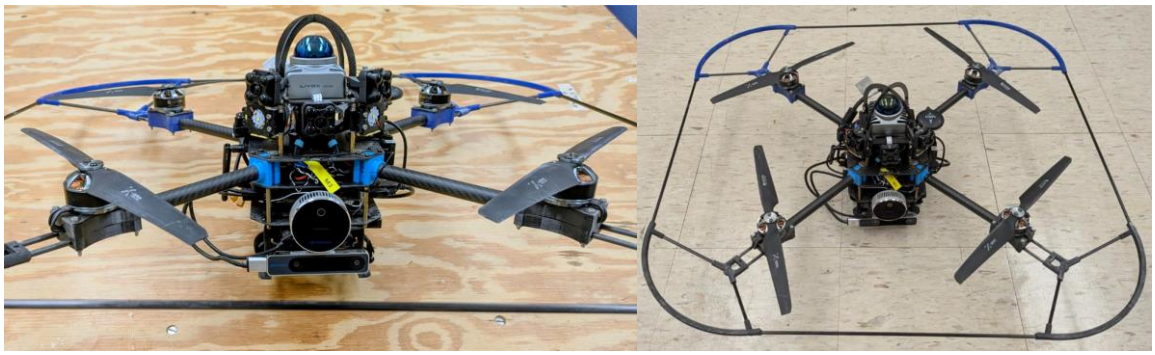

Figure 14 Mine Drone V3 with the same hardware as V2 but with a 360° LiDAR added on top. The Teratower array was removed, retaining only the front- and downward-facing sensors. Payload is interchangeable depending on the task.

Figure 15 shows the system arquitecture of the three versions of the drone. It is important to mention that, while the drone was improved from V1 to V3, all three versions were successful used along this project for data collection.

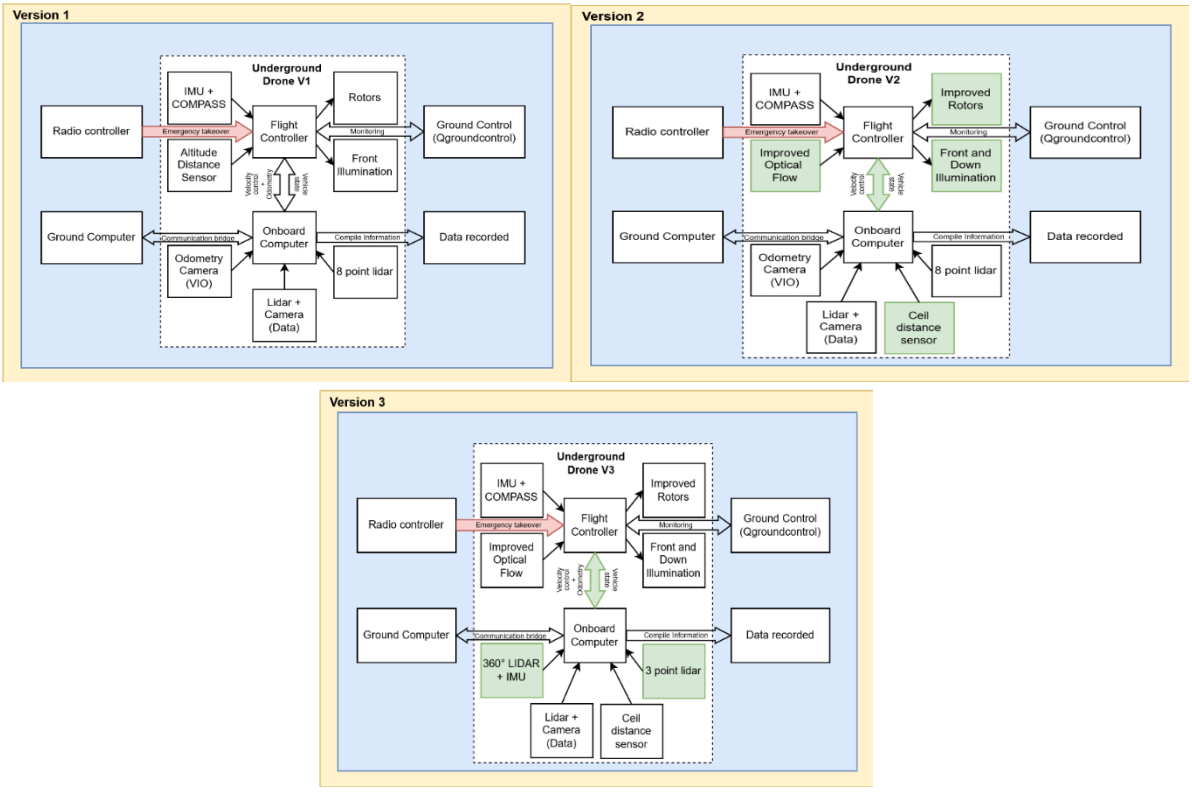

Figure 15 Arquitecture of the three drone versions developed in this project.

The final version of the drone does not require the onboard computer for flight, since it can maintain stable flight using its own sensors. However, in harsh conditions—especially in dark or dusty environments—additional inputs are used to calculate its position, enabling both manual and autonomous stable flight. The drone supports different payloads depending on what is connected and selected in the software. The Livox LiDAR is the primary and recommended sensor for flying underground in low-light conditions. The RealSense T265 camera provides odometry independently and is recommended when lighting conditions are sufficient. Since T265 cameras are no longer in production, we incorporated a VIO package called OpenVINS, which supports multiple cameras for odometry calculation. We tested OpenVINS with binocular cameras such as the RealSense D455, T265, D435, and a monocular camera L515, ensuring compatibility with these odometry sources. Additionally, the L515 LiDAR was primarily used to record detailed data of the pillars. Figure 16 summarizes the payload options of the drone.

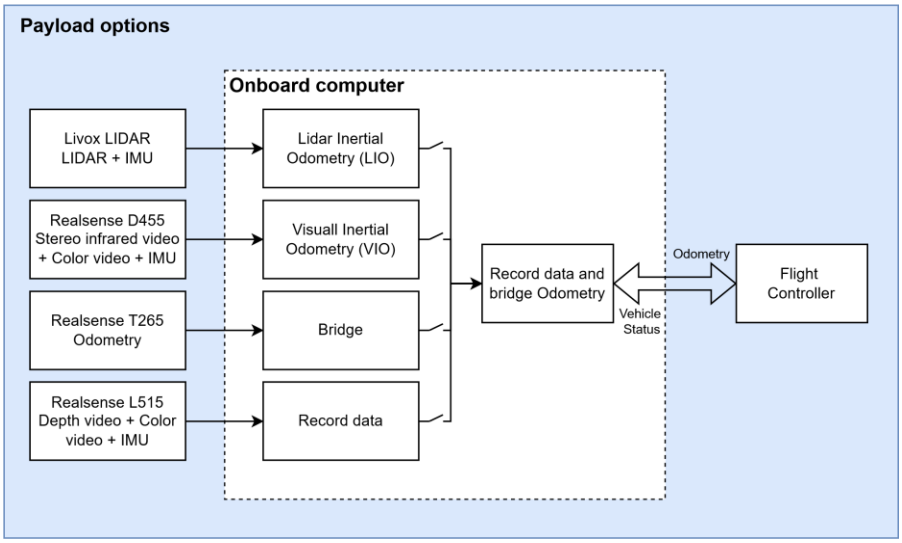

Figure 16 Several payloads can be used with drone. Some payloads are only used for data collections but a few of them can also be used to improve the stability and control fo the drone.

Software

The drone can be piloted manually by an operator or can perform its tasks autonomously. The use of LiDAR and cameras along VIO software connected to the drone's flight controller as a replacement for GPS sensors makes the drone very stable and easy to be operated by any user, including people with low experience with UAV control. To allow this, the computer on the drone relays information (x, y, z coordinates and heading with respect to the takeoff location) from the VIO software to the drone's controller (Pixhawk). During our experiments, we noticed that, in a few situations, sensor noise and/or excess of processing tasks caused errors and delays that could destabilize the drone. We observed, for example, that a delay in computing the orientation of the drone with respect to the pillar could cause the drone to turn too fast and lose track of its orientation, especially when its camera rapidly points to a dark corridor of the mine, where no features can be viewed by the camera. To solve this issue, which was not very frequent but had the potential to be catastrophic, we decided to add backup sensors. In this way, even if the computer on drone stops working completely, the drone's controller can still stabilize the drone using an optical flow sensor (ARKflow) pointing to the floor, which also provides the height of the drone.

In autonomous mode, the drone is able to scan a pillar without human intervention. Besides the sensors and software used for stabilization (LiDARs and/or cameras with VIO), it uses simple software that relies on 4 single-beam laser range sensors (3 at the front and one pointing up) and the height sensor. With these sensors, the software of the drone, which is very light and efficient due to the small amount of data to be processed, is able to 1) keep the drone parallel to the pillar during, 2) detect the corners of the pillar, 3) control its height and distance to the ceiling. The drone is then able to execute the following tasks autonomously:

1. Follow the face of a pillar (left or right): Using the 3 distance sensors pointing to the front, two variables are calculated: 1) the yaw relative to the pillar, and 2) the distance to the wall. For the distance to the wall only the information of the front sensor is used, and for yaw the differences between the alpha_1 and alpha_2 angles (see Figure 17) is computed and adjusted in real time. Once distance and yaw are calculated, the relative velocity to move left or right relative to the wall is calculated and sent to the drone controller.

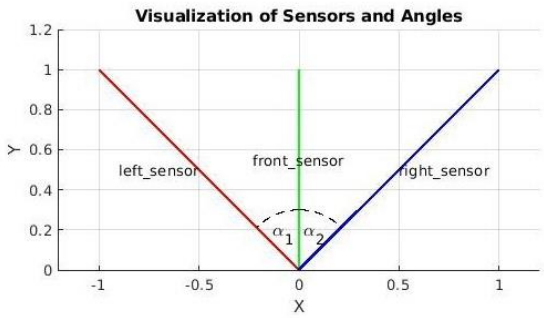

Figure 17 Sensor information used to follow the face of the pillar and detect corners.

4. Scan wall: This task scans a full wall in a back-and-forth motion, with incremental intervals. For this mission, a corner recognition algorithm is implemented by using the same measurements of the 3 pointing front sensors (Figure 17). Once a corner is detected, the next states to lift up and move in the contrary direction are activated.

Experiments

By performing several experiments at WVU's motion capture facility, WVU's simulated mine, and in an actual stone mine, we observed satisfactory performance of the vehicle and its behavior, even in situations with excess of dust and complete absence of light. Figure 18 shows snapshots of a manual and an autonomous pillar inspection being performed by the drone. A typical drone trajectory along the pillar face 3D reconstruction obtained by the drone in autonomous mode is shown in Figure 19. The reconstruction of a complete pillar, when drone flew manually around the pillar is shown in Figure 20.

Figure 18 Manual (left) & Autonomous (right) inspection of a stone mine pillar with the drone.

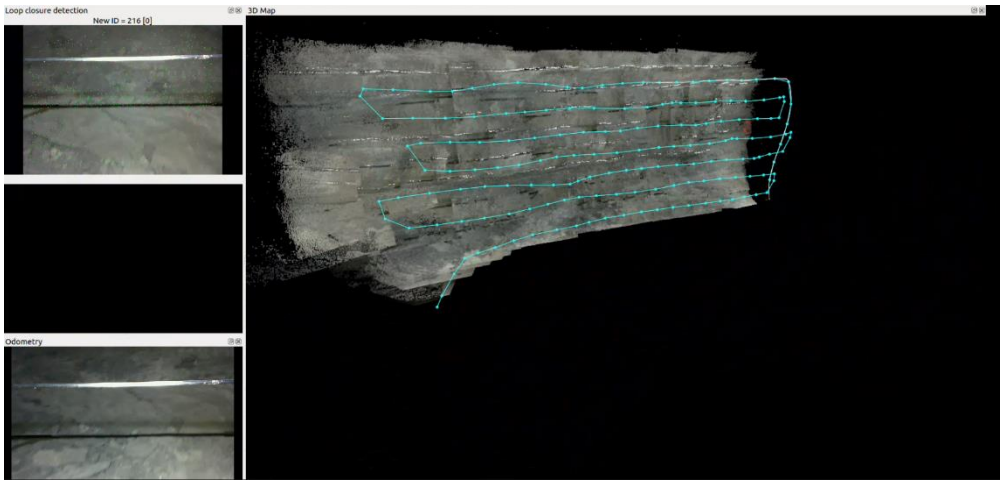

Figure 19 Drone trajectory in autonomous mode during a pillar face mapping operation.

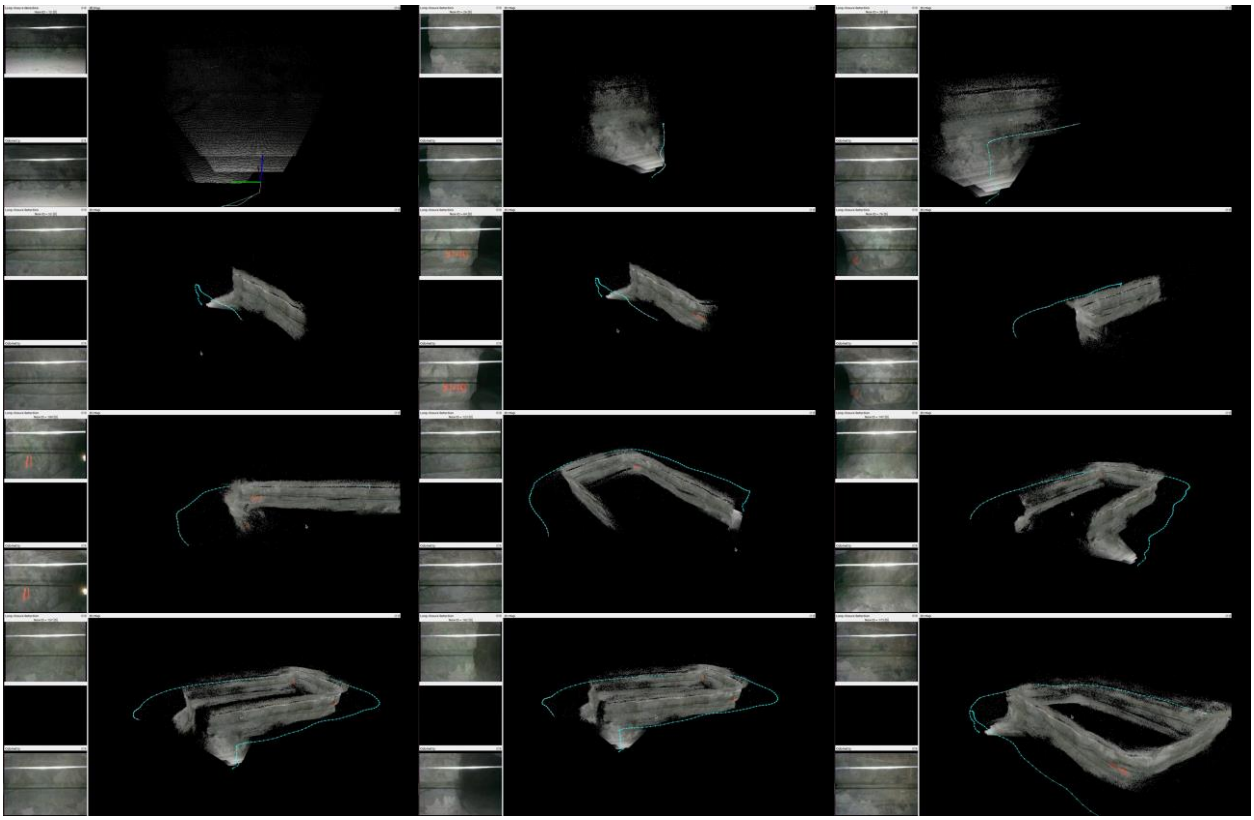

Figure 20 Pillar reconstruction in manual mode.

To expand upon this result, additional field and university testing were performed. On February 14, 2024, field data for mapping tests were conducted at a limestone mine in Ohio, shown in Figure 21. Camera image data was collected from one section of the mine wall while flying a drone equipped with an Intel RealSense T-265 stereo camera and an Intel RealSense LiDAR Camera L515. Using the collected data and RTAB-Map, a map of the mine wall was generated as shown in Figure 22.

Figure 21 Mapping test on the Ohio mine wall

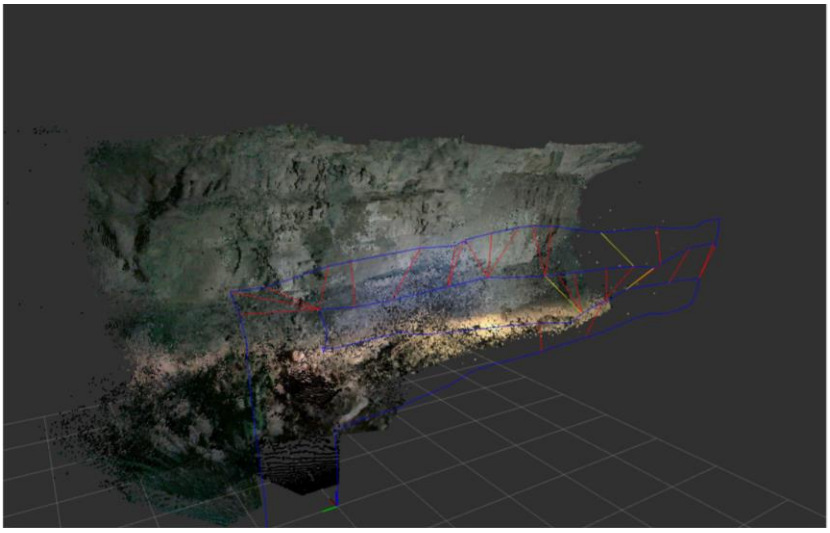

Figure 22 RTABMap output of the Ohio mine wall

Relocalization Framework

The mapping and quantitative evaluation performed using the toy climbing set was an initial attempt at environment mapping for this project and led to the subsequent development of a point-cloud registration-based relocalization approach. This focused on the development of a point-cloud registration framework for relocalization in subterranean environments. Relocalization is defined as the process of re-establishing a robot's position within an environment when external

positioning information is unavailable or lost. Subterranean environments are described as challenging due to limited external positioning information, poor lighting, irregular and non-distinct surfaces, and dust interference.

The framework, summarized in the flowchart shown in Figure 23, registers a target point cloud to a previously stored source point cloud map. This framework and proceeding work was published in a conference proceedings article in April 2025 (Akhihiero and Gross, 2025):

Intrinsic Shape Signatures (ISS) are used to select keypoints in both point clouds, and Fast Point Feature Histograms (FPFH) are used to compute descriptors. Descriptor matching provides correspondences, from which an initial three-dimensional transformation is estimated. This transformation is refined using Normal Distributions Transform (NDT), followed by Iterative Closest Point (ICP) registration.

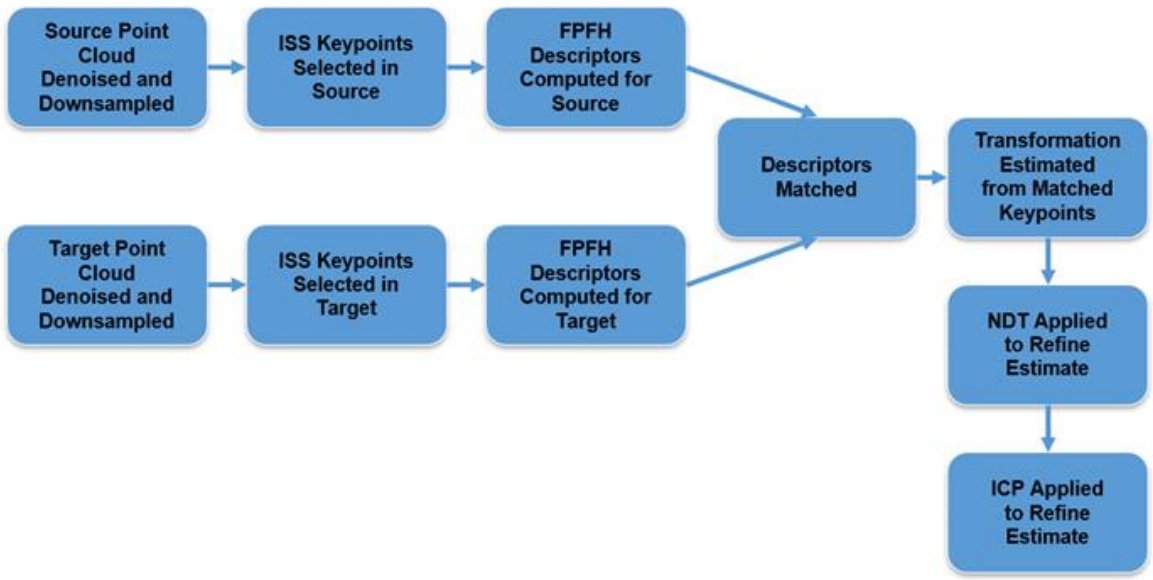

Figure 23 Flowchart for Relocalization Framework

The framework was evaluated using data from a ROS/Gazebo simulated mine, as shown in Figure 24, Figure 25, a physically simulated coalmine, and a real limestone mine, as shown in Figure 26 and Figure 27. The real mine was the limestone mine in Ohio.

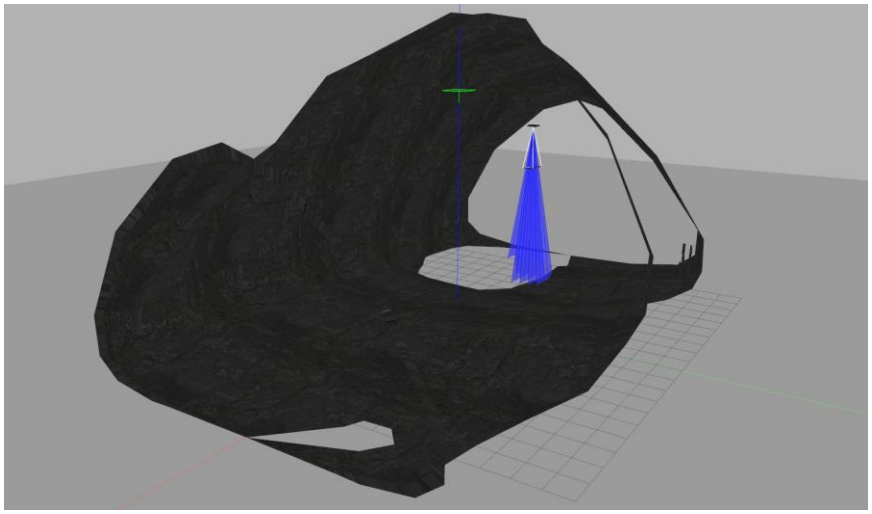

Figure 24 Gazebo simulator

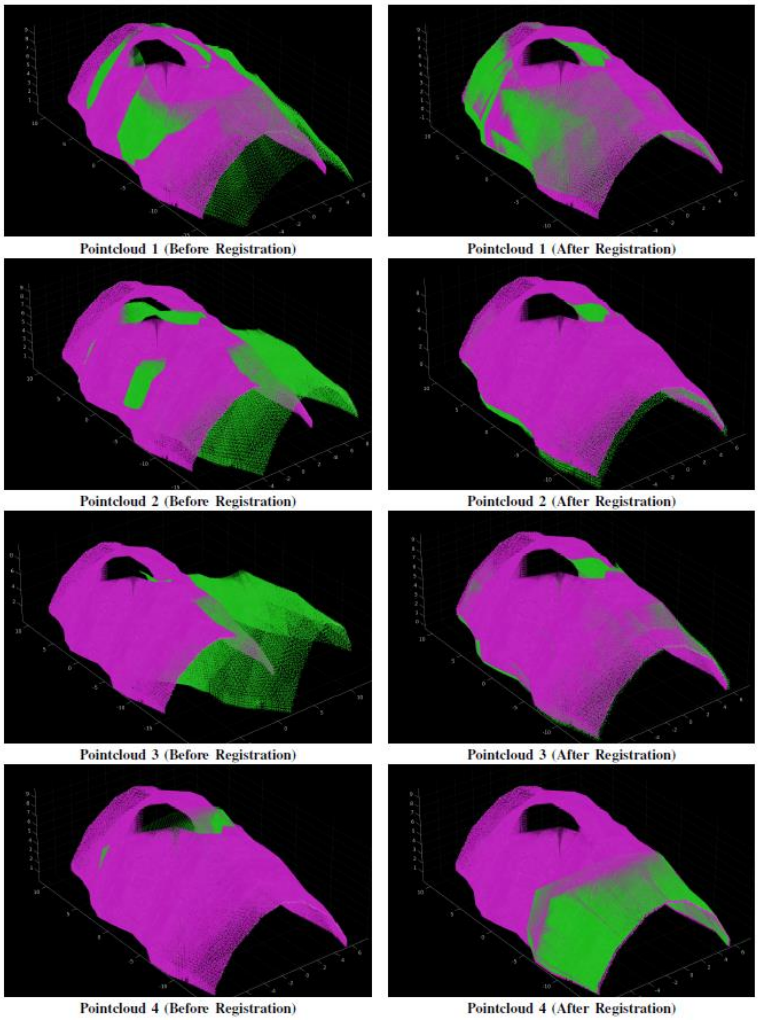

Figure 25 Pointclouds before and after registration using the full framework. The source pointcloud is in magenta and the target pointcloud is in green.

Figure 26 Both test environments: the physically simulated coalmine (left) and the actual limestone mine (right).

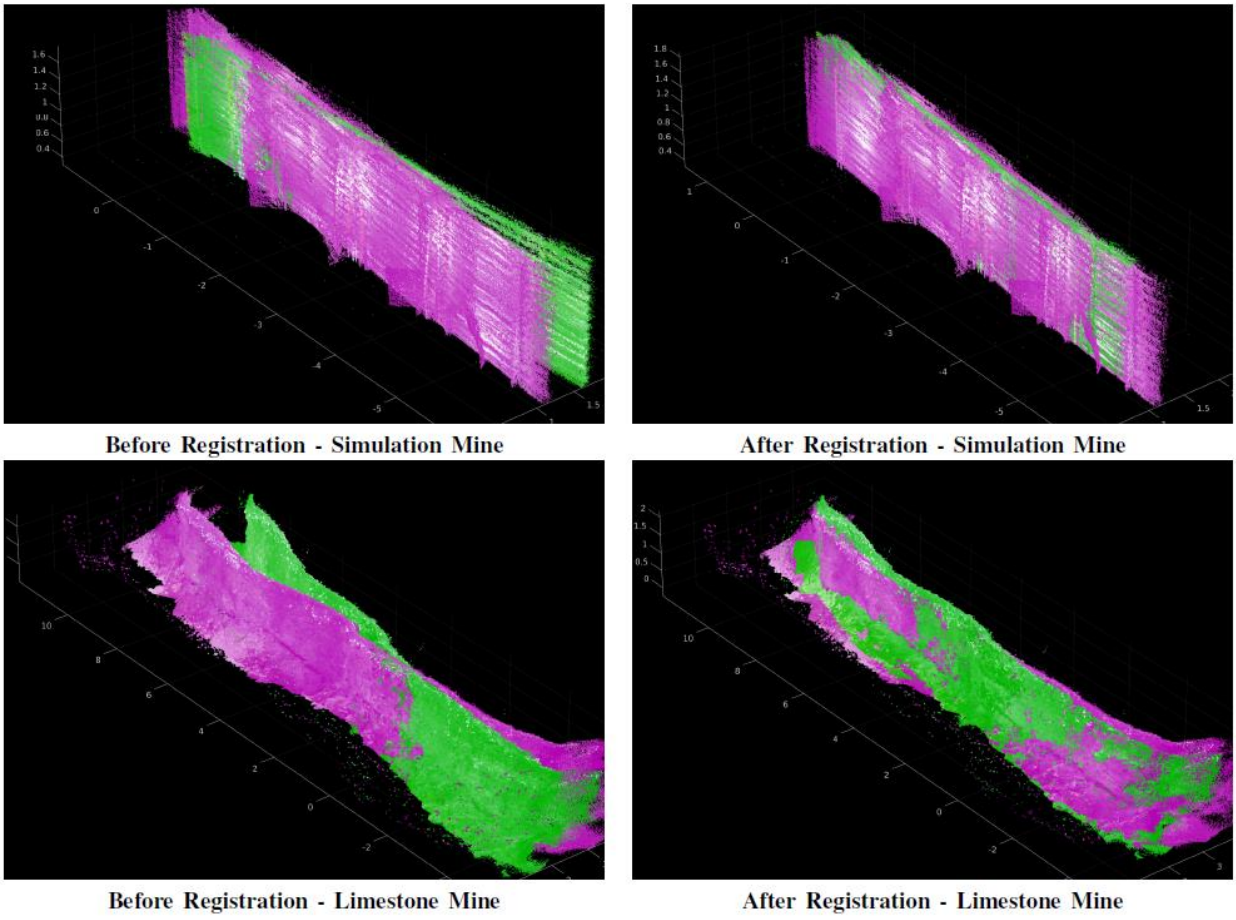

Figure 27 Point cloud registration results: (Top) Simulation mine before and after registration. (Bottom) Limestone mine before and after registration. The source pointcloud is in magenta and the target pointcloud is in green.

Registration performance was assessed using root mean square error (RMSE) and inlier percentage metrics as shown in Table 1 and Table 2. These results were published in the IEEE/ION PLANS 2025 conference (Akhihiero and Gross, 2025).

Table 1 Registration Performance for Different Framework Configurations for Gazebo Simulation Environment

Framework Configuration	Pointcloud 1 RMSE (m)	Pointcloud 1 Inlier %	Pointcloud 2 RMSE (m)	Pointcloud 2 Inlier %	Pointcloud 3 RMSE (m)	Pointcloud 3 Inlier %	Pointcloud 4 RMSE (m)	Pointcloud 4 Inlier %
FPFH Only	0.1253	86.59	0.1068	90.55	0.2722	33.97	0.2472	78.26
FPFH + NDT	0.0988	88.8	0.0909	89.32	0.1504	87.61	0.1365	89.35
FPFH + ICP	0.1231	87.94	0.0993	89.94	0.2329	57.28	0.2394	88.12
NDT + ICP	0.2432	70	0.1965	77.78	0.2817	43.03	0.1938	68.51
FPFH + NDT + ICP	0.1114	89.11	0.1324	87.21	0.1226	87.8	0.182	89.33

Table 2 Registration Performance in a Physically Simulated Coalmine and Real Limestone Mine (Ohio)

Framework Configuration	Simulation Mine RMSE (m)	Simulation Mine Inlier %	Limestone Mine RMSE (m)	Limestone Mine Inlier %
FPFH Only	0.1325	99.99	0.0703	99.96
FPFH + NDT	0.0173	99.97	0.0751	99.98
FPFH + ICP	0.0196	100	0.0651	99.98
NDT + ICP	0.0403	99.96	0.1398	98.9
FPFH + NDT + ICP	0.0173	99.97	0.0941	99.91

4.1.2.3 Unmanned Ground Vehicle improvements

Building on prior work in autonomous exploration and underground mapping, the team focused on the deployment of a robust UGV system, referred to here as Rhino, and the associated autonomy and mapping algorithms required to operate in real stone-mine environments. Field experiments were conducted in representative underground mines to demonstrate end-to-end autonomous exploration and mapping.

The Rhino platform was specifically engineered to support long-duration, autonomous operation in underground mine environments. A wheeled, skid-steer configuration with four large-diameter wheels was selected to maximize traction and energy efficiency over uneven mine floors while

maintaining mechanical simplicity and reliability. A split-body chassis with an articulated joint allows all wheels to remain in contact with the ground, improving mobility over rubble, ruts, and mild elevation changes commonly encountered in stone mines.

The platform is instrumented with a 3D lidar, cameras, and an Inertial Measurement Unit (IMU) for perception and navigation in GPS-denied environments. High-capacity lithium-ion batteries were selected to enable multi-hour missions, allowing the robot to traverse large underground areas and collect continuous datasets suitable for structural analysis. All electronics, sensors, and enclosures were designed with dust, moisture, and vibration tolerance in mind, reflecting lessons learned from previous underground deployments. The resulting system provides a stable and repeatable sensing platform for acquiring high-resolution geometric data of mine pillars and surrounding voids.

Autonomous Navigation and Mapping Algorithms

Reliable autonomous operation in old stone mines requires tightly integrated state estimation, terrain analysis, planning, and mapping. Rhino employs a LiDAR–inertial simultaneous localization and mapping (SLAM) framework based on factor-graph optimization, enabling accurate pose estimation and map construction despite wheel slip, uneven terrain, and intermittent perceptual degradation. The SLAM system fuses IMU pre-integration and LiDAR odometry to produce real-time pose estimates and globally consistent 3D point-cloud maps.

For navigation, Rhino uses a layered autonomy architecture, as shown in Figure 28. A terrain analysis module continuously evaluates local traversability by analyzing LiDAR returns in a voxelized representation around the robot, identifying obstacles, drop-offs, and non-traversable regions. A local planner generates dynamically feasible trajectories toward commanded waypoints, while a path-following controller executes smooth motion at low speeds appropriate for confined underground spaces.

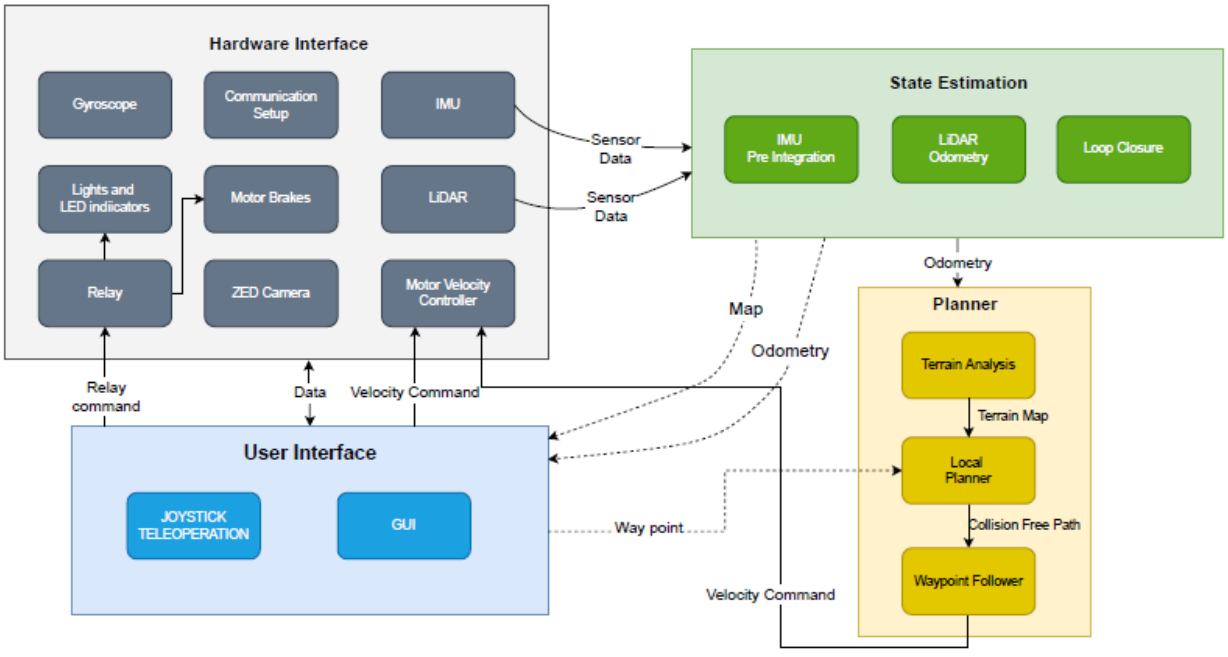

Figure 28 Rhino's systems software architecture, where grey is the hardware interface module, green is the state estimation module, yellow is the planner module, and blue is the user interface module.

Exploration and waypoint selection (Figure 29) are managed autonomously using a semantically guided exploration strategy originally developed and validated in underground environments. Rather than relying on pre-defined maps or teleoperation, the robot incrementally selects new viewpoints at the frontier of the explored region, prioritizing areas that maximize new surface coverage while maintaining safe distances from obstacles and pillars. This capability is particularly important in room-and-pillar mines, where large open spans can lead to perceptual aliasing and navigation ambiguity if not managed carefully.

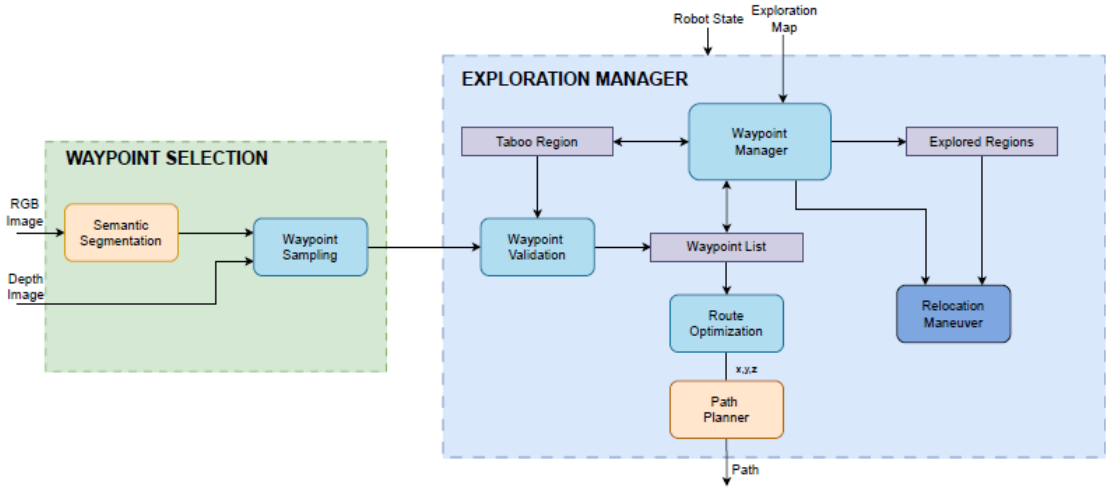

Figure 29 Rhino's overall exploration framework

Field Visits and Mine Deployments

Field experiments were conducted in multiple underground mine environments representative of old stone workings, including the NIOSH experimental mine and limestone mines with regular pillar spacing. These sites present realistic challenges such as low lighting, dust, standing water, reflective rock surfaces, and long corridors with minimal geometric variation.

During each deployment, Rhino was initialized at a safe entry point and operated in a predominantly autonomous mode. The robot navigated through the mine, incrementally extending its exploration region while building a dense 3D point-cloud map. Human intervention was limited to safety oversight and occasional recovery actions in the event of hardware or environmental anomalies, providing a realistic assessment of autonomous performance. The resulting datasets include high-resolution point clouds capturing full pillar cross-sections, wall surfaces, ceilings, and floor geometry over extended distances.

Mapping Results and Lessons Learned

The autonomous mapping runs successfully produced continuous 3D reconstructions of mine interiors including interconnected networks of corridors and pillars (Figure 30, Figure 31, Figure

32). Dense LiDAR coverage enabled near-complete surface capture of pillars, even in areas with limited line-of-sight, as the robot naturally acquired data from multiple viewpoints during exploration. The consistency of the SLAM solution across long traverses allows relative measurements between pillars, supporting comparative assessments across different regions of a mine.

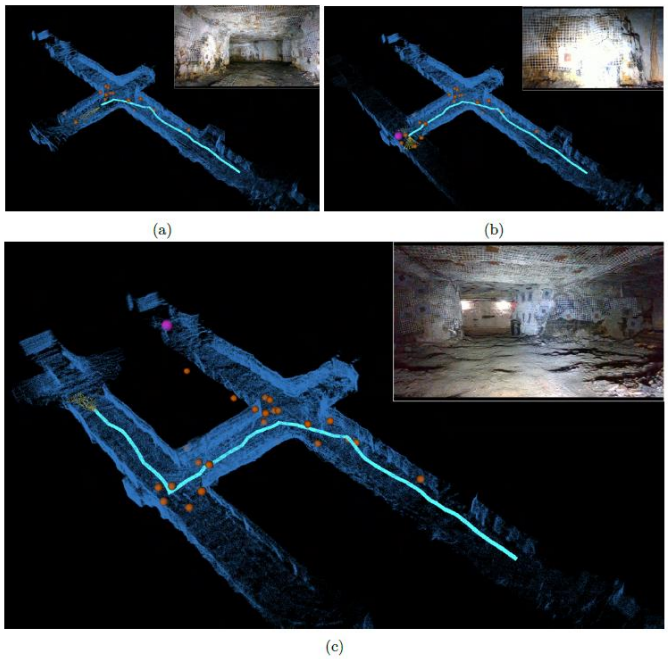

Figure 30 Rhino performing the Semantic-Guided Viewpoint Exploration, the blue point cloud represents the map constructed by the robot, the light blue line depicts the path traversed, and the orange spheres the sampled viewpoints.

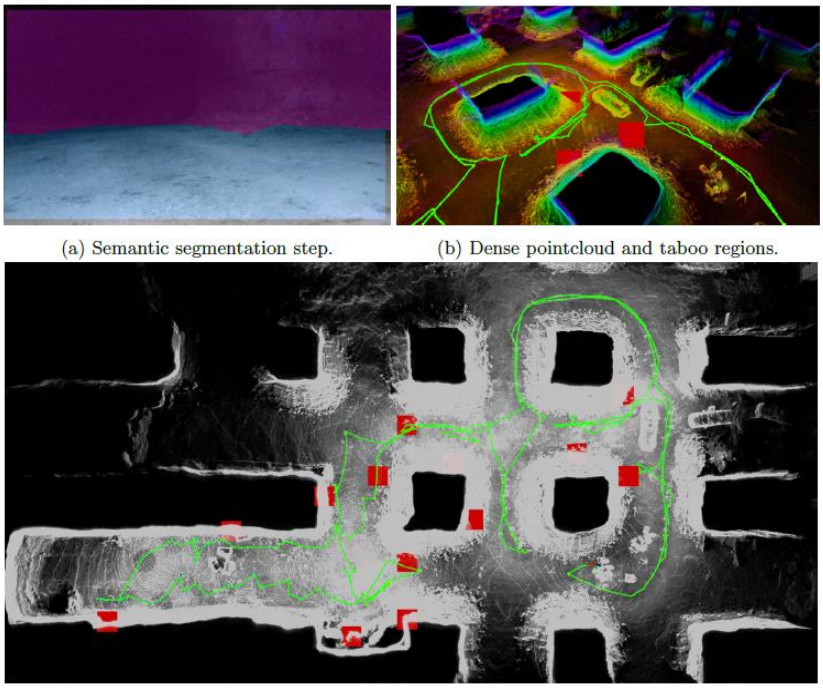

(a) Semantic segmentation step. (b) Dense pointcloud and taboo regions.

(c) Exploration map with green line representing the robot's path and red squares the taboo regions.

Figure 31 Semantic-Guided Viewpoint Exploration in the limestone mine environment.

Field testing also highlighted practical considerations for future deployments. Hardware robustness proved critical, as prolonged operation in confined spaces places sustained mechanical loads on drive components. Lighting conditions and airborne dust affected camera and Lidar perception, reinforcing the importance of developing a robust robot perception system.

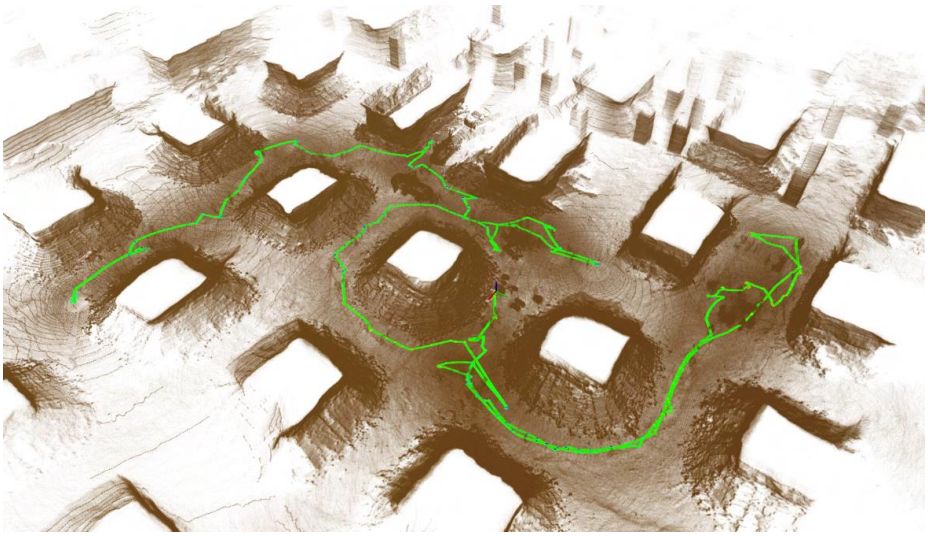

Figure 32 A large scale mapping of the stone mine. The brown pointcloud shows the map built from the LiDAR, and the green line is the robot's trajectory.

4.1.2.4 Roof inspections and mapping

To support a more complete mapping system on the drone, while not a complete solution for roof (ceiling) inspection, a LiDAR–camera SLAM approach was also adopted using FAST-LIVO2. Visual SLAM alone can be unreliable in mine environments due to poor lighting and limited visual features on the drone. Incorporating LiDAR information as well provides more robust odometry and geometric coverage, while the camera supplies color information, resulting in a map that captures both structure and appearance, as shown in Figure 33, a colored map of the Ohio Limestone mine.

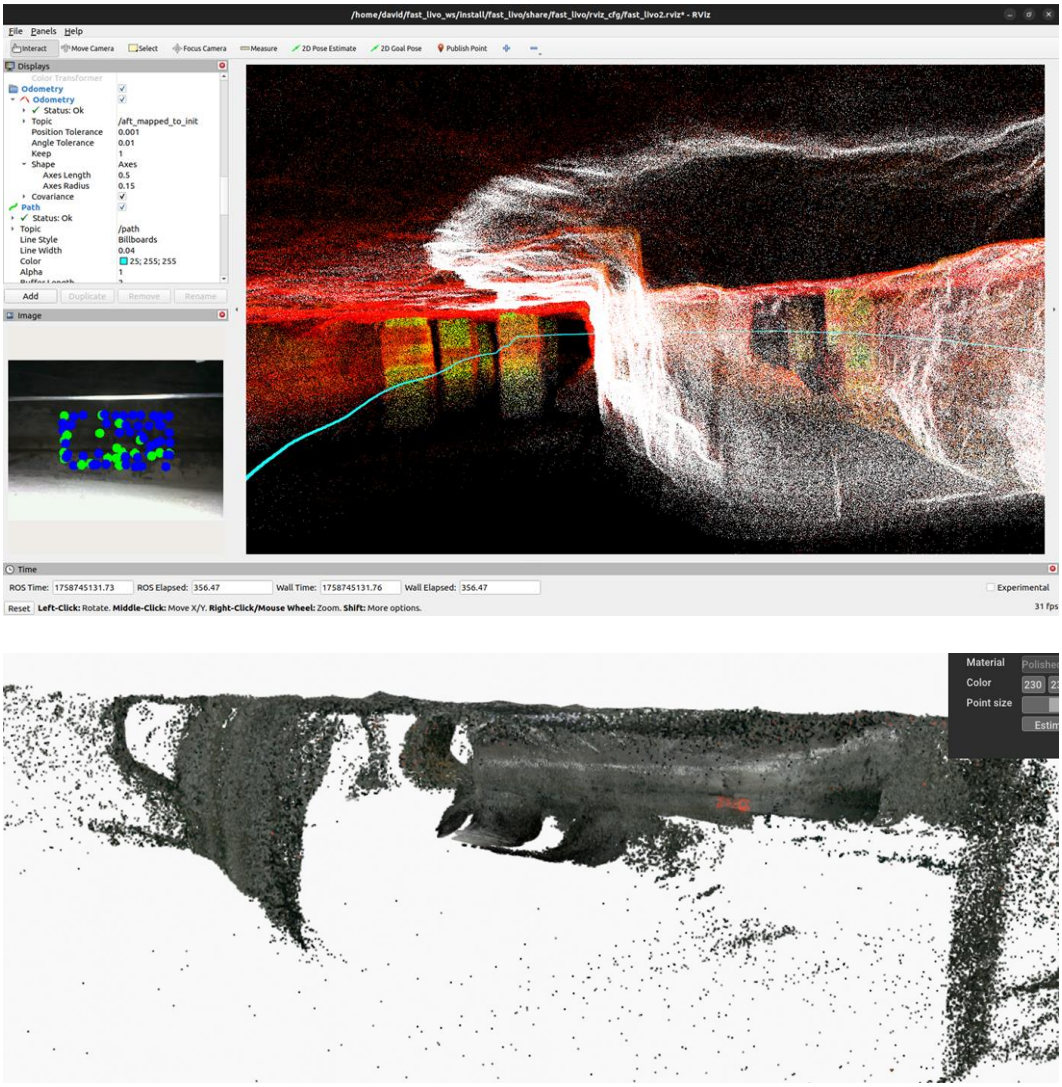

Figure 33 LiDAR-Camera SLAM output of the Ohio Limestone Mine

Several tests using a Virginia Tech drone equipped with LiDAR and high-resolution photogrammetry was deployed in one of the case study mines in east Tennessee to inspect the roof and roof bolts in an older section of the mine as seen in Figure 34. Supervisors can use these outputs to verify support installation against ground-control plans, prioritize scaling or

rehabilitation, and target bolting crews to specific problem areas rather than relying solely on manual visual checks. Drones can allow for increasing inspection coverage throughout the mine and provide repeatable digital records for tracking roof conditions over time.

Figure 34 Drone-based roof & roof bolt inspection

Another LIDAR scan was carried out in the aftermath of a roof fall (Figure 35). The collected information can be used to determine the volume of roof that collapsed, even more accurately if an earlier scan is available for change detection. Around the roof fall, the failed roof bolts can also be located as seen in Figure 35. This is possible even if there are no light sources available. When filtered for intensity, it is possible to locate intact roof bolts (Figure 36) that can be automated to estimate bolt spacing and possible unsupported areas with missing bolts.

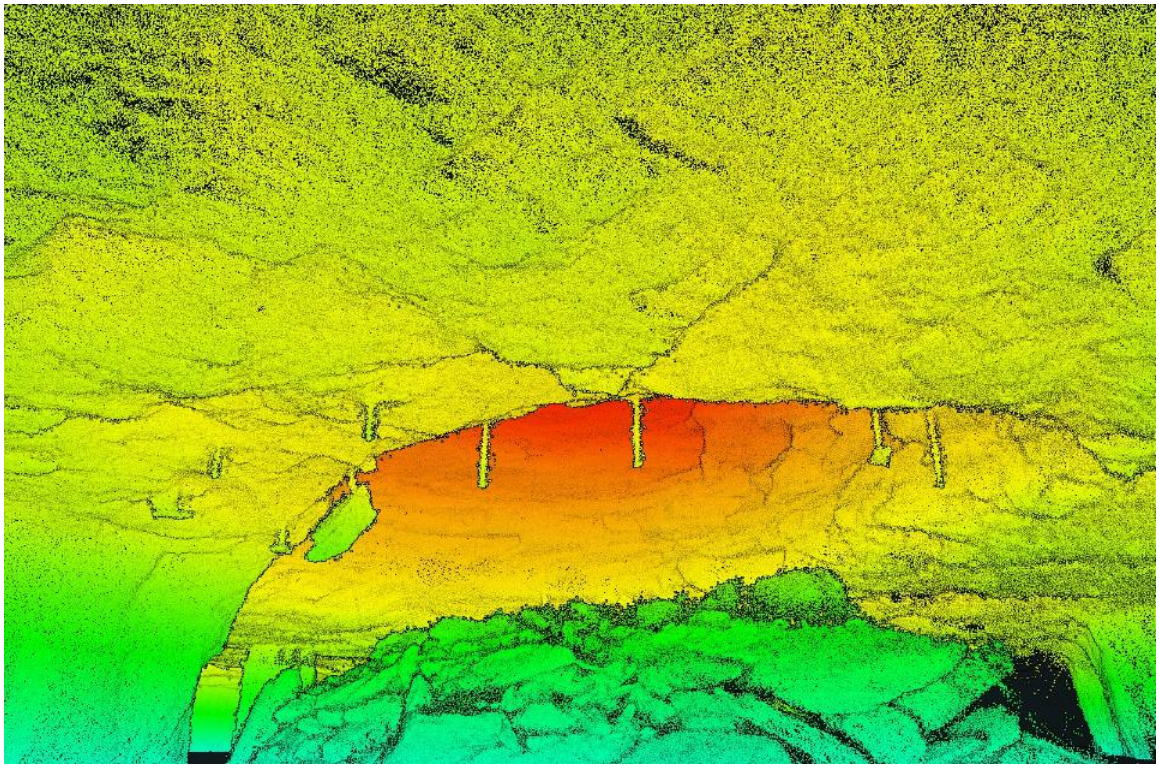

Figure 35 LIDAR scan of a roof fall

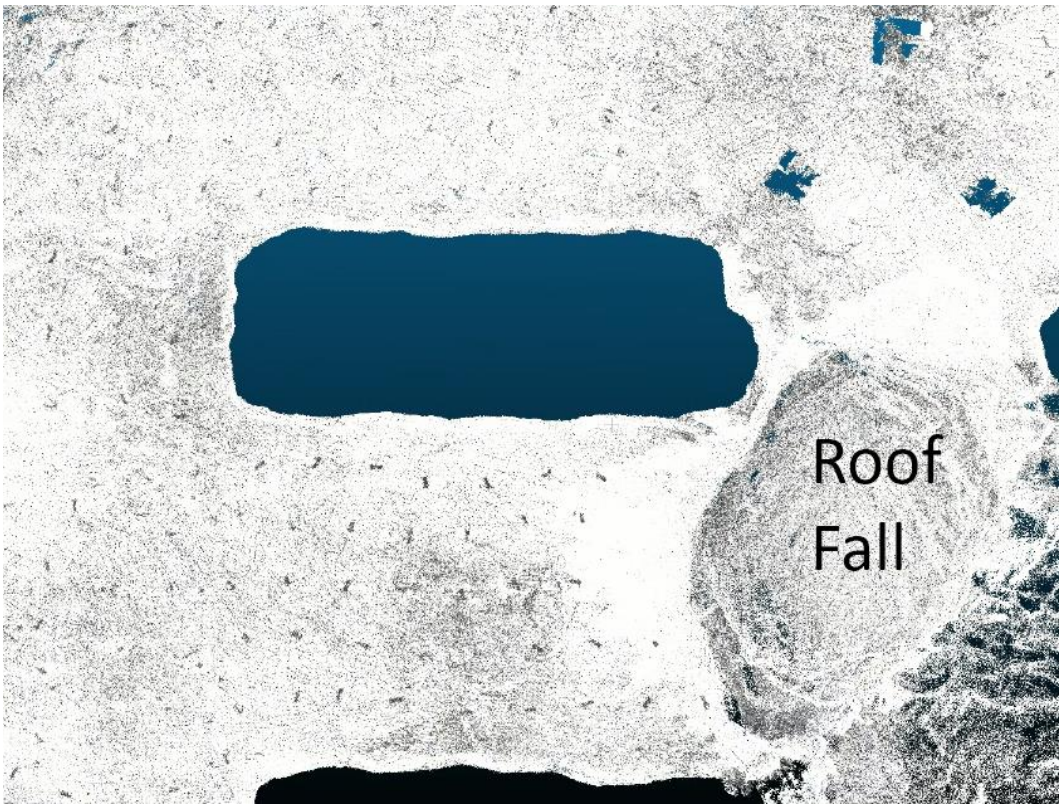

Figure 36 LIDAR scan filtered for intensity to locate roof bolts

4.2 Mine Visits and Data Collection

Over the course of the project, multiple active room and pillar limestone operations were visited, as well as a room and pillar zinc mine. These mines spanned Virginia, West Virginia, Tennessee, Kentucky, and Ohio (Figure 37). The sites offered opportunities to assess the performance of mobile LiDAR and photogrammetry-based mapping systems under varying ground conditions, dust levels, lighting environments, and access constraints, while also gaining an understanding of the operational challenges at each individual site.

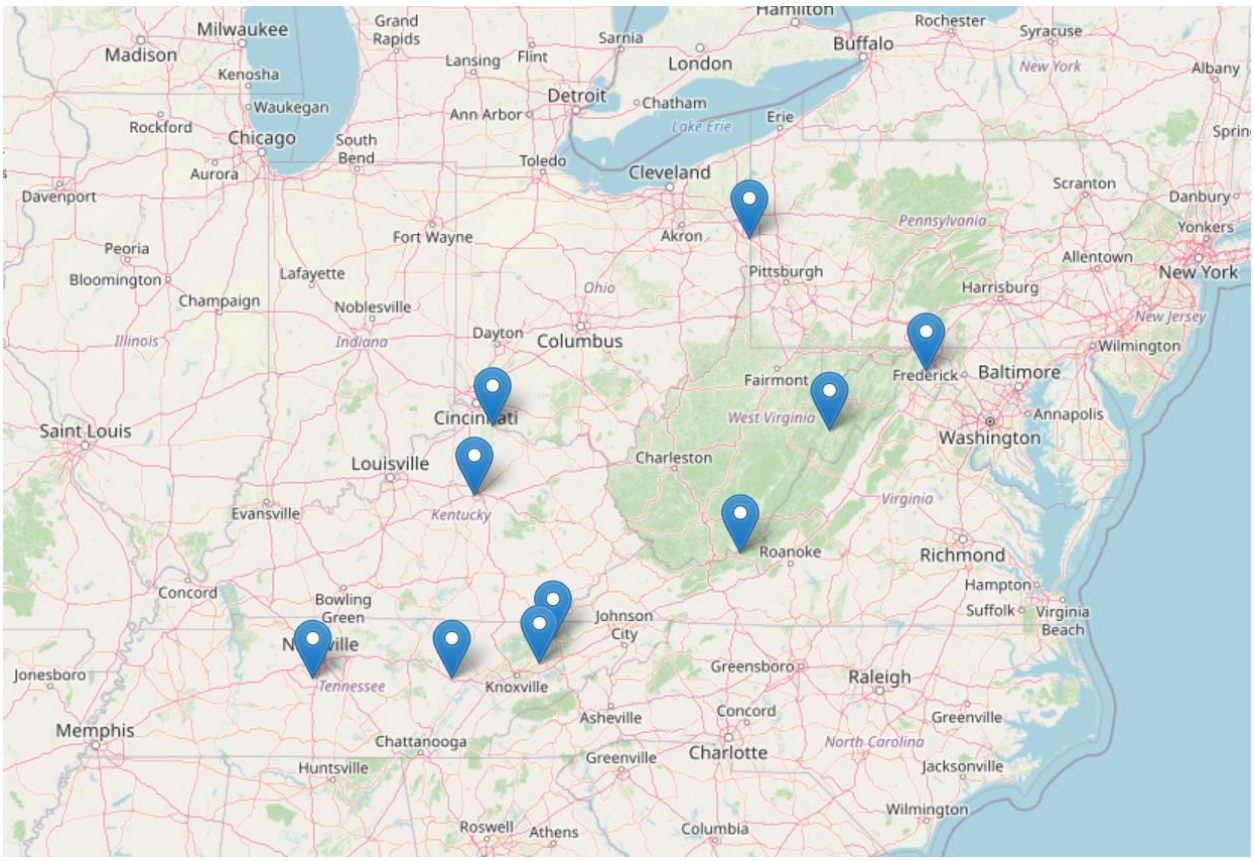

Figure 37 Site visit locations

Where permitted by the company hosts, high-resolution 3D data was collected to capture geometry, rib and roof conditions, and structural features such as joints and bedding. These datasets were used to generate detailed point clouds that can be used to support volumetric analysis, convergence assessment, and geotechnical characterization. Beyond validating sensor performance, the site visits facilitated close collaboration with mine engineers and operators, providing practical insight into how rapid underground mapping can enhance situational awareness, support ground control evaluations, improve ventilation planning, and inform production optimization in the mines. Collectively, the field deployments demonstrated the applicability of advanced 3D mapping technologies as tools for improving safety and efficiency of operations, through the creation of digital models.

Virginia Tech made a site visit to a stone mine in east Tennessee on June 7th, 2023 to assess the mine and introduce the project to mine personnel. No drone flights were conducted during this initial visit, but several terrestrial lidar scans were taken as seen in Figure 38.

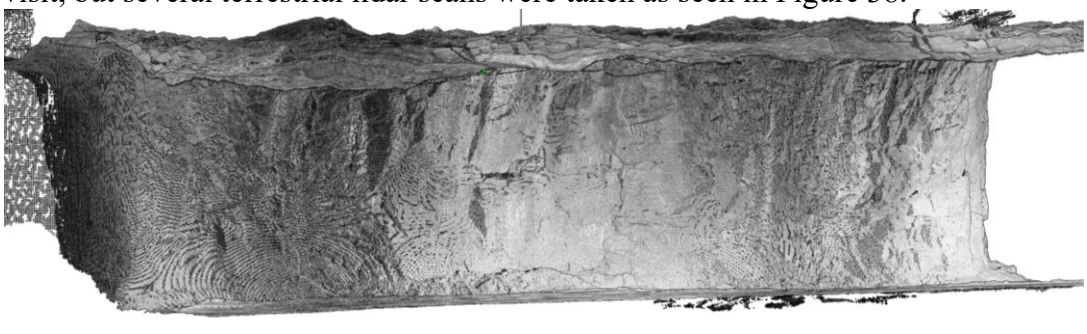

Figure 38 Faro terrestrial LiDAR scans at the Carmeuse Luttrell Mine in east TN

Several visits were made by the Virginia Tech team to a mine located in Ripplemead, VA. Most of the previously mapped areas of the mine have been made inaccessible due to the operations shutdown, except for one previously visited area on the 8th level of the mine. Initial testing focused on new UAV systems deployment underground, including a Yuneec H520 hexacopter as seen in Figure 39. A carbon fiber cage, also pictured in the figure, was added to the drone to add a layer of safety around personnel. The lack of optical flow sensors made position-hold without GPS difficult, further exacerbated by the additional weight and position of the guarding and lighting system. As a closed-system that is out of production, modification has become a challenge and efforts have turned to focusing on the DJI systems already at Virginia Tech as well as the Pixhawk-based systems that were built.

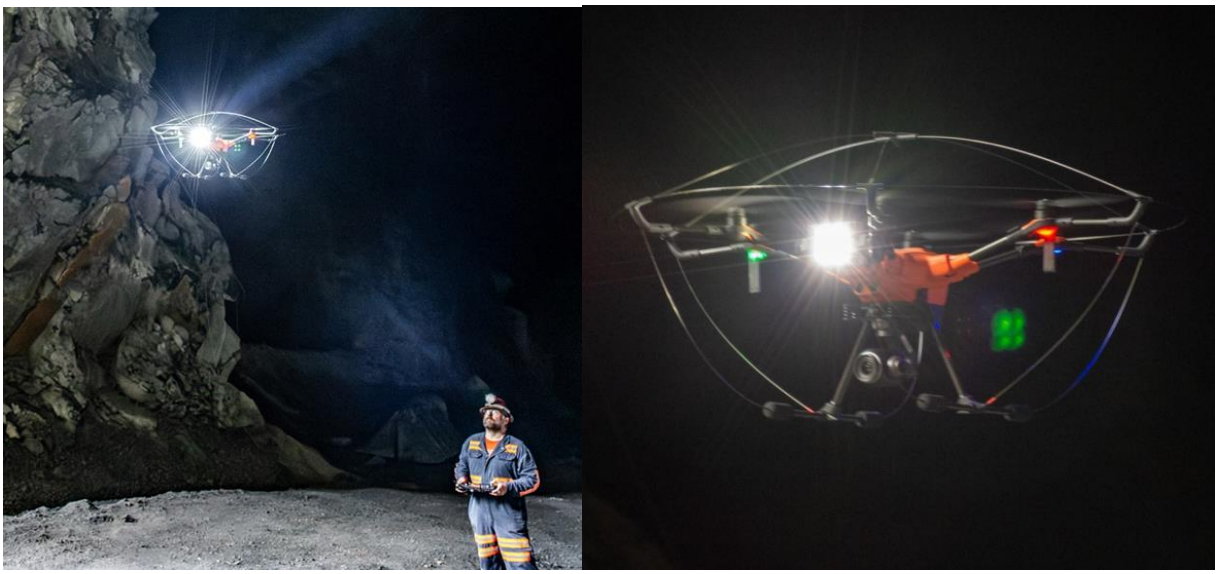

Figure 39 Consumer-grade Hexacopter Testing at the Mine

The best results achieved to date from a manufactured drone were with the DJI M300 system. A couple of different payloads were added to the system to enhance performance underground, including a radar system and a gimbal-mounted LED light as shown in Figure 40.

Figure 40 Drone Lighting & Photogrammetry Testing at the Mine

On a third visit to the same mine, the initial SLAM calibration of the LiDAR sensor was tested. Several mobile lidar scans were performed on the surface, down the primary ramp and through the secondary escapeway, and throughout the lowest accessible sections of the mine as seen in Figure 41.

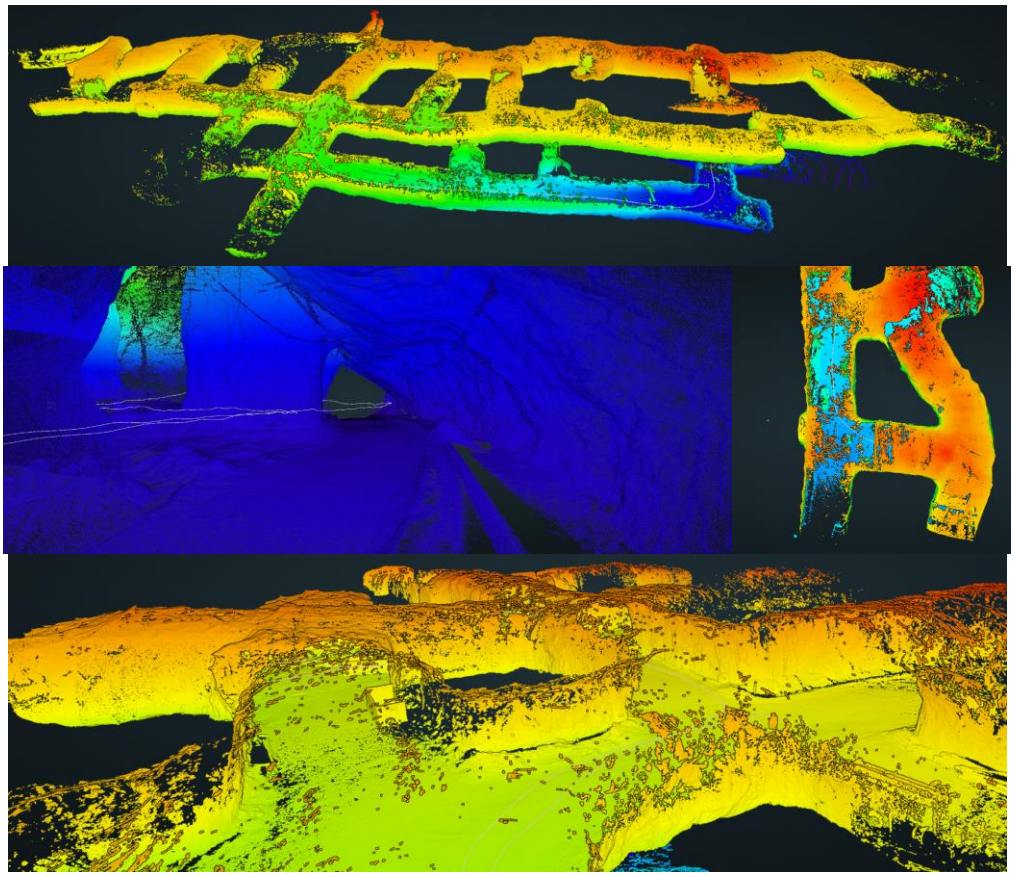

Figure 41 LiDAR SLAM at the Mine performed by Virginia Tech

A visit was made to a mine in east Tennessee on April 18th, 2024. The mine was the site of a massive pillar collapse in 2021. The mine is an underground room & pillar limestone mine with 15 m x 15 m pillars, but with historical pillars of more than 30 m in height. Previous

studies have noted areas with poor roof conditions displaying joint separation and blasting-related stress-induced cracking (Kurre & Walton, 2020).

Figure 42 Example mine pillars at a limestone mine in east Tennessee

Figure 43 Boundary of mine cave-in from 2021 collapse of multiple pillars

Baseline lidar scans have been made by company personnel. An initial pillar photogrammetry model was captured on the first visit as seen in Figure 44.

Figure 44 Initial pillar photogrammetry model at east Tennessee mine

A cement operation in Martinsburg, WV was visited previously in 2020 and 2021 when initial site surveys were conducted. Virginia Tech resurveyed this operation again in November 2024. Quarrying operations began at the site around 1900 for high-calcium limestone for lime products and later transitioned to an underground mine. The mine is now a large surface open pit with a cement plant capacity of 2MM tons per year. As the surface pit continues to expand to the southwest, it is intersecting historical workings from the underground mine as seen in Figure 45.

Figure 45 Surface & Underground Workings at Argos Cement in Martinsburg, WV

LiDAR scans were collected using the Exyn Nexys LiDAR system onboard a DJI M350 quadcopter of both the surface pit and of several drifts and crosscuts underground. Additionally, aerial images were collected of the surface pit for photogrammetric modelling. Virginia Tech used reflective targets for the LiDAR ground control points (GCP's). A DJI D-RTK 2 GNSS was used as a real-time kinematics (RTK) base station for the drone and a Trimble GNSS surveying tool to mark the GCP's as seen in Figure 46. The GCP's are being used to align the aerial scans and underground scans to each other and the mine map.

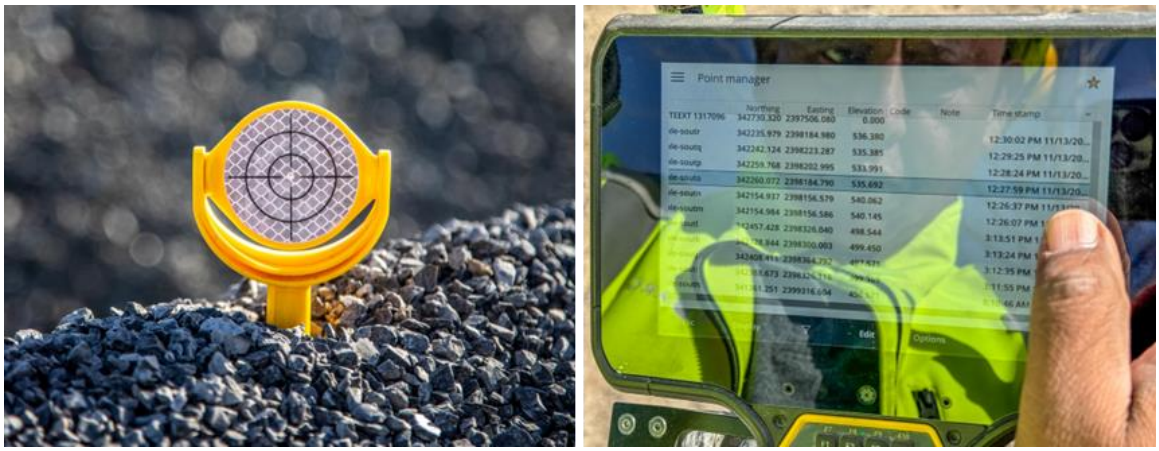

Figure 46 Ground Control Points for LiDAR Scans

Initial point clouds are included in Figure 47 and Figure 48. Rock samples were collected from the Argos Martinsburg limestone mine in West Virginia for laboratory testing to determine the parameters for pillar strength studies.

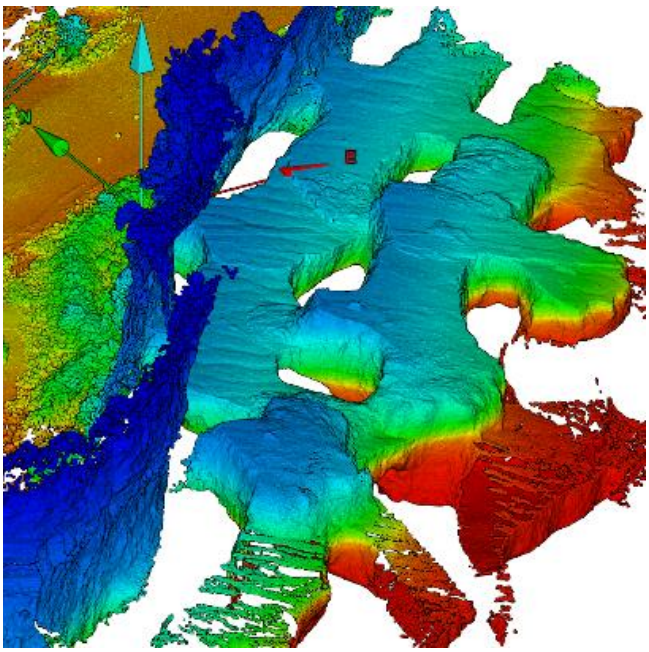

Figure 47 Drone LiDAR Point Cloud of Underground Workings at the Martinsburg, WV mine

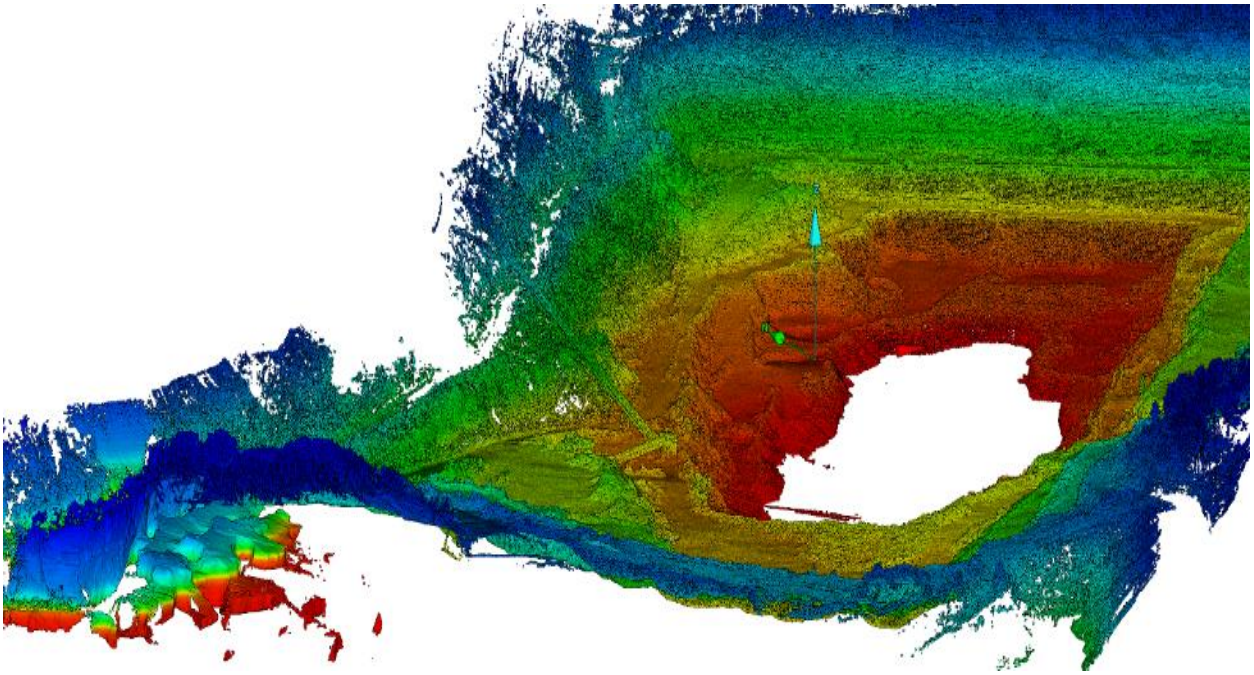

Figure 48 Drone LiDAR Point Cloud of Surface & Underground Workings in WV

4.3 Guidelines for Hazard Recognition

4.3.1 Post-processing & Geomechanical Analysis

To monitor underground stone mines' degradations in pillar and roof stability by using three-dimensional point cloud (3DPC) data gathered by LiDAR-equipped hand-held devices, drones, or ground-robots, it is aimed to accurately measure deviations from designed dimensions. The changes at different time intervals can be used as a means of strength degradation in geomechanical models or empirical equations using dimensions of pillars. This approach can lead to proactive control measures that may prevent catastrophic pillar or roof failures.

4.3.1.1 Pointcloud to mesh object

To perform this task, a perfectly shaped 3DPC of a cube is used initially. The simple flowchart of these computations is visualized in Figure 49. This method combines multiple software tools, including CloudCompare for manual manipulation and primary filtering, Python programming language for voxelization and noise reduction, Rhinoceros for the generation of surface mesh from 3DPC, and Griddle software for the generation of volumetric mesh. The generated volumetric mesh (e.g., grid file) is used for further analyses by using numerical simulations.

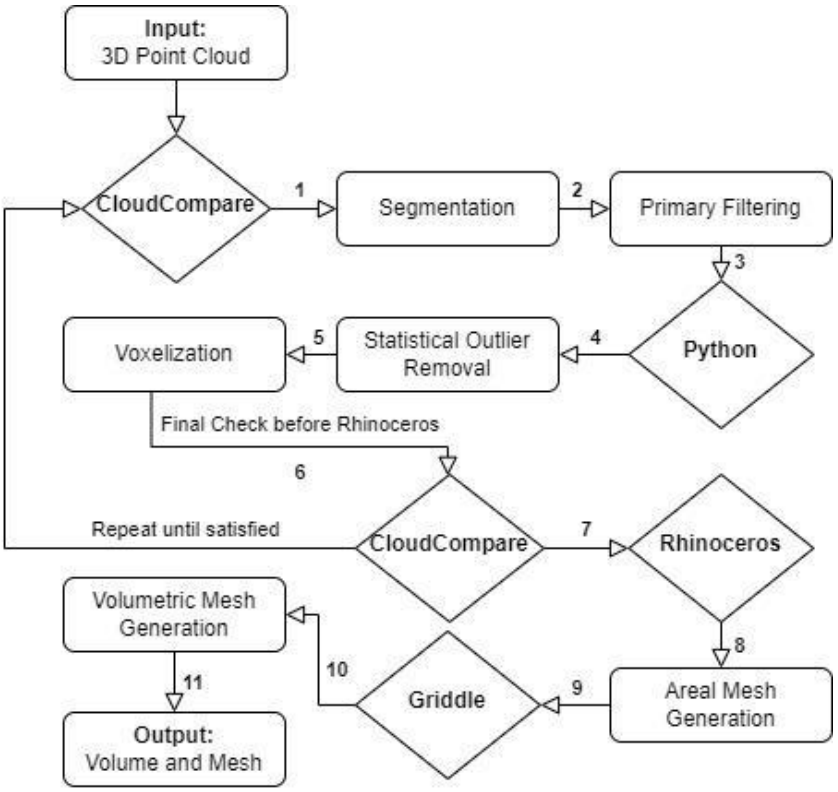

Figure 49 Mesh generation from 3DPCs

Figure 50 visualizes a 3DPC of a test cube generated to validate the above-outlined flowchart. The rough estimation of this 3DPC indicates that the volume is about 110,000-120,000 cubic-meters. It is not a certain measurement at this point since it is a sparse 3DPC with some noise and fluctuations. The 3DPC was processed for primary filtering, followed by statistical outlier removal with the nearest neighbors of 10. The voxel size is optimized to avoid losing any features (e.g., any surface from the cube) through a trial-and-error method. Therefore, it is imported into CloudCompare for a final check, which is performed to determine whether the 3DPC is ready for meshing or not. When it is ready, the 3DPC is exported for mesh generation in Rhinoceros. The surface mesh is generated via the command *MeshFromPoints*. Then, built-in volumetric mesh generator, Griddle, in Rhino is used to generate the volumetric mesh.

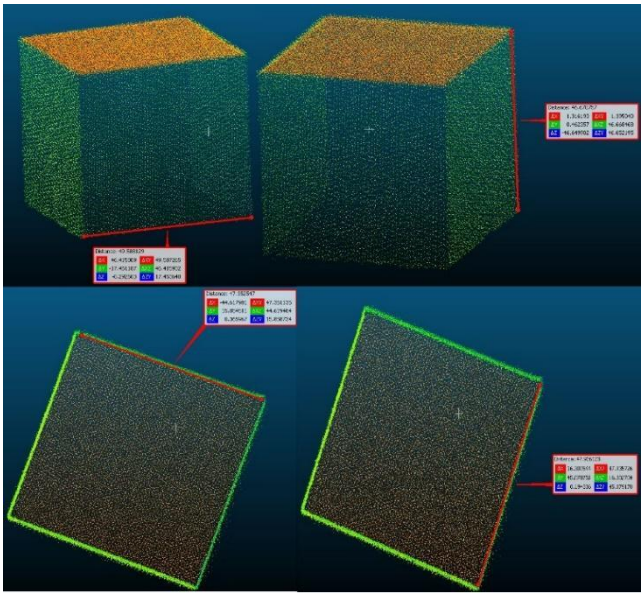

Figure 50 Dimensions of cubic 3DPC

The generated volumetric mesh is shown in Figure 51. The calculated volume for this mesh element is about 118,462 cubic-meters based on the zone elements.

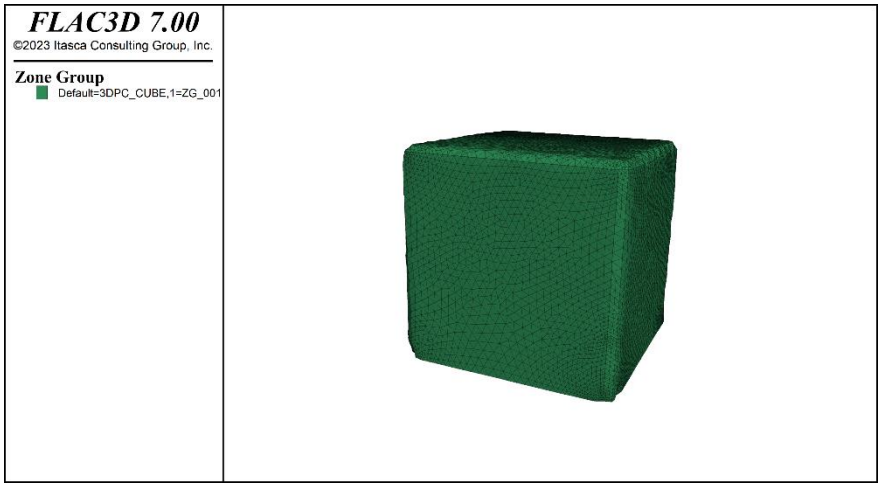

Figure 51 Generated mesh/volume from the cubic 3DPC

After verification of the methodology, the flowchart outlined in Figure 49 is applied to an individual underground stone mine pillar scanned obtained from a field visit. In this mine, multiple design layouts are employed but three of them govern the general layout. The pillar width and length are designed as 30 ft for square pillars, while lengths of 60 ft or 50 ft and widths of 25 ft or 30 ft are selected for rectangular pillars. Figure 52a shows the photo of the actual pillar in the underground mine, while Figure 52b represents the generated 3DPC of this pillar. The red circles in Figure 52a indicate the spalled material from the pillar ribs left as support to the pillars. Similar material is indicated in Figure 52b with blue circles, while the red line shows the path of the LiDAR scanner. This pillar is one of the square pillars, essentially having 30 ft width and length in design stages.

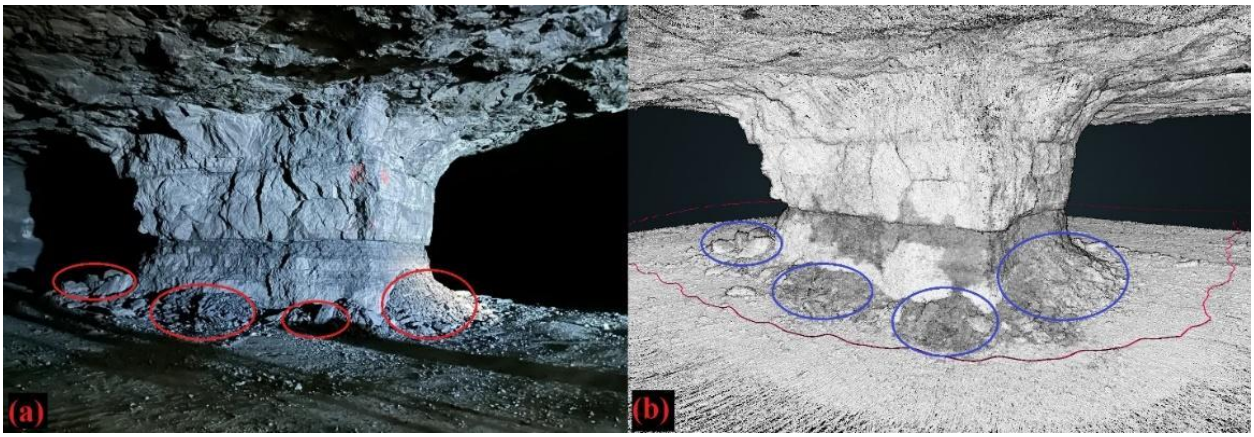

Figure 52 Underground stone mine pillar with spalled material indicated in circles: actual photo from mine (a), LiDAR scanned 3DPC (b)

To gather further information about the dimensions, the examined pillar is divided into four walls, and the point-to-point distances are computed via CloudCompare between north and south and east and west walls. Figure 53 visualizes each wall of the pillar. The mean distance between the north and south walls is computed as 24.5 ft with a 1.5 ft standard deviation, while the mean distance between east and west walls is found to be 27 ft with a standard deviation of 1.4 ft. Using the same logic, the mean height between roof and floor is calculated as 17.8 ft with a standard deviation of 0.7 ft. These measurements lead to the mean volume of this pillar being approximately 11,753 cubic feet, which deviates by 4,266 cubic feet from the designed pillar volume when the height is taken as 18 ft.

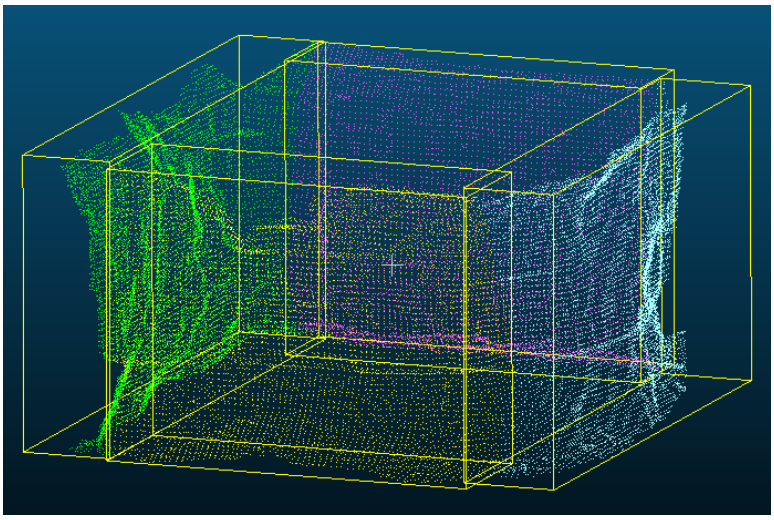

Figure 53 Pillar walls for distance calculation

The 3DPC presented in Figure 52b is then utilized to compute the volume of the pillar and generate the pillar's volumetric mesh. Steps 1 to 6 are performed on this 3DPC in an iterative manner to optimize the process. It should be noted that every single 3DPC is different; then, the optimization process (e.g., selection of number of neighbors, voxel size etc.) may vary. In the statistical outlier

removal process, 10 nearest neighbors are selected as the filtering group. During voxelization, the voxel length is employed as 0.2 ft. The voxelated and cleaned 3DPC is visualized in Figure 54.

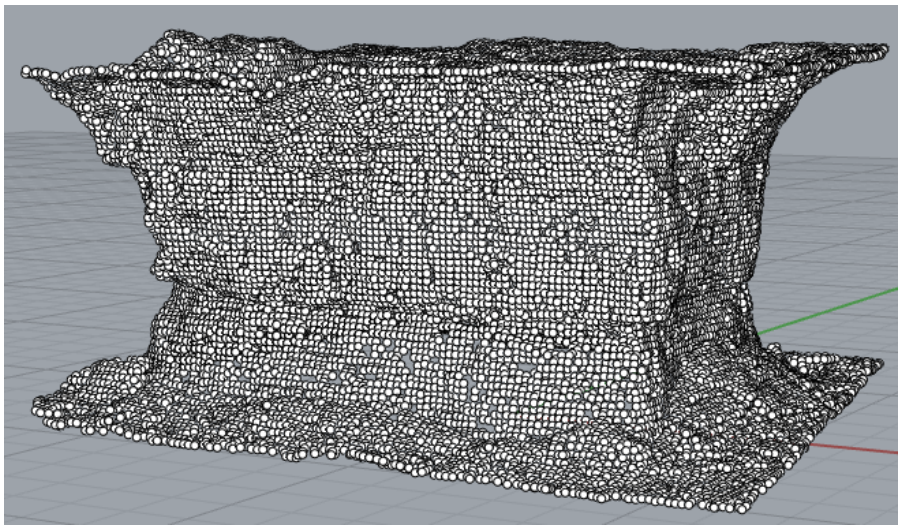

Figure 54 Voxelated and cleaned 3DPC in Rhinoceros

Therefore, a surface mesh is generated. However, due to non-conforming and irregular end of the mesh, it is not possible to produce a volumetric mesh. Then, two capping surfaces are introduced to trim the top and the bottom of the surface mesh. This provides smooth meshing without naked and non-manifold edges. The trimming edges and capping surfaces can be seen in Figure 55. After trimming, this mesh is used to generate the volumetric mesh. The volumetric mesh is exported as a FLAC3D (e.g., numerical simulation software) grid. This grid is presented in Figure 56, and the final volume is found to be 11,434 cubic-feet.

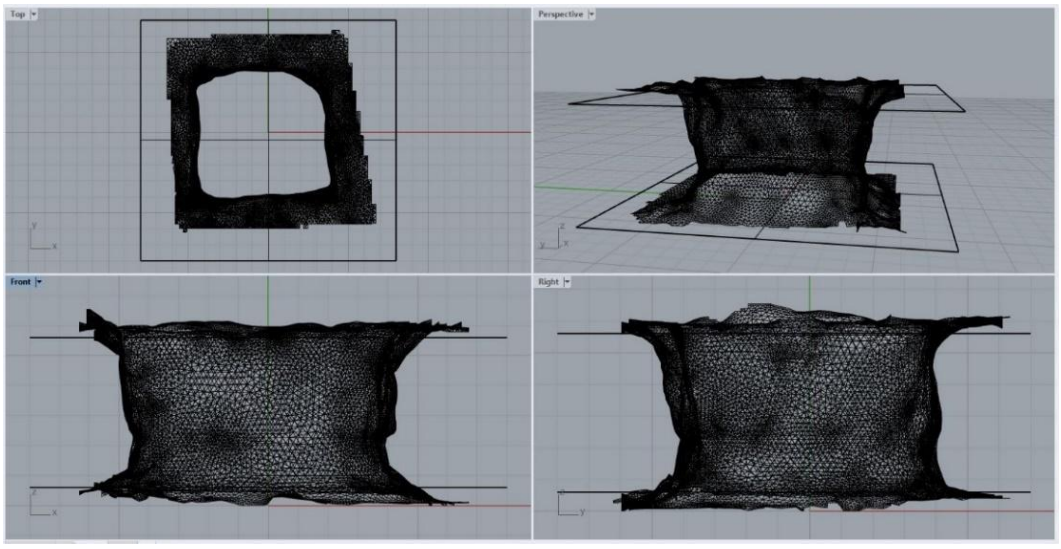

Figure 55 Generated mesh in Rhinoceros and the trimming surfaces

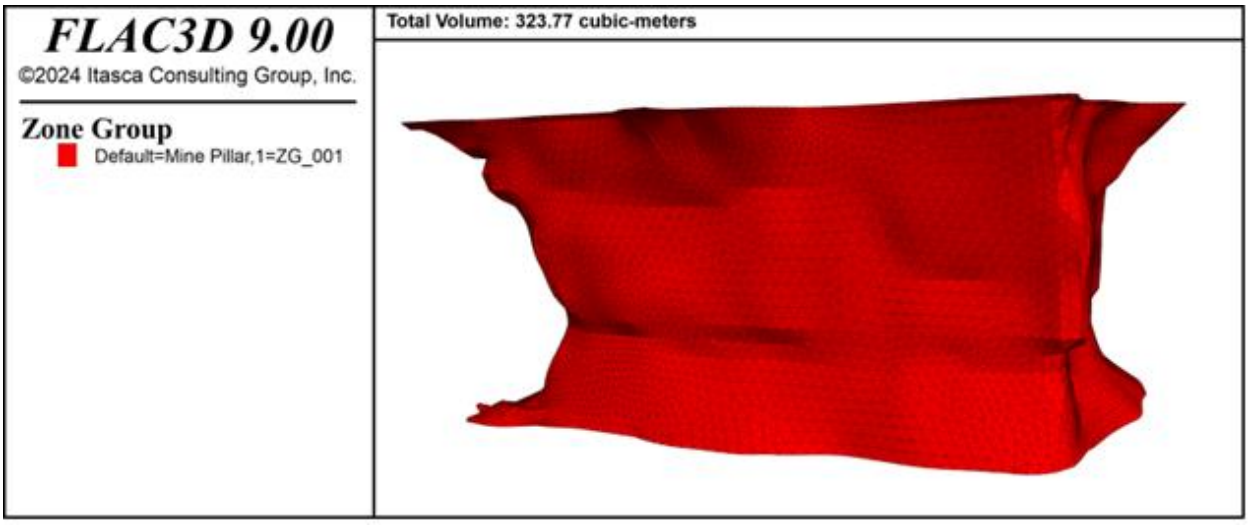

Figure 56 Generated volumetric mesh from the study pillar

The methodology outlined here discusses how three-dimensional point cloud data can effectively capture volumetric changes (from designed dimensions) in pillars, which are crucial for assessing geomechanical stability. The process involves multiple software tools for manual manipulation, filtering, voxelization, and meshing. The initial tests with a cubic 3DPC demonstrated the method's accuracy, and its application to actual mine pillar highlighted its practical utility. Accurate time-lapsed volumetric measurements would provide information about the condition of the underground mine pillars and roof while the generated mesh could be utilized for assessing the pillar strength and the potential failure mechanisms could expect for the underground mines.

4.3.1.2 FLAC3D model generation and analysis

Once imported to FLAC3D, the constitutive model can be implemented for strength analysis. The selected approach combines the elastic model with a strain-softening Mohr-Coulomb model, which allows the simulation of progressive degradation in rock strength parameters such as cohesion and friction angle as plastic deformation increases. This modeling method aligns well with the principles of Cohesion-Weakening Friction-Strengthening (CWFS) theory (Hajiabdolmajid et al., 2002; Rafiei Renani & Martin, 2018) which fits well to the behavior of stone pillars.

In the strain-softening Mohr-Coulomb model, rock initially behaves elastically, characterized by Young's modulus (E) and Poisson's ratio (v), which describe the stress-strain response before reaching yield conditions. These elastic parameters were selected based on typical values documented from extensive empirical studies conducted in underground stone mines (Esterhuizen et al., 2011). After surpassing the yield criteria, defined by the Mohr-Coulomb failure envelope, plastic deformation occurs, marking the transition from elastic to plastic behavior.

To effectively simulate brittle rock behavior, the CWFS logic is implemented, where the rock's cohesive strength decreases as plastic strain increases, reflecting the initiation and growth of micro-cracks that lead to damage and spalling. At the same time, frictional strength starts off minimal and gradually mobilizes and increases post-yielding as the fractured rock surfaces begin

to interlock under increasing confinement (see Figure 57). Thus, cohesion and friction angle become functions of accumulated plastic strain, aligning the numerical simulation with observed brittle rock behavior under low confinement.

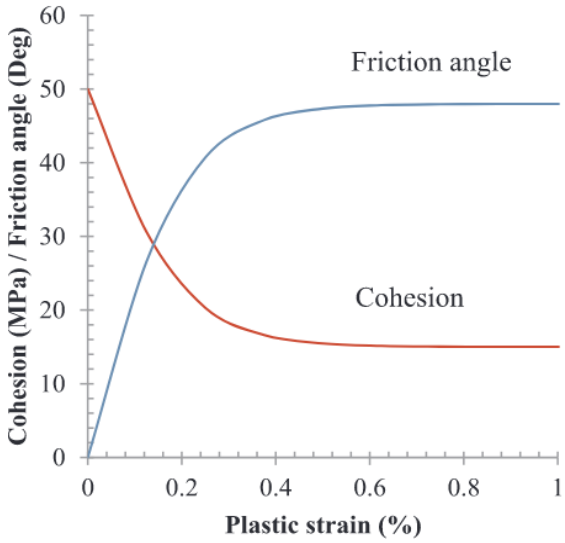

Figure 57 Evolution of Cohesion and Friction with Plastic Strain in the CWFS Model (Rafiei Renani & Martin, 2018)

In this case, the user can specify cohesion, friction, and dilatation as piecewise-linear functions of a hardening parameter that quantifies the plastic shear strain (Itasca Consulting Group, 2019). These functions were calculated with Equations (1) and (2). The degradation of cohesion (c) as a function of plastic strain (e^p) is given by:

$$c = c_r + (c_i - c_r)\left[2 - \frac{2}{1 + \exp\left(-5\frac{e^p}{e_r^p}\right)}\right] \quad (1)$$

Where c_i is the initial (peak) cohesion, c_r is the residual cohesion, and e_r^p is the plastic strain at which cohesion degradation is approximately 99% complete.
Simultaneously, the mobilization of the friction angle (ϕ) is described by:

$$\phi = \phi_i + (\phi_r - \phi_i)\left[\frac{2}{1 + \exp\left(-5\frac{e^p}{e_r^p}\right)} - 1\right] \quad (2)$$

Here, ϕ_i is the initial friction angle, ϕ_r is the residual (or fully mobilized) friction angle, and e_r^p is the residual plastic strain.

The described constitutive model approach, integrating elastic and strain-softening behavior under the CWFS logic, ensures a robust and realistic simulation of rock pillar behavior, accurately

reflecting the complex interaction between material properties, loading conditions, and failure mechanisms typical of underground stone mining environments.

The calibrated material properties for the case study rock mass are listed in Table 3. The details about the calibration process are presented by Jimenez (2023) and Jimenez (2025). Additional historical data analysis focused on intact rock characterization for stone mines is presented in the Appendix.

Table 3. Geomechanical Parameters after Calibration.

Material and Interface Properties	
Property	**Value**
Young's Modulus (GPa)	18.15
Poisson's Ratio	0.12
Tensile Strength (MPa)	-
Density (kg/m³)	2569
Intact Rock UCS (MPa)	103
Normal Stiffness (Pa/m)	8e+12
Shear Stiffness (Pa/m)	4e+12
Friction Angle (°)	20
Interface Cohesion (MPa)	0.5
Interface Tension (MPa)	0

Figure 58 shows the stress-strain curves resulting from numerical simulations for pillars with different w/h ratios. These curves indicate distinct strength characteristics for each ratio. The slender pillar (w/h = 0.5) exhibited the lowest peak strength and rapid post-peak strength reduction, confirming its susceptibility to brittle, sudden failure. In contrast, the squat pillar (w/h = 2.0) displayed significantly higher peak strength and more ductile behavior, consistent with the theory that higher confinement within the core increases resistance to failure.

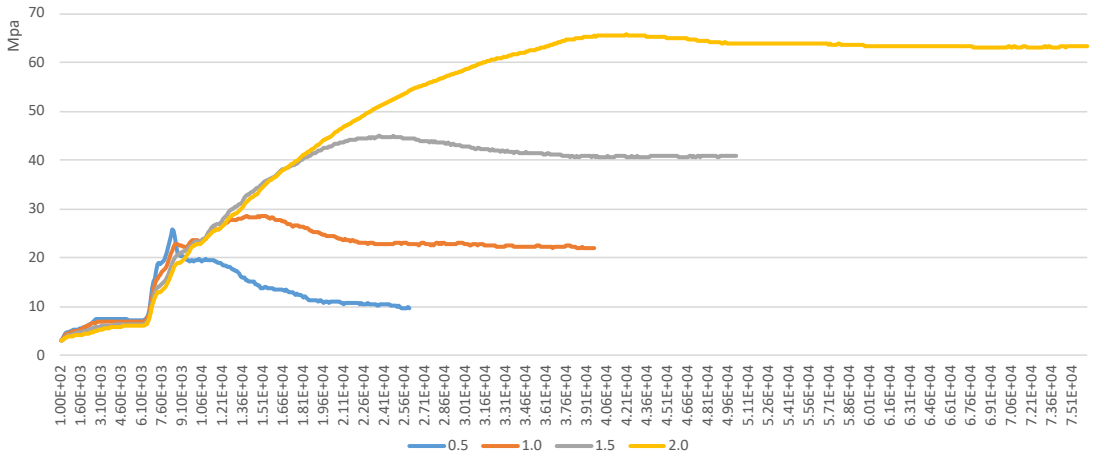

Figure 58. Stress Strain Curves for different w/h ratios

Validation against S-Pillar results (Figure 59) revealed good agreement, particularly for the w/h ratios between 1.0 and 1.5. At lower ratios (0.5), the FLAC3D results indicated a slightly lower

strength than predicted by S-Pillar, highlighting the limitations of empirical formulas at extreme slenderness. At higher ratios (2.0), FLAC3D indicated greater strength and confinement benefits than captured by S-Pillar, demonstrating the numerical model's advantage in capturing complex confinement effects.

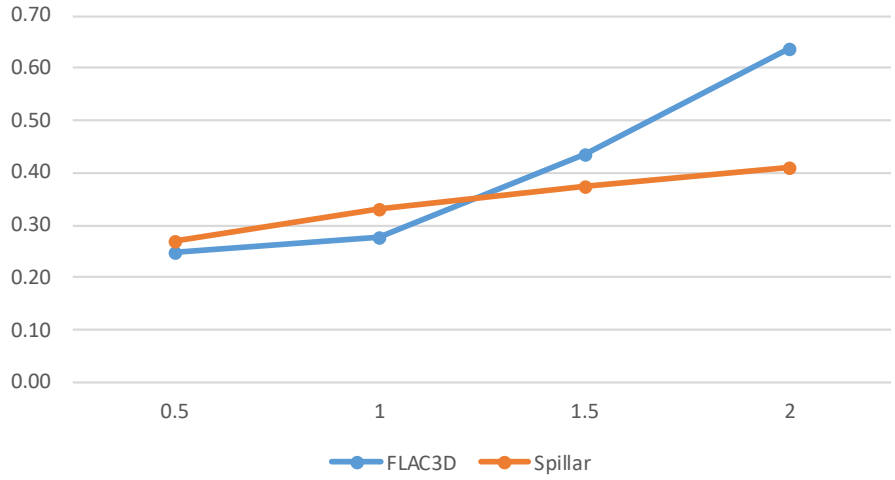

Figure 59. Comparison of Pillar Strength Ratio from FLAC3D and S-Pillar Software for different pillar w:h ratios.

The effect of pillar length is also examined and the results confirmed that increased pillar length improves strength, but the degree of improvement is strongly dependent on the pillar's width-to-height ratio. Each case was normalized against its corresponding strength at l/w = 1.0 to measure the relative strength increase due to elongation. The results are shown in Figure 60, where the strength ratio (strength at a specific l/w divided by the strength at l/w = 1.0) is plotted for each w/h category.

- For w/h = 0.5, the strength ratio remains nearly constant across all l/w values. This suggests that slender pillars, lacking a confined core, do not significantly benefit from elongation. Their failure is dominated by unconfined sidewall spalling and brittle fracture, which remain relatively unaffected by length.

- For w/h = 1.0, moderate increases in strength are observed, particularly as l/w exceeds 2.0. This indicates the early formation of a confined core and suggests that length begins to play a role in stabilizing post-failure load redistribution.

- For w/h = 1.5 and 2.0, the effect of length is profound. The strength ratio for the w/h = 2.0 pillar increases from 1.0 to over 1.65 as l/w grows from 1.0 to 4.0. This nonlinear growth highlights the critical role of geometry in enhancing confinement. Longer pillars allow for a more extensive development of a highly confined inner core, which improves the frictional resistance mobilized in the post-peak regime under the CWFS framework.

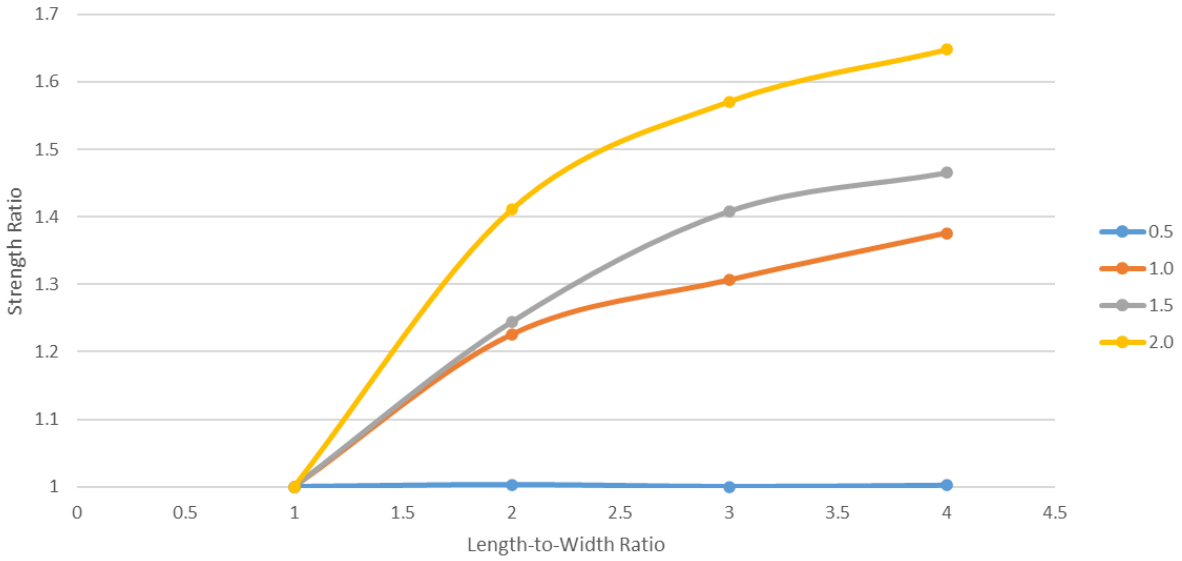

Figure 60. Strength ratio (normalized to l/w = 1.0) as a function of length-to-width (l/w) ratio for various width-to-height (w/h) values

This model is applied to the case study pillar and the failure pattern in Figure 61 is observed with failure starting along the edges and mostly staying near the perimeter. While there is some inward propagation observed, it remains less advanced due to the pillar having high w:h ratio and having a larger confined core compared to some of the other pillars analyzed. The presence and depth of spalling plays a significant role in governing how far failure extends into the pillar and whether the remaining structure retains integrity or undergoes complete collapse. The analyzed pillar at its current dimensions were found to be stable as expected, even under much higher loads.

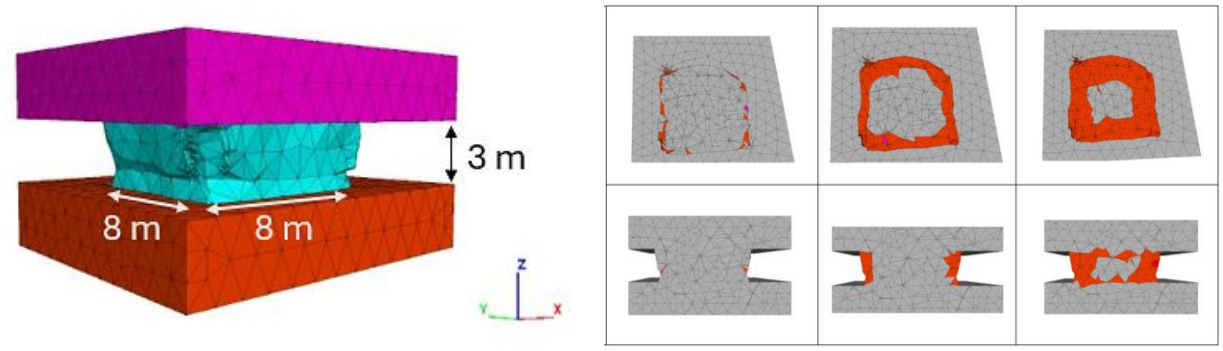

Figure 61. Sequence of horizontal (top row) and vertical (bottom row) cross-sections showing failure propagation in as-mined pillar for the case study pillar mine.

4.3.1.3 Rock mass characterization

The assessment of rock mass characteristics was achieved with the use of the Discontinuity Set Extractor (DSE) software to analyze joint orientations, spacing, and dip angles within high-resolution pillar scans. Among the eight available pillar scans, the dataset with the highest resolution was selected for detailed analysis. The discontinuity results obtained from DSE for the

other scans are presented in Elibol et al. (2024). The methodology for rock mass characterization involved drawing four imaginary lines on the pillar surface to systematically identify joint locations, spacing, dip, and dip direction. The structural characteristics extracted through DSE were essential for geomechanical classification.

The identification of joint sets within the selected pillar was conducted using DSE. Four imaginary lines were drawn on the pillar surface to systematically locate joints and discontinuities (Figure 62). The analysis focused on identifying joint parameters, including joint location, spacing, and dip and dip direction, which were measured using stereo nets. These structural characteristics are critical for assessing the effect of large and persistent discontinuities.

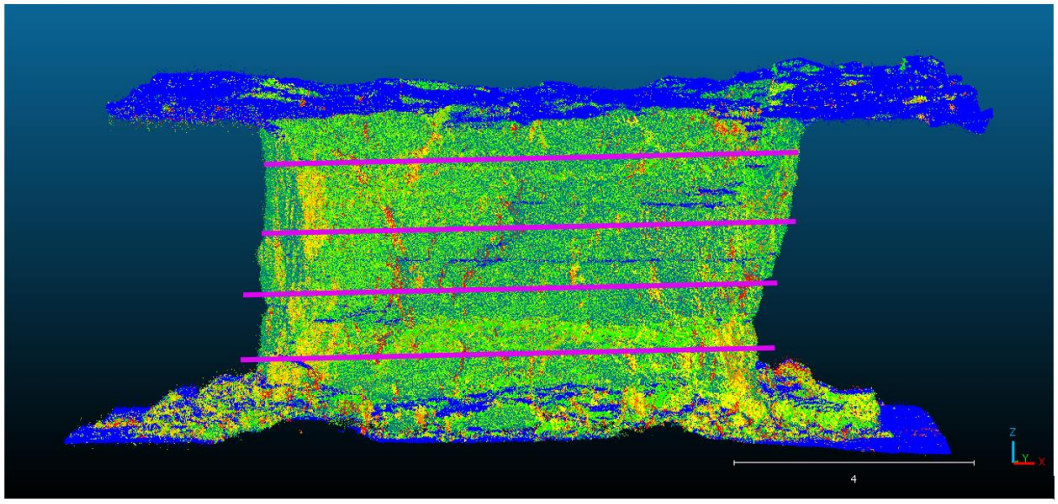

Figure 62 Pillar surface scan after DSE with four lines

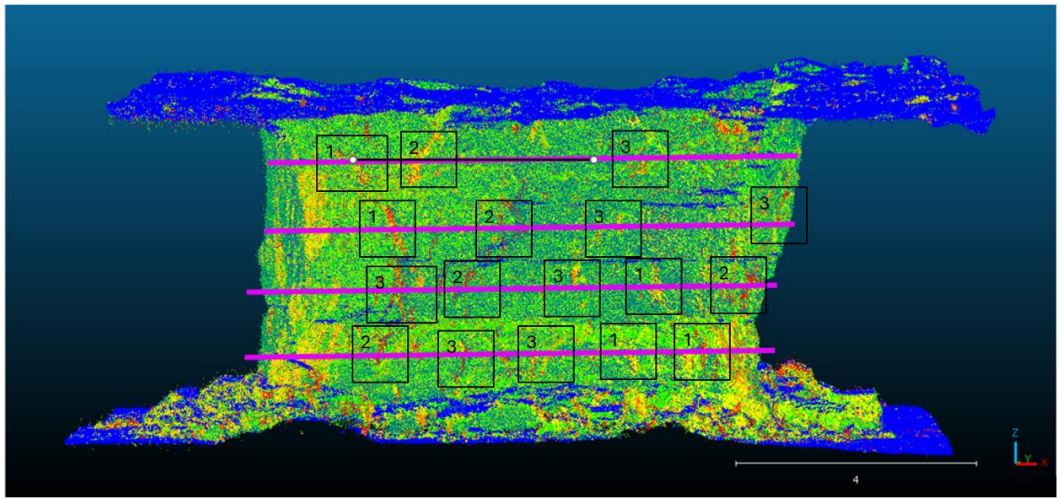

Figure 63 Identified joint sets on the lines and their classification

The analyzed pillar's surface has an E-W strike with a 90° dip angle. According to DSE Software analysis, the joints are separated into three classes according to their strike and dip (Figure 63). The strike and dip angles are given below in Table 4 according to joint classification. This information can be implemented into the Rock Mass Rating for the discontinuity spacing rating.

In this case, the average spacing considering all four lines were estimated as 1.85 meters which result in a spacing rating of 17.5 for RMR.

Table 4 Joint classification according to strike dip direction and dip angle

Joint Types	Strike, dip direction & dip angle
Joint 1	N56°W/ 15 SW
Joint 2	N2°W/72 NE
Joint 3	N35°E/4 NW

4.3.1.4 Mine map re-analysis

Another important piece of information that can be obtained from the scans is the change in pillar dimensions due to spalling. This information is useful in two ways: 1) determining the new pillar dimensions to update strength estimation calculations, and 2) detect changes between consecutive scans to identify stress concentrations and hazards. Raw LIDAR scan data is typically stored in point cloud formats, such as .LAZ, E57, and PTS, which are not directly compatible with AutoCAD. To address this limitation, AutoCAD ReCap Pro, a specialized software designed for point cloud processing, was employed. The LIDAR scan files were initially stored in .LAZ format was imported into AutoCAD ReCap Pro, where they were processed and converted into an AutoCAD-compatible format (.RCP - ReCap Project). This conversion enabled seamless integration with AutoCAD, allowing for the overlaying of 2D mine maps onto the 3D LIDAR model. This process facilitated a direct visual assessment of pillar dimensions and allowed for an effective comparison between the planned mine layout and actual conditions (Olivier, 2023).

After converting the point cloud data, the next step was to align it with the existing 2D mine map from AutoCAD. Since the 2D mine map does not inherently contain depth information, both datasets were converted into 3D visualization mode in AutoCAD. The alignment process involved: (a) Rotating and scaling to be able to overlay mine map and point cloud correctly, (b) adjusting Coordinate Systems to match reference points in both datasets, and (c) final verification to compare pillar positions in both datasets.

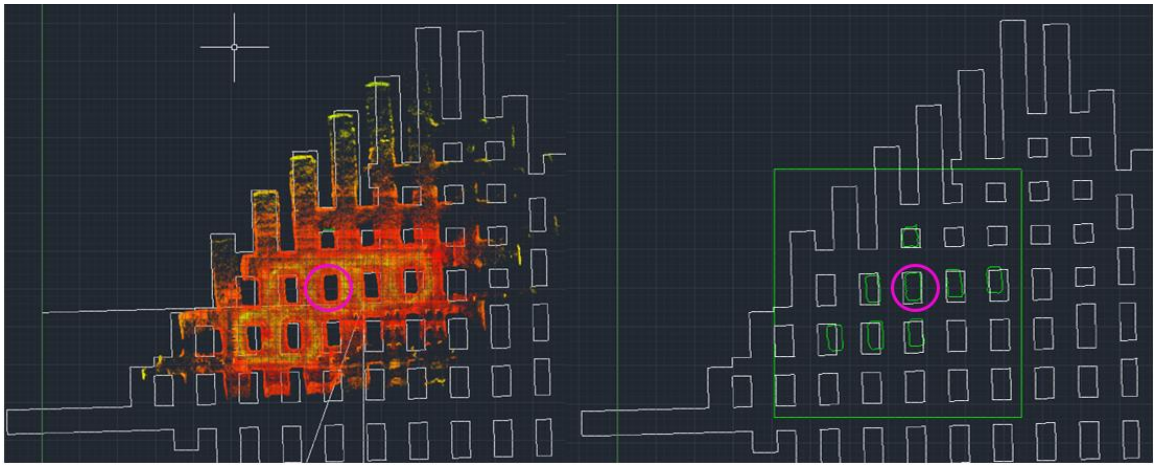

Figure 64 Left) The LIDAR scan is overlaid and aligned on top of the mine map layout. Right) Map layout pillars and pillars scanned from LIDAR

Among the eight pillars scanned, the pillar with the highest resolution was selected for detailed discontinuity analysis. Using CloudCompare, the raw point cloud was pre-processed to enhance visualization and extract structural features.

Pillar widths extracted from the AutoCAD mine map were compared against those measured from the LIDAR scans to assess changes in pillar geometry over time (Table 5). Variations in pillar width have a direct impact on stability and load-bearing capacity. This comparison was conducted using AutoCAD's measurement tools, allowing for the extraction and documentation of pillar width dimensions from both the mapped design and LIDAR scan measurements. The observed changes in pillar geometry were then evaluated for their potential effects on pillar strength.

Table 5 Designed pillars vs LIDAR scanned pillar measurements obtained in AutoCAD

	Designed	LIDAR	Change
Area of the designed pillar (ft^2)	1500.00	921.12	-38.61%
Width of the designed pillar (ft)	30	21.69	-27.7%
Length of the designed pillar	50	44.15	-11.71%

Figure 65 Selected pillar map design and LIDAR scan comparison

Tests were conducted to detect change using two different LIDAR scans taken of the same pillar at different times. LIDAR scans were collected nine-months apart. A pillar with high-definition point clouds from both visits were selected to test the algorithms (Figure 66).

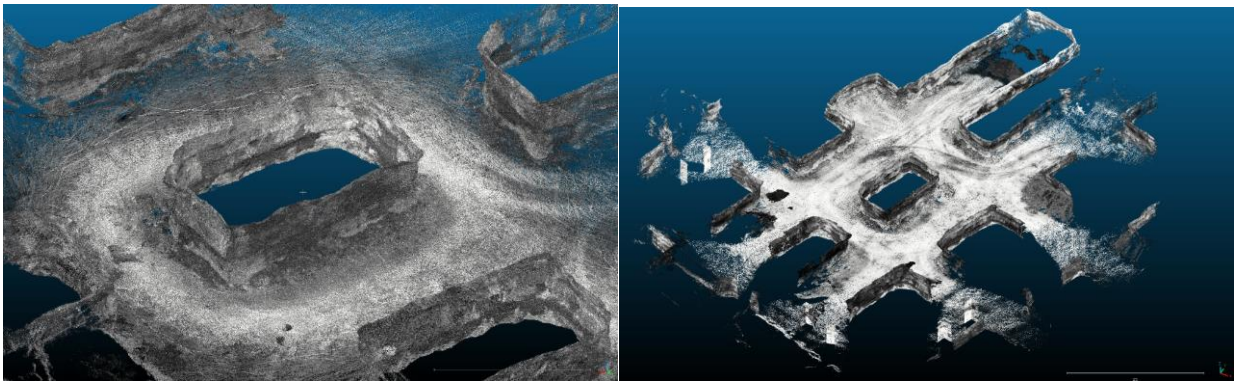

Figure 66 Pillar scans from two different visits

CloudCompare software was used to clean and reposition/scale the point clouds to manually match as closely as possible. The next step was to register the two point clouds and align both entities. For a more precise registration, all four ribs of the pillars were registered separately. However the registered scans were not to scale and a final adjustment to resize the scans was necessary. It was observed that there has been spalling on the pillar ribs and it was also seen in the point cloud comparison (Figure 67). The main contributing factor for the spalling was observed as the shale bands running horizontally in the middle of the pillars. The mine has started pushing clay toward the ribs of the pillars, covering the shale band, to contain the spalling and degradation of the shale bands.

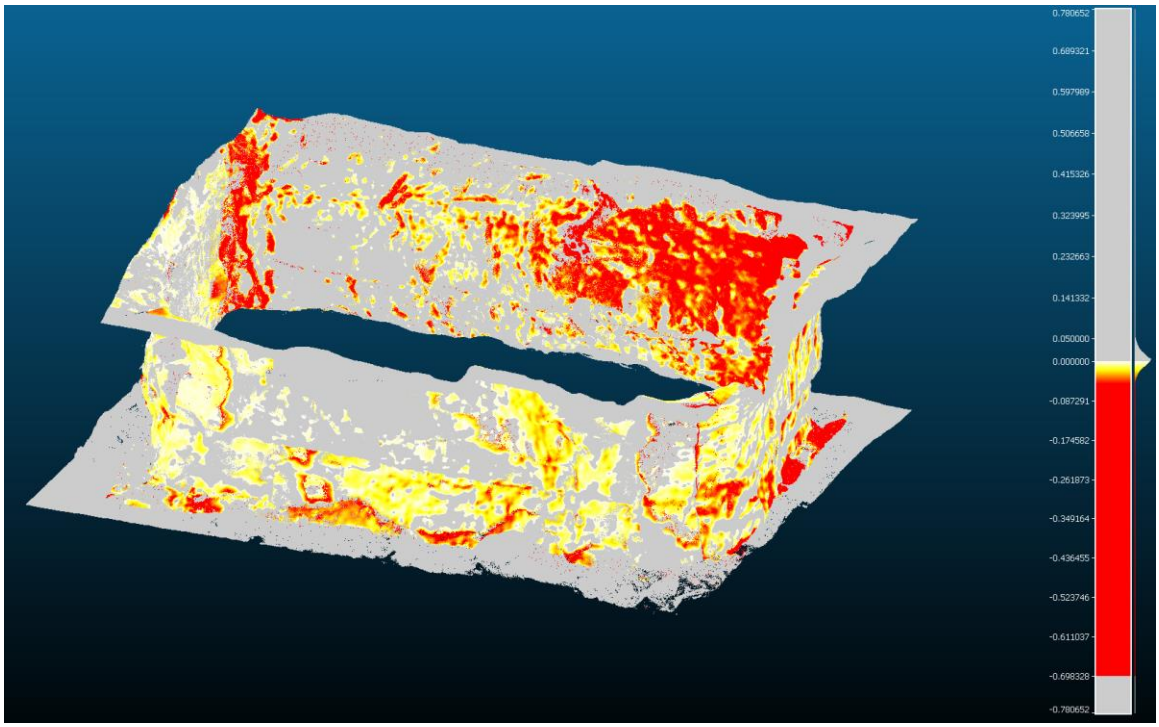

Figure 67 Change detection from two LIDAR scans 9-months apart.

4.3.2 S-Pillar, LaModel, and Stability Mapping integration

The pillar shown in Figure 65 and Figure 66 was selected to demonstrate the pillar stability analysis application. The selected case study pillar had the following dimensions and properties:

- Pillar width (rectangular): 30 ft (9.14 m)
- Pillar length (rectangular): 50 ft (15.24 m)
- Pillar height: 22.96 ft (7 m)
- UCS: 181.9 Mpa

Strength calculations were performed using the empirical method developed by Esterhuizen et al. (2011), implemented within the S-Pillar software, which provides a practical and widely applied

empirical tool for underground stone mine design. According to this method, the calculated pillar strength for the case study pillar was determined as 56.47 MPa, where the S-Pillar method assumes simplified loading conditions and uniform material properties.

A mathematical model of rock pillar failure in brittle rock found that thinner pillars gain less from increased length than thicker pillars due to being unconfined. The model demonstrates that the Length Benefit Ratio (LBR) is 0 when the ratio of width to height is 0.5, but increases to 1.0 as the ratio approaches 1.4, as shown in Table 6. The method calculates the length benefit in terms of an equivalent pillar width increase used in the equation for pillar strength. The calculation of the equivalent width follows Wagner's formula (1992), presented in Equation 3, which incorporates parameters such as the pillar's actual width, plan area, circumference, and the LBR value.

$$w_e = w + \left(\frac{4A}{C} - w\right) * LBR \quad (3)$$

Where A is the area of the pillar, C is the circumference of the pillar, w is the width of the pillar, and LBR is the length benefit ratio calculated according to Table 6. For square pillars, the equivalent width is simply the actual width. A chart of LBRs for different ratios of width to height is available, illustrating that as the ratio increases, the LBR approaches 1.0. This implies that rectangular pillars benefit proportionally more from length when they are wider, as shown in Table 6.

Table 6 Length Benefit Ratio (LBR) values calculated for corresponding width-to-height ratios (Esterhuizen et al, 2011)

Width-to-height ratio	Length benefit ratio (LBR)
0.5	0.00
0.6	0.06
0.7	0.22
0.8	0.50
0.9	0.76
1.0	0.89
1.1	0.96
1.2	0.98
1.3	0.99
1.4	1.00

In our case w_e is calculated as 9.28 m for mine map design layout and 6.75 m for the LIDAR scanned width. The research indicates that rectangular pillars increase pillar strength, as researched by numerous studies (Wagner, 1992; Mark and Chase, 1997; Galvin et al., 1999; Dolinar and Esterhuizen, 2007). These pillars are also less affected by geological structures when their longer axis is properly aligned, making them a more stable option (Dolinar and Esterhuizen, 2007). However, there remains a research gap regarding the performance of inclined rectangular pillars, highlighting an area for further investigation.

In conclusion, two different sets of pillar width and length measurements were analyzed: one obtained from a mine map layout and the other from a LIDAR scan. The pillar dimensions from the mine layout were recorded as 9.14 m (30 ft) and adjusted width as 9.28 m (30.44 ft) and 15.24

m (50 ft) in length. For the LIDAR scan measurements, the width was measured as 6.61 m (21.69 ft), where the adjusted width is calculated as 6.75 m (22.14 ft). To determine the pillar strength, the large discontinuity factor (LDF) was required. The LDF is calculated using Equation 4;

$$LDF = (1 - DDF) * FF \quad (4)$$

Where DDF is the discontinuity dip factor, and FF is the frequency factor related to the frequency of large discontinuities per pillar. These two parameters are calculated using Table 7 and Table 8

Table 7. Discontinuity Dip Factor (DDF) Table (Esterhuizen et al, 2011)

Discontinuity dip (deg)	**Pillar width-to-height ratio**								
	≤0.5	**0.6**	**0.7**	**0.8**	**0.9**	**1**	**1.1**	**1.2**	**>1.2**
30	0.15	0.15	0.15	0.15	0.16	0.16	0.16	0.16	0.16
40	0.23	0.26	0.27	0.27	0.25	0.24	0.23	0.23	0.22
50	0.61	0.65	0.61	0.53	0.44	0.37	0.33	0.3	0.28
60	0.94	0.86	0.72	0.56	0.43	0.34	0.29	0.26	0.24
70	0.83	0.68	0.52	0.39	0.3	0.24	0.21	0.2	0.18
80	0.53	0.41	0.31	0.25	0.2	0.18	0.17	0.16	0.16
90	0.31	0.25	0.21	0.18	0.17	0.16	0.16	0.15	0.15

Table 8. Frequency Factor (FF) Table (Esterhuizen et al, 2011)

Average frequency of large discontinuities per pillar	**Frequency Factor**
0.0	0.00
0.1	0.10
0.2	0.18
0.3	0.26
0.5	0.39
1.0	0.63
2.0	0.86
3.0	0.95
>3.0	1.00

The DDF was specifically calculated using LIDAR scan data analyzed with DSE software, which identified the LDF for the mine was determined to be 0.77. And the LIDAR-scanned pillar had dimensions of 6.61 m (21.69 ft) in width and 13.45 m (44.15 ft) in length. To analyze the worst-case scenario with greater accuracy in real-life applications, LDF is considered with a value of 0.77.

Table 9 Pillar strength values for adjusted widths for the mapped pillar and the LIDAR scanned pillar with adjustment.

S-Pillar strength equation	$\sigma_p = 0.65 * \sigma_0 * LDF * \frac{{w_e}^{0.3}}{h^{0.59}}$

Pillar Strength Value with Mine Map	56.47 MPa
Pillar Strength Value with LIDAR Scan	51.36 MPa

The pillar strength values as presented in Table 9 were 56.47 MPa for the designed pillar and 51.36 MPa for the LIDAR-scanned pillar. The corresponding width reduction was approximately 1.53 %, resulting in a 9.9% decrease in strength, indicating how even modest changes in geometry and discontinuities can significantly affect pillar strength. Overall, the analysis demonstrates that LIDAR scanning is a valuable tool for capturing true pillar geometries and estimating pillar strength more accurately, while also emphasizing the importance of accounting for width adjustments and zone-specific conditions, especially in benched areas.

A model is also generated using the LaModel Stability Mapping extension (Figure 68). To expand LaModel's applicability to stone mining, Escobar (2021) integrated the empirical stone pillar strength equation developed by Esterhuizen et al. (2011) (Eq. 5), which was previously implemented in the S-Pillar software. This integration enabled LaModel to conduct stress and safety factor analyses for stone mines, even in settings with irregular pillar geometries and undulating overburden. Please note that the 0.65 coefficient corresponds to metric units (m and MPa). For English units (ft and psi), the coefficient is 0.92.

$$\sigma_p = 0.65UCS\frac{w^{0.3}}{h^{0.59}} = \sigma_o\frac{w^{0.3}}{h^{0.59}} \tag{5}$$

Escobar (2021) applied gradient-based equations (Eq. 6 and 7) to simulate the internal strength distribution across the pillar that would match the pillar strength calculated using Eq. 1. The parameters include the σ_0 (rock strength), h (height of the pillar), W (element width), and x, which is the average location of the element within the pillar. Gradient equations for stone mine pillars were developed using methodologies similar to those outlined by Mark et al. (1992) and Johnson et al. (2014). These approaches consider the strength variation from the rib of the pillar within. These equations define the strength variation depending on the distance from the pillar rib. These equations enhance LaModel's ability to simulate confinement that develops in a pillar's core.

$$\sigma_{corner} = \left(\frac{1.23*\sigma_0}{h^{0.59}W^2}\right)\left[\left(x+\frac{W}{2}\right)^{2.3} - 2.3\left(x+\frac{W}{2}\right)\left(x-\frac{W}{2}\right)^{1.3} + 1.3\left(x-\frac{W}{2}\right)^{2.3}\right] \tag{6}$$

$$\sigma_{rib}(x) = 1.84\sigma_0\frac{x^{0.3}}{h^{0.59}} \tag{7}$$

In summary, Escobar (2021) extended LaModel's utility to stone mining by integrating empirical strength equations for stone pillars and by using gradient functions to better represent the pillar strength. This approach enhances predictive capability without modifying material strength spatially within the pillar. The users may modify in-seam material properties using Eq. 6 and 7, which depend on the relative positions of pillar elements and their sizes.

The element size for the case study pillar was determined as 1 ft to be able to capture more detail. One pillar is generated according to mine design layout, and another pillar is generated according to LIDAR scans, where 5 elements have been reduced from the width and 9 elements reduced from the length.

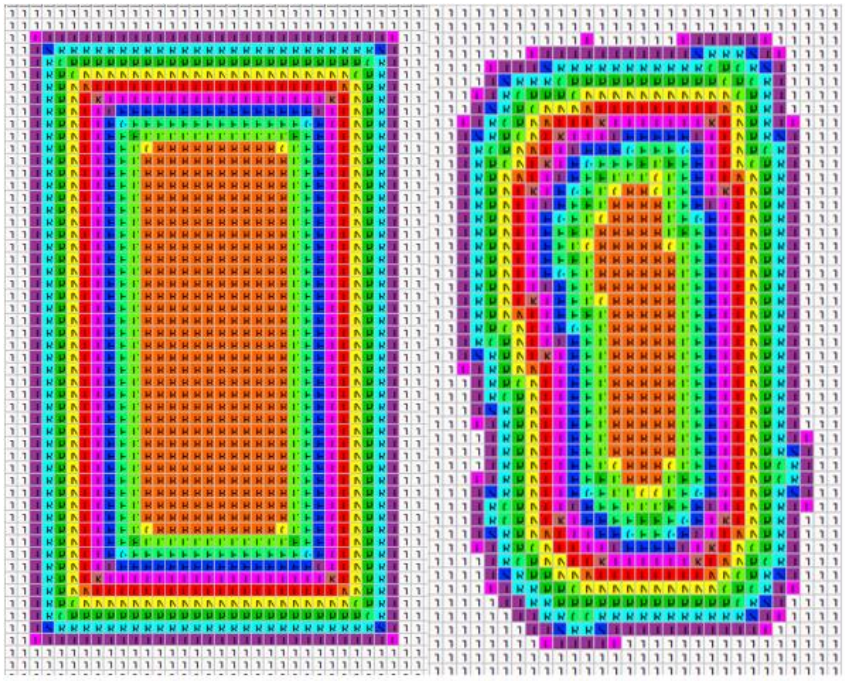

Figure 68 LaModel pillar's grid comparison. Left) Designed. Right) LIDAR scanned

In our case, the w-h ratio is almost 1.3, and some discontinuities have almost 70 dip angles. According to the LaModel results, the calculated pillar strength is 59.68 MPa for the designed pillar and 58.03 MPa for the LIDAR-scanned pillar. This reflects a reduction of approximately 2.75% in pillar strength due to the observed dimensional changes. Although the percentage decrease may seem modest, it highlights the sensitivity of pillar strength to geometric variations, especially in the presence of high-angle discontinuities. In critical areas of the mine where ground conditions are less favorable, even small reductions in strength could impact long-term stability and safety.

According to the S-Pillar analysis, the estimated pillar strength is 56.47 MPa for the designed pillar and 51.36 MPa for the LIDAR-scanned pillar, indicating a 9.05% reduction in strength due to dimensional changes observed in the scan. In contrast, LaModel results show a pillar strength of 59.68 MPa for the designed pillar and 58.03 MPa for the LIDAR-scanned pillar, reflecting a smaller reduction of approximately 2.75%.

This discrepancy highlights how different modeling approaches respond to changes in geometry. S-Pillar, being an empirical tool, may be more sensitive to width and height changes, particularly under assumptions of uniform loading and simplified geometry. LaModel, on the other hand, incorporates stress distribution and load transfer across the seam, providing a more nuanced response to dimensional changes, especially when confinement and boundary effects are present. Overall, both tools indicate a loss in pillar strength due to narrowing, but the magnitude of the reduction differs. This suggests that relying solely on empirical methods may overestimate the impact of dimensional changes in certain geomechanical settings. Using a combination of empirical and numerical approaches provides a more comprehensive understanding of pillar stability.

5. Publication Record and Dissemination Efforts

Publications:

Akhihiero, D., & Gross, J. N. (2025, April). A Pointcloud Registration Framework for Relocalization in Subterranean Environments. In 2025 IEEE/ION Position, Location and Navigation Symposium (PLANS) (pp. 1257-1264). IEEE.

Arend Tatsch, C. A. (2024). Enhancing Robotic Exploration through Semantically-Guided Sampling Strategies. WVU Ph.D. Dissertation.

Escobar, L., & Pereira, G. A. (2025, May). Energy-Aware Coverage Path Planner for Multirotor UAVS. In 2025 International Conference on Unmanned Aircraft Systems (ICUAS) (pp. 777-784). IEEE.

Jimenez, R, "Analysis of the Brittle Failure Mechanism of Underground Stone Mine Pillars by Implementing Numerical Modeling in FLAC3D", (2023), MS Thesis, West Virginia University.

Jimenez, Y, "Investigation Of Spalling Effects on The Brittle Behavior of Rectangular Pillars in Underground Stone Mines.", (2025), MS Thesis, West Virginia University.

Lima, R. R., & Pereira, G. A. (2025). Tension-Aware Motion Planning for Tethered Robots. Robotics, 14(2), 11.

Lima, R. R., Rocamora, B. M., & Pereira, G. A. (2023). Continuous vector fields for precise cable-guided landing of tethered uavs. IEEE Robotics and Automation Letters, 8(7), 4370-4377.

Lima, R. R., & Pereira, G. A. (2023). A multi-model framework for tether-based drone localization. Journal of Intelligent & Robotic Systems, 108(2), 20.

Reed, C., Tatsch, C., Gross, J. N., & Gu, Y. (2025, October). Autonomous Hiking Trail Navigation via Semantic Segmentation and Geometric Analysis. In 2025 IEEE/RSJ International Conference on Intelligent Robots and Systems (IROS) (pp. 52-58). IEEE.

Suner, M.C., A. Elibol, R. Jimenez, D. Tuncay, and Z. Agioutantis, (2024), Calibration of LaModel In-Seam Material Properties for Underground Stone Mine Benching Operation by Employing Brittle Failure Criteria in FLAC3D, Proceedings, 43rd International Conference on Ground Control in Mining, July 22-25, Canonsburg, PA.

Tatsch, C., Bredu, J. A., Covell, D., Tulu, I. B., & Gu, Y. (2023, June). Rhino: An autonomous robot for mapping underground mine environments. In 2023 IEEE/ASME International Conference on Advanced Intelligent Mechatronics (AIM) (pp. 1166-1173). IEEE.

Presentations and Interviews:

Bishop, R. (2023). Society for Mining, Metallurgy, & Exploration: "Flying Drones in the Mining Industry", June 29, 2023. https://www.youtube.com/watch?v=HG_TRNfAycY

Bishop, R. (2023). American Geosciences Institute's Earth Science Week Drone Webinar: "Drones for Earth Science". October 10, 2023. https://youtu.be/jtjP4EsXzDA

Bishop, R. (2023). Maptek Newsletter by Marisa Suarez: "How can mining operations increase safety underground?", March 30, 2023. https://www.maptek.com/blogs/how-can-mining-operations-increase-safety-underground/

Bishop, R. (2024): "Autonomous Drones for 3D Mapping of Underground Mines", presented twice at the Virginia Tech Engineering Open House event, Blacksburg, VA. April 15, 2024.

Bishop, R. (2024): "Drones for Underground Mines", presented at the 2024 Kids' Tech University Outreach Program, Virginia Tech, Blacksburg, VA. March 16, 2024.

Bishop, R. (2023): "UAV Systems for Room & Pillar Mine Digitization Beyond Visual Line of Sight", presented at the Kentucky Crushed Stone Association's Underground Stone Safety Seminar, Louisville, KY. December 6, 2023.

Bishop, R. (2024): "Drones in Underground Mines", presented to Virginia Tech's Mine Automation & Data Analytics course, Blacksburg, Virginia. November 6, 2024.

Bishop, R. (2024): "Drone-based Surveying in Mining", presented to West Virginia University's Mine Surveying course. Morgantown, WV. November 4, 2024.

Bishop, R. (2024): "Drones in Mining", presented to Virginia Tech's Space Mining course. Blacksburg, VA. October 25, 2024.

Bishop, R. (2024): "Drones in Mining", presented to Virginia Tech's ENGR 1014 course. Blacksburg, VA. October 25, 2024.

Bishop, R. (2024): "Drones for Underground Mines", presented at Virginia State University's STEAM-H Seminar, Petersburg, Virginia. September 27, 2024.

Bishop, R. (2024): "Drone-based Surveying in Mining", presented to Virginia Tech's Mine Surveying & Mapping course. Blacksburg, VA. September 3, 2024.

Pereira, G. A. S. (2024): "Improving Mining Safety with Autonomous Drones", keynote presentation at the IEEE Latin-American Robotics Symposium, Arequipa, Peru, November 12, 2024

Bishop, R. (2025): "Drones for Underground Mines", presented to the Engineering 1004 course, Virginia Tech, Blacksburg, VA. February 17, 2025.

Bishop, R. (2025): "Autonomous Drones for Underground Mines", presented at the Virginia Tech College of Engineering Open House, Virginia Tech, Blacksburg, VA. March 31, 2025.

Bishop, R. (2025): "Autonomous Drones for Underground Mines", presented to Oak Grove, Alabama, May 15, 2025.

Bishop, R. (2025): "Mining Drone Research in Mining & Minerals Engineering at Virginia Tech", presented to Caterpillar, Blacksburg, VA. September 5, 2025.

6. Conclusions and Impact Assessment

This project demonstrated the feasibility and value of using autonomous robotic inspection systems to support ground control evaluation in underground stone mines. Through field deployments and data analysis, the research showed that robotic platforms equipped with advanced sensing technologies can autonomously collect high-resolution spatial data in underground

environments. The collected data can provide detailed information about pillar geometry, entry dimensions, and surrounding structural conditions and when integrated with geomechanical analysis approaches, these datasets enable a more quantitative and systematic evaluation of pillar stability.

The findings highlight the potential for autonomous inspection technologies to complement conventional ground control practices. Traditional inspections may be limited by accessibility, safety concerns, or time constraints. Autonomous robotic systems offer the ability to collect consistent and repeatable measurements over large areas, including locations that may be hazardous or difficult for personnel to access. This capability can improve the quality of ground condition assessments and support earlier identification of potential stability concerns, thereby enhancing risk management and decision-making.

In addition to demonstrating technical feasibility, the project also provided insights into the operational challenges associated with deploying autonomous systems in underground mining environments. Issues such as navigation in complex mine geometries, communication limitations, lighting conditions, and data processing requirements were identified and evaluated. Addressing these challenges is important for enabling broader adoption of robotic inspection systems in routine operations. The knowledge gained through this research contributes to the development of improved workflows for robotic mapping, data interpretation, and integration with existing mine planning and ground control practices.

Autonomous mapping in underground environments has progressed beyond a purely conceptual or laboratory-stage capability, with several commercial platforms now offering integrated solutions for navigation and mapping in GNSS-denied conditions. These systems, particularly those leveraging LiDAR-based SLAM, are capable of performing autonomous or semi-autonomous mapping in controlled or moderately challenging environments, providing practical value for general inspection and large-scale spatial data acquisition. For baseline mapping tasks and routine inspections, commercially available drones can often provide an adequate and deployable solution without the need for extensive customization. However, this capability remains limited when applied to harsh, real-world underground conditions, such as those characterized by darkness, airborne dust, and feature-poor geometries. In these environments, there is still room for advancements in reliable localization, consistent autonomy, and high-fidelity reconstruction. Achieving engineering-grade mapping for detailed structural inspection requires advanced sensor fusion, careful mission planning, and multi-modal data integration, all of which remain active areas of research. Robust and fully reliable autonomous mapping in complex subterranean settings continues to depend on research-driven system integration and development.

From a health and safety perspective, the ability to remotely collect detailed structural information has significant implications. By reducing the need for personnel to enter potentially unstable or poorly supported areas, robotic inspection systems can directly decrease exposure to ground control hazards. Furthermore, the high-resolution datasets generated through robotic mapping provide valuable information for change detection over time, which may serve as early indicators of stress redistribution or developing instability. These capabilities can support more proactive ground control strategies that also include field-informed numerical models. Using obtained scans

to model real pillar geometries and applying brittle failure criteria allows us to more accurately analyze the stability of pillars where empirical methods fall short.

The methods developed in this project could be integrated into existing mine inspection and ground control programs by deploying autonomous or semi-autonomous robotic mapping platforms equipped with LiDAR sensors. These systems can be operated by trained personnel to periodically scan pillars and entries, generating high-resolution spatial datasets that can be analyzed using the workflows developed in this project. The ability to collect repeatable and objective measurements over large areas may significantly improve monitoring capabilities and reduce exposure of personnel to hazardous areas.

7. Recommendations for Future Work:

There are various paths to follow for research to further develop pillar stability assessment in underground limestone mining. One of the promising areas is the application of time-dependent modeling to capture long-term degradation processes such as creep and progressive spalling. It would enable more proactive ground control by modeling long-term stress and strength changes. In addition, the effects of dynamic loading conditions can be examined, including blast vibrations, seismicity, and induced stresses due to equipment, to achieve a simulation of working conditions. These conditions are particularly important under deep mining conditions, as the rock mass response will be more susceptible to sudden variations in stress.

While the CWFS model captures the progressive weakening of brittle rock, future simulations should look into including heterogeneity and natural jointing, and mesh refinement studies are also needed to evaluate the sensitivity of results to element size and type. High-resolution localized meshes may better represent narrow spalled zones and more realistic bands and geological discontinuities.

The results presented are based on conditions typical of Eastern and Midwestern U.S. limestone mines. Applying the model to deeper mines, weaker rock formations, or different geological settings will require adjusting material properties and validating failure modes. Collaborating with mine operators to collect site data and analyze past collapses can help enhance model robustness.

Future research should also focus on automated detection of structural features and potential instability indicators directly from 3D datasets. Integrating robotic mapping with numerical modeling tools and machine learning algorithms could further enhance predictive capabilities for ground control assessment and improve the workflow.

8. References

Akhihiero, D., & Gross, J. N. (2025, April). A Pointcloud Registration Framework for Relocalization in Subterranean Environments. In 2025 IEEE/ION Position, Location and Navigation Symposium (PLANS) (pp. 1257-1264). IEEE.

Ates, M. (2022), "Integrated Large Discontinuity Factor, LaModel, and Stability Mapping Approach for Stone Mine Pillar Stability" (2021). Graduate Theses, Dissertations, and Problem Reports.

Bendezu de la Cruz, Mario Alejandro, "Evaluation of LIDAR systems for rock mass discontinuity identification in underground stone mines from 3D point cloud data" (2021). Graduate Theses, Dissertations, and Problem Reports. 10243. https://researchrepository.wvu.edu/etd/10243

Dolinar, D. R. and Esterhuizen, G. S. (2007). Evaluation of the effects of length on strength of slender pillars in limestone mines using numerical modeling. Proceedings, 26th International Conference on Ground Control in Mining. West Virginia University, Morgantown, WV, pp. 304–313.

Elibol, A., D. Tuncay, and Z. Agioutantis, Assessing Pillar Stability in Underground Stone Mines: Impact of Geological Structures and Stress Variations In The Appalachian Region, (2024), Proceedings 58th US Rock Mechanics / Geomechanics Symposium (ARMA), 23-26 June 2024, Golden, CO, paper 24- 0578

Escobar, Samuel, "Implementing the Empirical Stone Mine Pillar Strength Equation into the Boundary Element Method Software LaModel" (2021). Graduate Theses, Dissertations, and Problem Reports. 10273. https://researchrepository.wvu.edu/etd/10273

Esterhuizen, G., Dolinar, D., Ellenberger, J., & Prosser, L. (2011). Pillar and Roof Span Design Guidelines for Underground Stone Mines. Pittsburgh: National Institute for Occupational Safety and Health.

Galvin, J. M., Hebblewhite, B. K. and Salamon M. D. G. (1999). University of New South Wales coal pillar strength determinations for Australian and South African mining 129 conditions. Proceedings, 2nd International Workshop on Coal Pillar Mechanics and Design. Pittsburgh, PA: U.S. Publication No. 99-114, IC 9448, pp. 63-71.

Hajiabdolmajid, V., Kaiser, P. K., & Martin, C. D. (2002). Modelling brittle failure of rock. In International Journal of Rock Mechanics & Mining Sciences (Vol. 39).

Johnson, J. C., Whyatt, J. K., & Loken, M. C. (2014). A generalized method for calculating pillar cell capacities for boundary element modeling of coal mines. Proceedings, 2014 SME Annual Meeting. Salt Lake City, Utah, February 23–26, 2014.

Kurre, Reece & Walton, Gabriel. (2020). A case study on the efficacy of different roof bolting schemes in Lhoist North America's Crab Orchard Mine. International Journal of Mining Science and Technology. 30. 10.1016/j.ijmst.2019.12.014.

Mark, C., Chase, F. E. (1997). Analysis of retreat mining pillar stability (ARMPS). In C. Mark & R. J. Tuchman (Eds.), Proceedings: New Technology for Ground Control in Retreat Mining NIOSH Information Circular 9446, pp. 17–34.

Mark, C. (1992). Analysis of Longwall Pillar Stability (ALPS): An update. Proceedings of the Workshop on Coal Pillar Mechanics and Design (pp. 238-249). U.S. Bureau of Mines.

MSHA. (2025). Mine Data Retrieval System (Accident Injuries Data Set). Retrieved from Mine Safety and Health Administration (MSHA): https://www.msha.gov/mine-data-retrieval-system

MSHA (2021). Assessing Pillar Collapse and Airblast Hazards in Underground Stone Mines Retrieved from Mine Safety and Health Administration (MSHA): https://www.msha.gov/newsmedia/special-initiatives/2021/10/29/pillar-collapse-initiative

MSHA (2020). Roof Control Plan and Ground Support Review Procedures: https://arlweb.msha.gov/READROOM/HANDBOOK/PH20-V-2.pdf

MSHA (2022a). Metal and Nonmetal Mine Safety and Health Resource Page Retrieved from https://arlweb.msha.gov/siteindex/mnmsiteindex.asp

National Institute for Occupational Safety and Health. (2021, 5 20). Number of active underground stone mines by year, 2000 - 2019. Retrieved from https://wwwn.cdc.gov/NIOSHMining/MMWC/Mine?StartYear=2000&EndYear=2019&SelectedMineType=1&SelectedCommodity=4#

Olivier, A. M. (2023). Optimising the use of three-dimensional data to lower gold grade dilution by controlling stope width in the mining of ultra-deep complex ore bodies, Doctoral dissertation, School of Mining Engineering, Faculty of Engineering and the Built Environment, University of the Witwatersrand, Johannesburg.

Rafiei Renani, H., & Martin, C. D. (2018). Cohesion degradation and friction mobilization in brittle failure of rocks. International Journal of Rock Mechanics and Mining Sciences, 106, 1–13. https://doi.org/10.1016/j.ijrmms.2018.04.003

Suner, M, "The Effect of Natural Fractures on the Mechanical Behavior of Limestone Pillars: A Synthetic Rock Mass Approach Application" (2021). Graduate Theses, Dissertations, and Problem Reports. 8254. https://researchrepository.wvu.edu/etd/8254

Suner, M and Tulu, I. Examining the Effect of Natural Fractures on Stone Mine Pillar Strength through Synthetic Rock Mass Approach. Mining, Metallurgy & Exploration (2022) (In press).

Samarakoon, K., Pereira, G., Gross, J (2022) "Impact of the Trajectory on the Performance of RGB-D SLAM Executed by a UAV in a Subterranean Environment" Proceedings of the International Conference on Unmanned Aerial Systems (ICUAS), Dubrovnik, Croatia.

Wagner, H. (1992). Pillar design in South African collieries. In Proceedings of the workshop on coal pillar mechanics and design. U.S. Bureau of Mines. Report IC 9315, pp. 283-301.

9. Appendix

9.1 Intact rock characterization

In the United States, Esterhuizen and Murphy (2011) released a database containing the specifications of underground stone mines. This database consists of pillar dimensions, uniaxial compressive strength of intact rocks, and rock mass characterization quantified based on Geological Strength Index. This database is based on field surveillance performed in 34 different underground stone mines and 94 different observations from these mines. This one of the most extensive databases for characterization purposes of underground stone mines. Therefore, Esterhuizen (personal communication, 2019) provided an extended version of this database with total performed 187 intact rock samples from additional 43 different mines. Later, Suner (2021) performed statistical analyses on this extended database to categorize underground stone mines by grouping them based on their intact rock uniaxial compressive strength test results. Therefore, he employed ANOVA to understand reducibility of parameters to represent each strength groups. He concluded underground stone mines can be categorized into three groups such as (1) low, (2) medium, and (3) high strength. And, for each strength group, Suner (2021) provided mean values and standard deviation for UCS, Young's modulus, Poisson's ratio, and specific gravity. The summary of this analyses can be seen in Table 10. While the characterization of the underground stone mine database is clearly presented by Esterhuizen et al. (2011), Esterhuizen and Murphy (2011) and Suner (2021), an alternative way to represent underground stone mines using the same database is performed in this section. Also, laboratory test performed and published by various researchers are summarized to provide insights on the mechanical behaviors of stone mine rocks in underground stone mines.

Table 10 Statistical analyses of stone mine database performed by Suner (2021)

<table>
<tr><th></th><th>UCS, MPa</th><th>Young's Modulus, GPa</th><th>Poisson's Ratio</th><th>Specific Gravity</th></tr>
<tr><td>Low Strength</td><td>88.45 [31.10]</td><td>46.56 [10.91]</td><td rowspan="2">0.12 [0.04]</td><td>2.57 [0.13]</td></tr>
<tr><td>Medium Strength</td><td>135.31 [27.77]</td><td>54.49 [10.23]</td><td rowspan="2">2.67 [0.06]</td></tr>
<tr><td>High Strength</td><td>214.21 [42.04]</td><td>62.84 [10.10]</td><td>0.17 [0.05]</td></tr>
</table>

The intact rock uniaxial compressive strength test results are fit through the Weibull cumulative distribution function with a simple Python script. For this fit process, sum of squares error minimization is performed and the residual sum of squares are calculated to quantify the performance of the fit. Figure 69 visualizes the Weibull cumulative distribution function fit for UCS values. The characteristic UCS value is found as 175.73 MPa, and the shape factor is calculated as 3.25. On the other hand, the same procedure is followed for the Young's modulus, and the Poisson's ratio. Figure 70 and Figure 71 represent the fit for tangent Young's modulus and Poisson's ratio values on Weibull cumulative distribution function, respectively. Also, the descriptive statistics for these fitting results can be seen in Table 11.

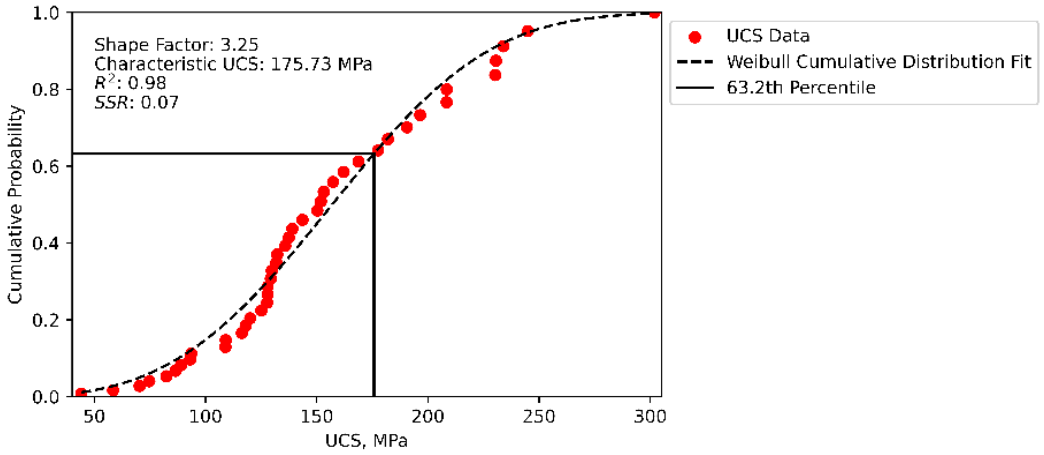

Figure 69 Weibull cumulative distribution fit for UCS

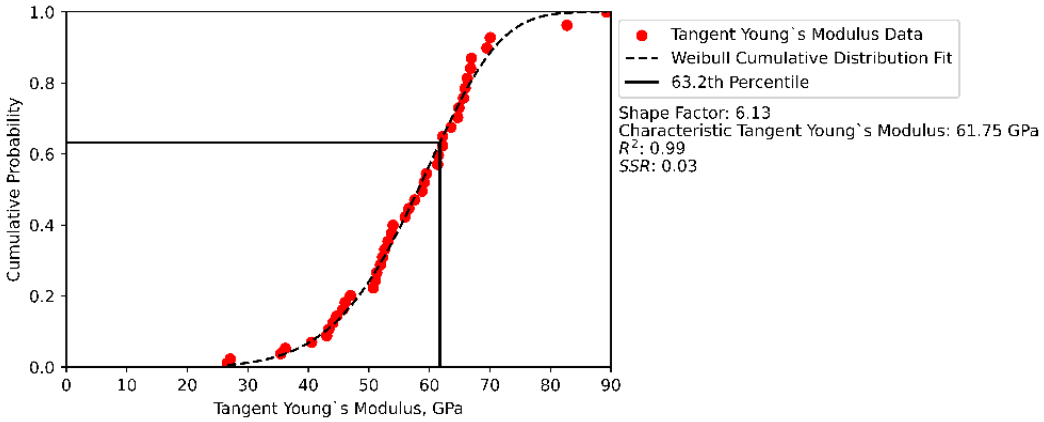

Figure 70 Weibull cumulative distribution fit for tangent Young's modulus

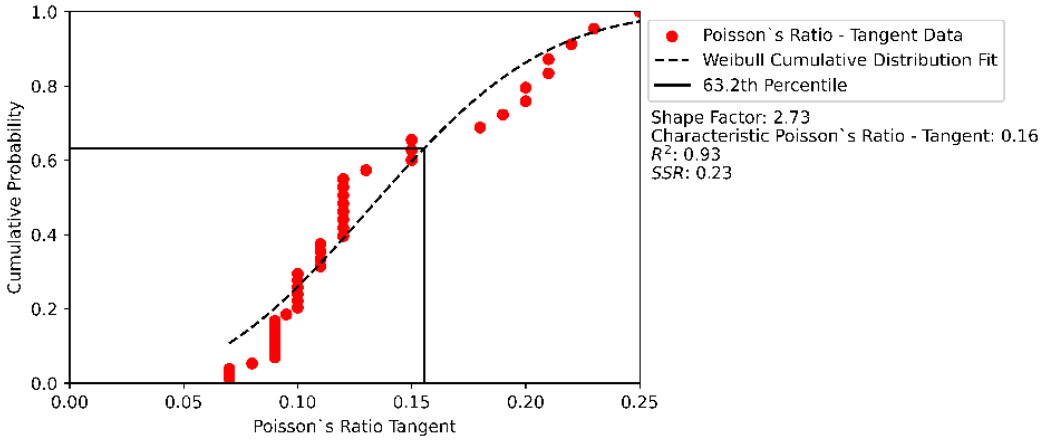

Figure 71 Weibull cumulative distribution fit for tangent Poisson's ratio

Table 11 Descriptive statistics based on Weibull cumulative distribution

	Shape	Scale	First Quantile	Third Quantile	Max	Min
UCS, MPa	3.25	175.73	119.81	194.3	301.91	44.13
Young's modulus, GPa	6.13	61.75	50.38	65.13	89.29	26.61
Poisson's ratio	2.73	0.16	0.1	0.18	0.25	0.07

9.1.1.1 Rock Mass Characterization

Additional information is collected to determine parameters to characterize underground stone rock masses. For the rock mass characterization, the descriptive statistics based on Suner (2022) analyses can be seen in Table 12 that in general underground stone mine rock masses have an average GSI value of 75.

Table 12 Descriptive statistics of rock mass characterization for underground stone mines in the US (square brackets indicate the GSI value)

	Mean	Standard Deviation	Minimum	Maximum
Low Strength	79 [74]	4.58	70 [64]	88 [83]
Medium Strength	81 [76]	4.25	70 [64]	90 [85]
High Strength	82 [77]	5.21	73 [68]	92 [87]

The most important take away here is the fact that expectations would be in favor that rock masses with high intact rock strength would have massive rock mass systems and their rating would be higher when compared to others. However, it is found that in each RMR rating category related with the geotechnical characteristics (e.g., RQD and joint spacing rating, and trace length of the discontinuities), high strength rock mass has lower rating. Therefore, the rock mass system is more jointed in the high strength rock masses where the main structure-controlled failure is observed.

While there is not information about the dip angle and the dip direction of the discontinuities in underground stone mines, Esterhuizen et al. (2011) indicate near vertical discontinuities with 81° mean dip angle is observed; and less than 20% of the discontinuities have the dip angle less than 70°. In addition, general rock mass structure of underground stone mines exhibits blocky rock mass characteristics that there are also horizontal bedding planes about 0° dip angle cutting through the vertical ones. However, Monsalve (2022) and Elibol et al. (2024) provided some insights into the underground stone mining environment's discontinuity system including orientation, size and density parameters. Monsalve (2022) presented three major discontinuity systems and one bedding plane observed in their case study mine. The summary table for this can be seen in Table 13. Note that the set 4 is bedding plane (e.g., this is a dipping mine) and Set 2's density mean and standard deviation are estimated since only minimum, 25%, median, 75%, and maximum value are provided as 0.18, 0.576, 1.180, 1.577, and 1.883, respectively. Also, while the size distribution follows the log-normal distribution, density is presented with normal.

Table 13 Discontinuity set properties provided by Monsalve (2022) for their case study mine (square brackets indicate the standard deviation)

Set	Dip	Dip Direction	Size	Density, p10
Set 1	88	255	0.353 [0.659]	1.011 [0.495]
Set 2	68	348	0.318 [0.772]	1.081 [0.742]
Set 3	75	21	0.018 [0.749]	0.928 [0.492]
Set 4	29	144	0.778 [0.934]	0.941 [0.477]

Recently, Elibol et al. (2024) historically examined the geological stress variations and discontinuities that may affect the pillar stability. Then, using automated discontinuity set extractor (Riquelme et al. 2014), they provided dip and dip direction of the four different cases. Table 14 summarizes their analyses results. Together Monsalve's (2022) and Elibol et al.' (2024) results, it can be said most of the discontinuities in the underground stone mines are nearly vertical, supporting Esterhuizen et al. (2011).

Table 14 Summary of discontinuity dip and dip direction estimation performed by Elibol et al. (2024) (Dip Angle/Dip Direction Angle is employed to present their results)

Case #	Joint Set 1	Joint Set 2	Joint Set 3	Joint Set 4
1	86°/229°	69°/137°	73°/315°	87°/186°
2	73°/318°	81°/281°	87°/167°	79°/64°
3	81°/306°	84°/349°	60°/163°	-
4-1	4°/45°	90°/262°	90°/352°	-
4-2	4°/45°	73°/178°	90°/262°	-

While the information about discontinuity orientations system is qualitative rather than quantitative; fortunately, extended stone mine database includes the spacing, dip, strike, and length rating of significant through-going discontinuities from floor to roof. Therefore, the specifications of these significant discontinuities are discussed. The majority of the significant discontinuities' strike is on East direction (e.g., 090°-100°). The rosette plot in Figure 72 visualizes the strike of 40 significant discontinuity recording in the database. On the other hand, the dip angles of these discontinuities are summarized in Figure 73a, where many of these discontinuities are near vertical. There is also major bedding planes exist in the underground stone mines where their dip angle is about zero except for the ones have 30°, where they are found in the dipping limestone mine. Figure 73b also shows the spacing of these significant discontinuities where the mean spacing value is about 12.86 m.

When the massive pillar collapses examined in terms of geological structures, it can be easily recognized that prominent discontinuity systems are leading to failure. In the first collapse case in a mine at Pennsylvania, the dip of the large discontinuities is about 50° to 80° and the spacing of them is about 2 m to 5 m (Esterhuizen et al., 2019). Another pillar collapse case showed that the similar geological structures are found with the previously identified by Iannacchione and Coyle (2002). In this mine they found that there is one longitudinal major joint set (e.g., strikes at N35°E to N45°E) with spacing from 3 m to 6 m, and local joint clusters at spacing from 1.5 m to 3 m.

Also, one non-persistent transverse joint set having strikes 7° to 16° offset from N47°W, and N54°W to N63°W is found.

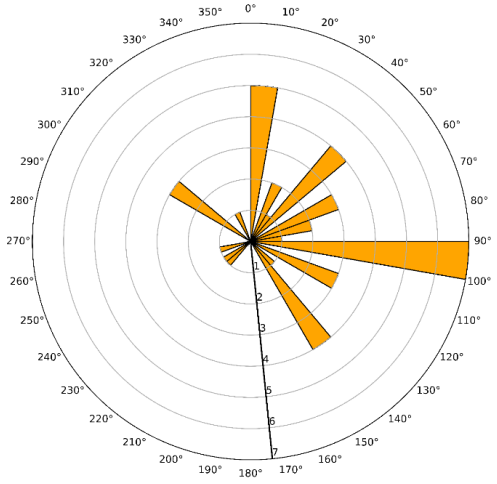

Figure 72 Rosette plot of the discontinuity strikes

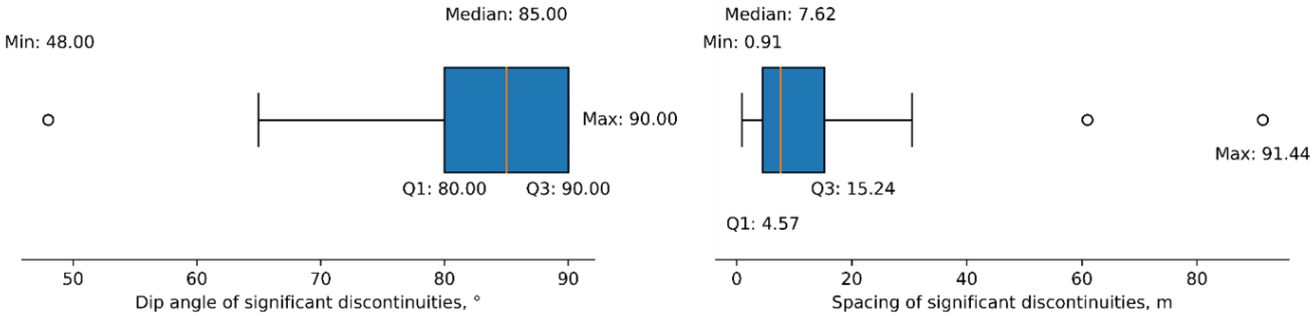

Figure 73 Box plots of significant discontinuities: a) dip angle, b) spacing

In 2011, Esterhuizen et al. summarized the operational parameters of the pillar dimension for both successful and un-failed cases. In these pillar reports, it is found that about 33% of the pillars are benched, and 18 individual pillars are categorized as complete failure. Main leading factor of failure for the more than half of the failed pillars is identified as the structurally controlled failure where most of them took place in medium and high strength rock masses. Descriptive statistics of the pillar dimensions successful and failed cases are summarized in Table 15.

Table 15 Descriptive statistics of successful and failed pillar dimensions of extended stone mine database

	Height, m			**Width, m**			**Width-to-height ratio**		
	Min	**Mean**	**Max**	**Min**	**Mean**	**Max**	**Min**	**Mean**	**Max**
Successful	4.82	11.1 [6.17]	37.98	4.57	13.06 [3.42]	24.49	0.29	1.41 [0.61]	3.52
Failed	3.7	9.93 [2.97]	15.2	7.3	15.82 [6.38]	27.4	0.44	0.69 [0.29]	1.75

In addition to Esterhuizen et al.'s field surveys, Rumbaugh et al. (2023) summarized the dimensions of the pillars, which were observed in the four massive pillar collapses occurred since 2015. In the below, based on Rumbaugh et al., the main characteristics of this collapses are

discussed. The characteristics of these five massive pillar collapse cases in terms of overburden depth, bench height, with-to-height ratios and number of pillars with collapse area is given in Table 16.

- **Collapse Case #1 – April 2015, Pennsylvania:** The mine had operated for about 25 years. Those collapsed pillars are the first pillars in the mine (e.g., legacy area pillars), and the benched area approximately benched 15 years before the event.
- **Collapse Case #2 – October 2020, Pennsylvania:** The pillar collapse involving about 25 pillars caused 2.9 magnitude seismic event on U.S. Geological Survey's seismic network. The development mining for the collapsed area is performed about 5 years ago.
- **Collapse Case #3 – November 2020 and July 2021, Pennsylvania:** The mine experienced two pillar collapses. In the first one, 12 pillars were involved while second collapse was about 25 pillars. In the first one, a sinkhole developed immediately, while the surface subsidence occurred within 48 hours of the pillar collapse. This is the first failure since 1950. The collapsed panel was initially developed between 1998 and 2001 and benched between 2002 and 2006.
- **Collapse Case #4 – August 2021, Tennessee:** The mine had an inspection in 2005 where they found there is a presence of through-going joints in the pillars and the karst features. About 40 pillars, developed 70 years prior, collapsed across an area of 567 Ares.

Table 16 Characteristics of five massive pillar collapses (Rumbaugh et al., 2023)

Characteristics	**Case 1**	**Case 2**	**Case 3**		**Case 4**
Pillar collapse date	April, 2015	October, 2020	November, 202	July, 2021	August, 2021
Overburden, m	61	49	152	182	122
Bench height, m	18	15	22	22	24
W/H ratio, minimum	0.54	0.63	0.76	0.76	0.45
Pillars	35	25	12	20	40
Pillars collapse area, Ares	284	202	243	364	567

Table 15 and Table 16 highlights that when the width to height ratio is low; in other words, when the slender pillars are employed in the underground stone mines, the possibility of failure of the pillar increases. This also stated by the S-Pillar (2011) software that the suggested lower boundary for width-to-height ratio of the pillars is 0.8.